FEDERAL UNIVERSITY OF SÃO CARLOS
CENTER FOR HARD SCIENCES AND TECHNOLOGY
GRADUATE PROGRAM IN MATERIALS SCIENCE AND ENGINEERING

ON THE THERMOMECHANICAL BEHAVIOR OF MODEL COMPOSITES USING DIGITAL IMAGE CORRELATION

Igor Paganotto Zago

São Carlos
2024

FEDERAL UNIVERSITY OF SÃO CARLOS
CENTER FOR HARD SCIENCES AND TECHNOLOGY
GRADUATE PROGRAM IN MATERIALS SCIENCE AND ENGINEERING

ON THE THERMOMECHANICAL BEHAVIOR OF MODEL COMPOSITES USING DIGITAL IMAGE CORRELATION

Igor Paganotto Zago

Thesis presented to the Graduate Program in Materials Science and Engineering as a requirement to obtain the title of DOCTOR IN SCIENCE AND MATERIALS ENGINEERING

Supervisor: Dr. Rodrigo Bresciani Canto
Co-supervisor: Dr. Ricardo Afonso Angélico
Funding Agency: CNPq - Process: 140250/2020-4

São Carlos
2024

CANDIDATE’S VITAE

Lecturer at the Federal Institute of Education, Science and Technology (IFSP) (2019-2020),
Master in Science and Mechanical Engineering with emphasis on Aircraft from University of São Paulo (USP) (2017-2019),
Technologist in Aircraft Maintenance by the Federal Institute of Education, Science and Technology of São Paulo (IFSP) (2014-2016).

UNIVERSIDADE FEDERAL DE SÃO CARLOS

Centro de Ciências Exatas e de Tecnologia
Programa de Pós-Graduação em Ciência e Engenharia de Materiais

Folha de Aprovação

Defesa de Tese de Doutorado do candidato Igor Paganotto Zago, realizada em 28/06/2024.

Comissão Julgadora:

Prof. Dr. Rodrigo Bresciani Canto (UFSCar)

Profa. Dra. Ana Paula da Luz (UFSCar)

Prof. Dr. Marco Aurelio Liutheviciene Cordeiro (UFSCar)

Prof. Dr. Jonas de Carvalho (USP)

Prof. Dr. Rodrigo Ribeiro Paccola (USP)

O Relatório de Defesa assinado pelos membros da Comissão Julgadora encontra-se arquivado junto ao Programa de Pós-Graduação em Ciência e Engenharia de Materiais.

ACKNOWLEDGEMENTS

A lot happened in the course of my PhD. Right in the beginning, I was called to be a substitute professor at the institute where I had graduated, and for six months I carried the teaching at IFSP with the learning at UFSCar, from the end of 2019 to the beginning of 2020. During this time, my grandfather, who was such an important and influential figure in my life, passed away. Thus, I decided to stop dividing my attention and focus on my studies, leaving my position at IFSP. A month later, the COVID-19 pandemic struck the world, and life changed in so many ways: isolation, anxiety, depression, and an overall feeling of emptiness and lostness. This confusing time is all mixed memories. The impression is that it lasts a lot longer than it actually did, while it appears to be much closer to nowadays than it actually is. The pandemic took two years of the planned experimental work of my PhD. When things began to normalize, even with the uneasy feeling that getting back to a normal life brought. The experimental work began with many developments, discoveries, and setbacks, which if had occurred sooner, perhaps would not have been much of a deal, but in the face of the two and a half years that had passed, the feeling of urgency gave new weight to each experimental drawback.

The story told so far seems like a tragedy, but as preached by Friedrich Nietzsche, adversity invites us to experience who we are and the true reason for what we are doing. Each challenge during these almost five years was faced and surpassed, and it was not merely my effort, but the support of so many people in my life that allowed me to succeed.

Initially, I would like to thank my parents Fabio and Betina, for their love and support during my long academic journey, always encouraging me to pursue this path. Also to my supervisor Rodrigo Bersciani Canto and co-supervisor Ricardo Afonso Angélico for guiding me throughout this journey, and helping me to improve as a researcher, teacher, and a person.

My gratitude to professor Vinicius Sciuti, and lab colleagues Rafael Vargas, Salvino Macêdo, Matheus Furlan, Matheus Cardoso, Igor Bonizio, and all the others, for I have nothing but gratitude for the nice social environment and companionship at UFSCar. I also would like to thank my former colleagues at USP, who helped me in the first stages of this research.

I would also like to acknowledge Walter Aparecido Mariano for the knowledge and assistance given to the realization of this work. Also to Prof. Ana Paula Luz for the valuable insights in ceramic materials and for the assistance in the Undergraduate Education Modernization Program.

To my good friend Gustavo Bertoli for all the discussions since elementary school until the PhD.

Finally, to all the others that help in some way with the development of this work, and also, to PPGCEM that allowed me to conduct this research.

Financial support:

To CNPq - Conselho Nacional de Desenvolvimento Científico e Tecnológico, for the financial support for carrying out this work with a scholarship, process 140250/2020-4.

To the São Paulo Research Foundation (FAPESP) #2020/08077-6, for the financial support to carry out part of this work allowing the acquisition of many of the equipment used in this study.

This study was financed in part by the Coordenação de Aperfeiçoamento de Pessoal de Nível Superior - Brasil (CAPES) - Finance Code 001.

“No one really starts anything new, Mrs. Nemur. Everyone builds on other men’s failures. There is nothing really original in science. What each man contributes to the sum of knowledge is what counts"

- Daniel Keyes, Flowers for Algernon.

ABSTRACT

In composite systems with incompatibility between the coefficients of thermal expansion (CTE) of their phases, stresses can lead to cracking of the material during a temperature variation. Analytical, numerical and experimental studies on the subject have been carried out. Experimentally, this topic is difficult to approach, since observing and measuring the effects of temperature variation in composite systems is not a trivial task. With the development and improvement of field measurement techniques such as Digital Image Correlation (DIC), a new approach is proposed in combination with the use of model composites. In the present study, mechanical and thermal properties of model composites phases composed of alumina and colloidal silica matrices with cylindrical inclusions of brass or zirconia were evaluated, and temperature variation experiments aided by DIC were carried out to obtain experimental displacement and strain fields. The model composites temperature variations were conducted up to 300, 600 or 900 °C depending on the systems's response up to that temperature. Such experiments allow the visualization of the model composites cracking, which can be quantified in terms of crack initiation and evolution. The quantification of cracking was done from the calculation of an inelastic strain field. Obtaining this field of both opposite faces of the tested systems and quantifying its cracking provides data for comparison with analytical and numerical modeling of cracking phenomena due to CTE incompatibility of such systems, results that do not exist in the literature. Thus, the data produced allows the modeling of this phenomenon to be carried out for the proposed composite systems, using the evaluated properties and having field information and parameterized cracking parameters for comparison.

Keywords: thermomechanical behavior; CTE mismatch; model composites; digital image correlation

RESUMO

SOBRE O COMPORTAMENTO TERMOMECÂNICO DE COMPÓSITOS MODELO UTILIZANDO CORRELAÇÃO DE IMAGENS DIGITAIS

Em sistemas compósitos com incompatibilidade entre os coeficientes de expansão térmica (CET) de suas fases, tensões podem levar ao trincamento do material durante uma variação de temperatura. Estudos analíticos, numéricos e experimentais sobre o assunto foram realizados, porém, experimentalmente, esse tema é de difícil abordagem, visto que a observação e medição dos efeitos da variação de temperatura em sistemas compósitos não é uma tarefa trivial. Com o desenvolvimento e aprimoramento de técnicas de medição de campo, como a Correlação de Imagens Digitais (CID), uma nova abordagem é proposta em combinação com a utilização de compósitos modelo. No presente estudo, propriedades mecânicas e térmicas das fases constituintes de compósito modelo com matriz a base de alumina e sílica coloidal e inclusões cilíndricas de latão ou zircônia foram avaliadas, e experimentos de variação de temperatura auxiliados por CID foram realizados para obtenção dos campos de deslocamento. As variações de temperatura dos compósitos modelo foram conduzidas até 300, 600 ou 900 °C dependendo da resposta do sistema na temperatura. Tais experimentos permitem a visualização do trincamento do material, o qual pôde ser quantificado em termos de início e evolução. A quantificação do trincamento foi feita a partir do cômputo de um campo de deformações inelásticas. A obtenção desse campo e a quantificação do trincamento de ambas as faces opostas dos sistemas ensaiados fornece dados para comparação com modelagens analíticas e numéricas de fenômenos de trincamento por incompatibilidade dos CTEs, algo que não existe na literatura. Assim, os dados produzidos possibilitam que modelagens desse fenômeno possam ser realizadas para os sistemas compósitos propostos, utilizando as propriedades avaliadas e tendo informações de campo e parâmetros de trincamento parametrizados para comparação.

Palavras-chave: comportamento termomecânico; incompatibilidade de CET; compósitos modelo; correlação de imagens digitais.

PUBLICATIONS

SCHIAVON, F.L.; ZANARDI, H.; ZAGO, I.P.; ANGÉLICO, R.A.. Prediction of elastic parameters of particle reinforced composites using finite element simulations, Mater. Res. 26 (2023) e20220475, http://dx.doi.org/10.1590/1980-5373-MR- 2022-0475.

ZAGO, I. P.; VARGAS, R.; SCIUTI, V. F.; CANTO, B. C.; ANGÉLICO, R. A. DIC to evaluate a model composite system cracking due to CTE mismatch. In: Theoretical and Applied Fracture Mechanics. 2024. doi:10.1016/j.tafmec.2024.104330.

VARGAS, R., ZAGO, I.P., SCIUTI, V.F., FURLAN, M., ANGÉLICO, R.A., HILD, F., et al. Multi-Window Setup for Thermomechanical Experiments Assisted by DIC up to 900 ℃. Materials Research. 2024; 27. doi:10.1590/1980-5373-MR-2024-0072.

CONFERENCE PROCEEDINGS

ZAGO, I. P.; CANTO, R. B.; ANGÉLICO, R. A.. Crack pattern of a composite model material submitted to a temperature increase assisted by DIC. Brazilian Conference on Composite Materials. Anais. São Carlos, SP: EESC/USP, 2021.

ZAGO, I. P.; Furlan, M.; Angélico, R. A.; Canto, R. B.. Avaliação da influência das tensões residuais no comportamento termomecânico de compósitos modelo bifásicos fabricados por prensagem de pó. 24° Congresso Brasileiro de Engenharia e Ciência dos Materiais (CBECiMat). Águas de Lindóia. 2023.

Zanardi, H.; Schiavon, F. L.; Zago, I. P.; Angélico, R. A. Evaluation of effective mechanical properties of particle reinforced composites via numerical simulations of representative volume elements. GAMM 2023 - 93º annual meeting of the international association of applied mathematics and mechanics, Dresden, Germany.

VIEIRA, B. L.; ZAGO, I. P.; ANGÉLICO, R. A.. Aplicação da técnica de correlação de imagens digitais em um material modelo submetido à variação de temperatura. 31º Simpósio Internacional de Iniciação Científica e Tecnológica da USP. Anais. São Carlos, SP: EESC/USP, 2023. Disponível em: https://www.eesc.usp.br/biblioteca-admin/wp-content/uploads/2024/02/cicte2023anaisp

Oliveira, F. L. A; Zago, I. P; Sciuti, V. F.; Angélico, R. A. Integrating mesh adaptivity and digital image correlation for full-field displacement evaluation of cracked bodies. XLV Ibero-Latin American Congress on Computational Methods in Engineering (CILAMCE), 2024.

Gonçalves, A. M; Zago, I. P; Vargas, R; Canto, R. B; Angélico, R. A. Young's modulus identification via finite element method updating using full-field data from a 3-point bending test. XLV Ibero-Latin American Congress on Computational Methods in Engineering (CILAMCE), 2024.

Special projects

Professor Advisor on the extension project: Divulgação dos cursos técnicos nas escolas públicas por intermédio dos alunos do IFSP. 2019.

Tutor in the discipline Mecânica dos Sólidos. Ministered by Professor Rodrigo Bresciani Canto, 2020.

Tutor in the discipline Projetos em novos materiais. Ministered by Professor Rodrigo Bresciani Canto, 2021.

Assistant PhD student in the Modernization of Undergraduate Education project. Visit to Massachusetts Institute of Technology (MIT) to learn about the undergraduation structure of the Material Science and Engineering course. 2022.

SUMMARY

LIST OF TABLES

LIST OF FIGURES

LIST OF ACRONYMS AND ABBREVIATIONS

AA-D - Atomized alumina pressed disk specimen

BR-B - Brass Bar

BR-D - Brass Disk

CA-D - Calcined Alumina Disk mortar

CMCs - Ceramic Matrix Composites

CTE - Coefficient of Thermal Expansion

CVI - Chemical Vapor Infiltration

DIC - Digital Image Correlation

DVC - Digital Volume Correlation

EA-S - Electrocuted Alumina mortar with Square cross-section

EA-B - Electrocuted Alumina mortar parallelepiped Bar

IDIC - Integrated Digital Image Correlation

IET - Impulse Excitation Technique

LVDT - Linear Variable Differential Transformer

MCS - Model Composite System

MCS-CAB - Model Composite System Calcined Alumina-Brass

MCS-EAB - Model Composite System Electrofused Alumina-Brass

MCS-EAYSZ - Model Composite System Electrofused Alumina-Yttria Stabilized Zirconia

MMCs - Metal Matrix Composites

PMCs - Polymer Matrix Composites

PPGCEM - Programa de Pós-Graduação em Ciência e Engenharia de Materiais

RFDA - Resonant Frequency Damping Analyzer

ROI - Region of Interest

TRS - Thermal Residual Stress

UFSCar - Federal University of São Carlos

UTM - Universal Testing Machine

YSZ-B - Yttria Stabilized Zirconia bar

YSZ-C - Yttria Stabilized Zirconia Cylinder

LIST OF SYMBOLS

Latin symbols

a - Crack length

A - First parameter of the radial displacement solution

B - Second parameter of the radial displacement solution

$\mathbf{C}$ - Constitutive tensor

E - Young's modulus

$\boldsymbol{I}$ - Identity matrix

I_0 - moment of inertia

$\mathcal{G}$ - Energy release rate

K - Bulk modulus

K_t - Concentration factor

M - Cross-section

P - Cohesive strength

P_c - Cohesive force

u - Displacement

U - Potential energy

W_s - work to create new surfaces

r - Radius or radial axis

$\mathbf{u}$ - Displacement field

Greek symbols

α - Thermal expansion coefficient

$\Delta\alpha$ - Inclusion thermal expansion coefficient minus matrix thermal expansion coefficient

γ - shear strain

γ_s - surface energy

ΔT - Temperature variation

λ - First Lame's parameter

μ - Shear modulus (Second Lame's parameter)

υ - Nodal displacement

$\mathbf{\Psi}$ - Shape function

ν - Poisson’s ratio

Π - External work

σ - Normal stress

ε - Normal strain

τ - Shear stress

Φ - Volume fraction

κ - Curvature

Subscripts

I - Inclusion property

M - Matrix property

i - Inclusion's domain

m - Matrix's domain

s - secant

t - tangent

x - Horizontal component in Cartesian coordinate system

y - Vertical component in Cartesian coordinate system

z - Vertical component in cylindrical coordinate system and out-of-plane component in Cartesian coordinate system

1 - Maximum principal component

r - Radial component in spherical and cylindrical coordinate systems

ϕ - Tangential component in spherical coordinate system

θ - Tangential component in spherical and cylindrical coordinate systems

Superscripts

e - Elastic component

i - inelastic component

t - Thermal component

1 INTRODUCTION

This chapter intends to assist the reader to situate itself in the context of the present thesis. With that in mind, it begins contextualizing historical developments in understanding materials, especially the relation of composite materials and mankind. Then, the challenges related to the use of composite materials in applications with temperature variations are presented, which motivates the present work and establishes the goals of this research. At last, the structure of the thesis is shown, allowing the understanding of the approach adopted.

1.1 Some history

Through time, many skills were developed to reach the current technological stage of society, being one of the most important the domain of materials: the understanding of their properties, their manufacturing process, and finally, their structure in many levels. The knowledge about materials is so intrinsically connected to mankind's history that even the history timeline is eventually expressed in terms of the main material usage or innovation at the time, such as the Stone Age (Paleolithic and Neolithic), the Bronze Age and the Iron Age [1, 2].

The need to better comprehend materials led to their most basic and general classification. Those materials which have a high density, are shiny when polished, stiff and yet ductile, and are good electrical and thermal conductors were classified as metals. Materials that have low density, stiffness, and melting point, but accept relatively high deformations were classified as polymers. Last but not least, those that present hard and brittle behavior, have high melting points and are neither good electrical nor thermal conductors were classified as ceramics. It is clear that these generalizations do not embrace all the materials existent, and that in each class several examples do not fit perfectly its characteristics. Even so, this classification set the basis for material science. In the dawn of Material Science, these materials classes were researched and enhanced almost completely separate from each other based on their different observed most fit appliances [3].

Despite that, there is another material class that has been used since a wood stick was taken by human hands and when archery was the finest long-range weapon, composites. Composite materials are a combination of materials with distinct properties or behaviors that result in a new one with superior effective properties to a given application than each of its phases alone. Of course, wood is a natural composite, and man's knowledge about what makes this material so versatile and distinct from others was not completely understood for a long time. The first man-made composite known is most probably the Egyptian papyrus that was used circa 4000 B.C., also bricks of mud reinforced with straw were used circa 1300 B.C. One of the most important composites used in the early days that led to enormous cultural and territorial growth through time was the concrete used by the Greeks and especially the Romans 2000 years ago [2, 4]. Figure 1.1 presents some composites used by mankind in the early days.

(a) (b) (c)

Figure 1.1: Examples of composite materials used in the past. (a) Greek art representing an archer with a wood bow and arrow [5]; (b) Egyptian papyrus [6]; (c) Roman concrete [7].

Although natural and man-made composites have been used for a long time, it is mostly a consensus that in the 60's composite materials began to be studied as a distinct discipline. This fact happened partly because of the increasing demand in the aerospace and civil engineering fields for stiffer, stronger, and lighter materials. These new challenges brought attention to the concept of material combination once the traditional classes of materials did not fulfill the unattainable performance required for the engineering improvement needed at the time. By taking this approach, it can also be said that material design was never so important and developed as in creating the composite structures to supply these needs [8].

Since composites begun to be properly studied, a lot has been developed. In the aircraft industry, for example, composite structures had replace metal alloys as a major structural aircraft material in the most recent projects. Also, Marine and wind energy industries are becoming high based on composite structures [9]. Civil industry is one that has always made use of composites, as concrete, reinforced concrete, and wood structures and composites. In the 21st century, civil engineering embrace the use of more advanced composite systems for the maintenance, repairment, and replacement of structures such as bridges and other large engineering structures [10]. The developments that led to this increase in composites use, came with many challenges and the need to understand new and more complex material behaviors, that are still open to study and debate up today.

The study of different approaches to material combination led to different manufacturing process strategies and also, the perception that material combination could be applied to create property combinations that were previously considered impossible.

1.2 Context

Nowadays, a wide range of composite materials is largely applied in several industries, including aeronautical, medical, sports, space, and base. These industries desire materials more suitable for their specific needs, with enhanced property combinations to meet their demands. For these reasons, the composite research field grows continuously to meet the expectations of these ever-developing industries. These materials are key in overcoming many engineering problems in obtaining property combinations appropriated for specific applications. At the same time, they were a driving force to interconnect the different material science fields by creating material systems that combine different material classes, which leads to innovative possibilities. For instance, the increase in strength of polymers by the insert of a ceramic phase [11], the addition of electrical conductivity to materials that were insulators by the incorporation of a conductive metal phase [12], and the increase in toughness to brittle materials by the introduction of material phases or phases' interfacial condition that helps to alleviate stress or to create toughness mechanisms [8, 13, 14]. Thus, there is a tendency for the increase in the composite materials' usage, as demonstrated in Figure 1.2, where the evolution of different material classes relevance can be observed over time.

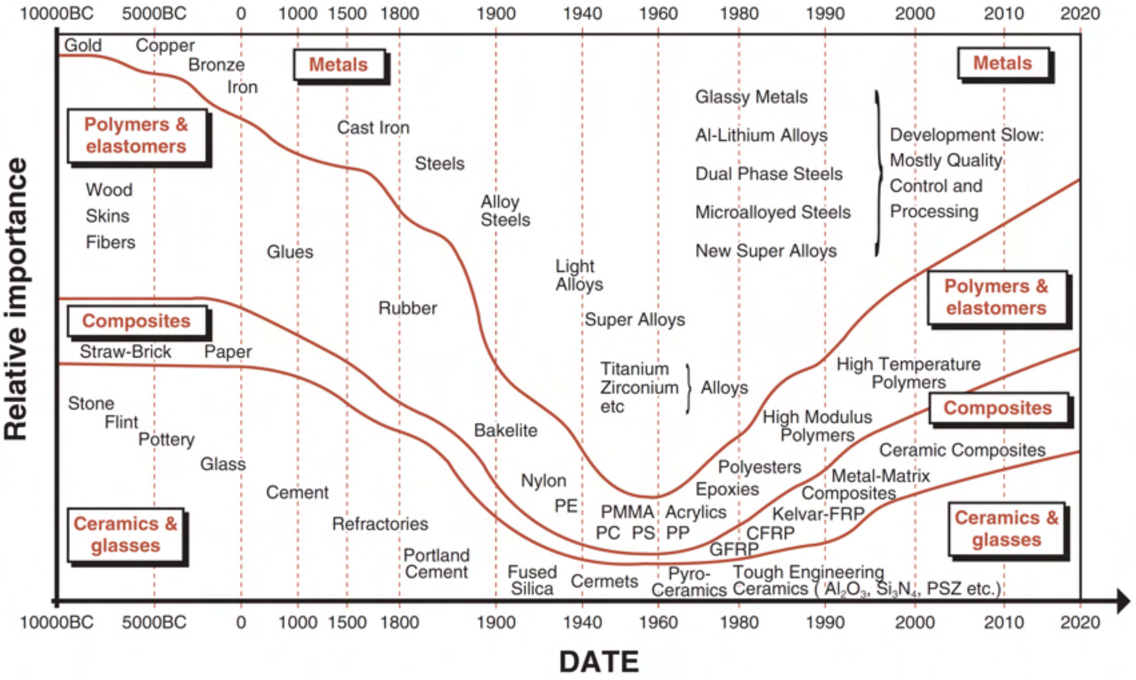

Figure 1.2: Material classes importance through time. Since the 60's [1], a growth in composites usage can be seen.

Composite materials are created by combining different material phases, which usually will have different properties. Consequently, each composite's phase has different responses to mechanical, thermal, chemical, and physical stimuli, leading to complex behavior and demanding attention in its application [8–10, 15]. For instance, when a composite is comprised by phases presenting different coefficients of thermal expansion (CTE - α), and this material is submitted to a temperature variation, stress between the phases will arise, which may lead to crack nucleation, propagation, or even complete material failure [16–20].

A way to look at this phenomenon is as a problem, once several times, the main purpose of using composite materials is to increase the resistance or toughness of a traditional material already used for a particular application. However, in a controlled and predictable way, this phenomenon can create better materials for applications such as thermal insulation, where a crack network can increase the material insulation efficiency and be helpful to other interesting technological applications [1, 21–25]. Some refractories that present cracks due to CTE mismatch also show increased resistance to thermal shocks [26]. Furthermore, the Coefficient of Thermal Expansion (CTE) mismatch in composite materials is already used in systems such as heat and fire detectors [27], and also has been applied to some new technological innovations like shape memory composite materials [28].

Cracks due to phase's thermal expansion mismatch are an exciting subject in the developing of high-performance Ceramic Matrix Composites (CMC's). Some examples can be observed in aerospace applications such as space probes, space shuttles, heat shields and the leading edges of supersonic aircraft. These applications demand resistance to high temperatures, resistance to temperature variations, and adequate mechanical properties [21, 29–31]. Nevertheless, several composites processing routes comprehend significant temperature variations, as Chemical Vapor Infiltration (CVI), Chemical Vapor Deposition (CVD), and Melt-Infiltration (MI) process, where it is not unusual for the appearance of cracks or Thermal Residual Stress (TRS) in the material after cooling [32–34]. Therefore, as explained by King [35], cracks in composites can originate from TRS in the processing and thermal stress in in-service conditions. An example of cracks in a titanium matrix reinforced with silicon carbide resultant of TRS is displayed in Figure 1.3 [35].

Therefore, the continuous appliance of composite materials to engineering applications creates the need to better comprehend such materials in an extensive range of work conditions. For that, analytical and computational models have been developed to evaluate the response of composite materials in the different environments where these are required. In the last decades, the advance in computer processing made possible a significant advance in understanding the thermomechanical response of composites by using numerical tools [36, 37]. Nevertheless, experimental results are essential to evaluate and validate these models.

The interest in composite materials' mechanical behavior under temperature

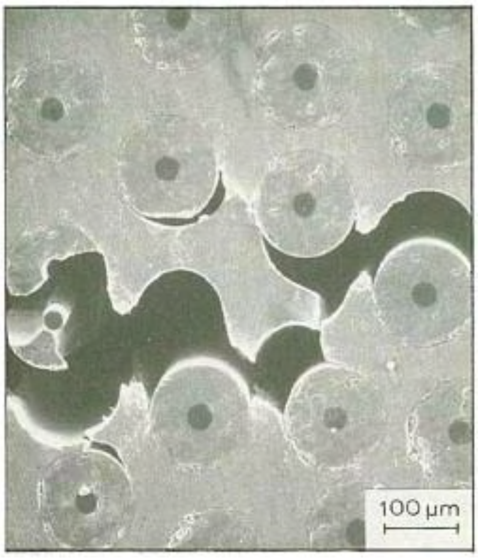

Figure 1.3: Cracks in a titanium metal matrix reinforced with silicon carbide fibers. (credits: J G Robinson and British Petroleum) [35].

variation has been relevant since the 60s. Many experimental studies of that time and after opted for the use of glass matrix composites to make possible the observation of the interfacial region between the material's phases, observing the crack pattern after a temperature variation [17, 18, 38]. As an outcome of using glass matrix composites, fracture occurred abruptly, precluding results of the transient stage – the crack nucleation and propagation. Even so, in the lack of more advanced methodologies and techniques, the glass matrix was a clever solution to map the inclusions in the composite and see the resulting crack pattern. The use of model materials is an excellent aid to experimental works. Model materials highlight properties or interesting phenomena by creating a simple system to be studied and compared with analytical and numerical models [17, 39, 40].

In the specific context of mechanical and fracture properties of composite materials submitted to a temperature variation, many studies have analyzed the thermomechanical behavior of composites by observing the before and after states of the material regarding a temperature variation [17, 41]. However, few presented data about the evolution of the material in fracture [18], and even less bring field information regarding this evolution [42]. This could be because of the difficulty of observing the phenomenon when working with opaque matrices, in reason of the speed of the phenomenon when working with a glass matrix, or the small scale of the reinforcement phase and/or cracks in the material, among other issues.

1.3 Motivation

With the increasing effort in developing analytical and computational models to evaluate composite materials' response to different applications, an experimental gap needs to be filled. This gap consists of simple experiments which provide enough data to be accurately compared with those models. With the development and advance of the Digital Image Correlation (DIC) technique, it is possible to obtain field experimental data with great precision and without invasive measurement tools. Also, the DIC technique allows the identification of cracks by post-processing its results, allowing the observation of crack nucleation and growth in the surface or even in the interior of the material using tomography, performing the Digital Volume Correlation (DVC) technique [43, 44].

Thus, due to the shortage of experimental data relating crack nucleation and growth in composite materials submitted to temperature variation, an experimental procedure assisted by DIC using a model composite material to investigate CTE mismatch crack phenomena was idealized. As presented, many applications and processes expose composite materials to temperature variations, where the mismatch between the phases' CTE might result in the system cracking. Whether these cracks are beneficial depends on the application of interest, but independent of the case, understanding this phenomenon is essential. Therefore, experimental data to improve or validate analytical and computational models is the main concern of this work.

1.4 Goal

The aim of this thesis is to produce reliable field experimental results in regard to the interaction of model composites phases during a temperature variation. These results can be used for evaluating, developing, and validating models that investigate the interaction between composites' phases and the crack nucleation and propagation due to temperature variation due to the phases properties mismatch. The obtaining of experimental field evolution of cracking initiation and propagation brings a lot of information that can be explored in future works. To produce the data and ensure trustworthy of the experiments, the respective specific tasks were achieved:

- Create Model Composite Systems (MCS) to be experimentally tested that have an optimized geometry for the use of the DIC technique;
- Characterize relevant thermomechanical properties of the MCSs phases, regarding the properties of interest to analytical and numerical models;
- Develop experimental equipment optimized to perform thermomechanical experiments assisted by DIC;
- Obtain the evolution field results of the MCS cracking nucleation and propagation resultant of temperature variation using the DIC technique and evaluate the cracking of these systems;
- Compare the experimental results with analytical and numerical models.

1.5 Thesis project framework

This manuscript is organized into five chapters. The first chapter contextualizes the scientific and technological developments in the use of materials, especially composite materials. Then, it introduces the main subject of this thesis: the investigation of the thermomechanical behavior of Model Composite Systems (MCSs) when subjected to temperature variations.

In the second chapter, an overview of composite materials and MCSs is presented, as well as some important concepts like volume fraction. Relevant concepts of the mechanical and thermal behavior of materials are approached to then present the general stress-strain and fracture behavior of simplified composite systems under a temperature variation, with some examples of the influence of different material properties on the material response. At last, the principles of the Digital Image Correlation (DIC) technique are presented.

The third chapter presents the methodology used to manufacture the specimens and perform the mechanical and thermal experiments. It also describes aspects related to the use of DIC.

The fourth chapter presents the research results, including the materials phases mechanical and thermal characterization and the temperature variation of the MCSs. Different methodological approaches are used to better quantify the cracking of the MCS and to investigate the cracking in different material systems and with different inclusion configurations and sizes.

Lastly, the fifth chapter presents the remarks of this research, exploring analytical insights, experimental and numerical methodology approaches tested, and, of course, the main findings regarding the experiments performed.

2 THEORETICAL FRAMEWORK

This chapter presents the scientific and technological fundamentals of composite materials and model composites. Also, the effects of temperature variation on mechanical behavior and fracture mechanics of composites are explained here. Further, the principles of Digital image correlation are presented, supporting the comprehension and the discussion later in the results.

2.1 Composite materials

Composites are a particular class of materials designed to obtain optimal effective properties by combining different material systems. Therefore, it is impossible to group composites by means of common properties but rather by their strategies and morphological architecture. The following subsections explore the idea of defining and classifying composites.

2.1.1 Definition

The literature presents different concepts concerning the key to classifying a material as a composite instead of a compound, heterogeneous alloy, or other inhomogeneous solid groups. Composites are part of a larger group, viz. the heterogeneous materials, and the distinction among these minor classes is not always evident, especially for small scales [45, 46]. However, a reasonable way to classify a material as a composite is the existence of an interface between its phases [14, 15]. Composites are materials composed of two or more phases chemically, mechanically, or geometrically distinct that together result in a material with superior effective properties to an application of interest than each of its phases alone [14, 15, 47]. They are also characterized by an interfacial region that, in many situations, has its own intrinsic properties and behavior [8, 14].

Before getting into the composite materials' classification, some concepts of composites must be defined. The most traditional composite materials are formed by continuous and dispersed phases. The dispersed phase may improve some properties of the material, such as strength, toughness, etc. For example, in large aircraft composite structures, there is an outer conductive skin with graphene or carbon nanotube conductive fibers and an inner insulator phase used to overcome lightning strikes with safety [12]. The matrix determines the composite geometry, transfers the loads through the composite, and surrounds the other phases. At last, sometimes there is a void phase, such as pores, cracks, or spaces with vacuum, air, or inert gas. This phase can be helpful in thermal insulation, electrical insulation, and weight reduction [8, 14, 15, 48, 49].

Composite materials can be classified by different criteria. These materials are engineered to obtain the best of their constituents since the possibilities concerning their constituents' choices are numerous. There is a synergy involving composites development, as these materials are designed to achieve high performance considering their in-service conditions [8]. The following section provides an overview of the possibilities to classify composite materials.

2.1.2 Classification

There are several ways to classify composite materials, e.g. by their function, dispersed phase geometry, continuous phase material type, and dispersed phase material type [8, 14, 15].

Regarding its function, there are the structural composites and the non-structural ones. The structural composites are those used in structural applications for their interesting mechanical properties. These composites are usually honeycomb sandwich structures or traditional multi-layer composite structures, while the non-structural composites used to be only a dispersed phase embedded in a matrix. However, the final material strength for a particular application is the most important aspect. For example, although concrete is considered a low-performance composite in several aspects, it is still an important structural composite for civil engineering [1, 8, 13, 15].

The dispersed phase geometry defines mainly the discontinuous phase's shape, drastically affecting the composite's final properties. For example, using a single layer of a continuously oriented fiber will lead to an anisotropic mechanical behavior; however, this behavior is not expected when using a well-distributed spherical dispersed phase. The most common types of dispersed phases are particles, short fibers, long fibers, and whiskers. A subclassification when using short fibers and whiskers is about the orientation of the dispersed phase, once a random orientation produces a more isotropic material, and a regular orientation produces a more anisotropic material [1, 8, 13–15, 50].

Finally, there is the material type of the phases, viz. polymeric, ceramic, or metallic. Therefore, composites can be defined as polymer matrix composites (PMCs), metal matrix composites (MMCs), and ceramic matrix composites (CMCs).

2.1.3 Volume fraction

When discussing composite materials, it is important to know the concept of volume fraction (ϕ). The volume fraction is the macroscopic ratio between the volume occupied by a dispersed phase and the total volume [15, 51]. It is essential to highlight that it depends on the total volume considered. For instance, in the vicinity of the dispersed phase, the local volume fraction can be higher or lower than its nominal value. For example, a composite with a volume fraction of 10% ($\phi = 10\%$) may present values of local volume fraction of 8% or 12% due to the non-perfect manufacturing process. These variations must be considered in the behavior predictions of composite materials. Moreover, the dispersed phase size and/or size distribution will modify the composite's effective properties alongside the volume fraction [17, 37].

2.1.4 Model materials

When studying material systems or phenomena that are difficult to analyze — because of scale, shape, opacity, or other issues — strategies have to be adopted to evaluate such materials or phenomena. One strategy is the use of model materials. These, are materials specially designed for research purposes, making feasible or easier the understanding of complex materials or phenomena. The goal is to create the conditions for a more predictable response, mitigating the influence of secondary effects, allowing for an easier comparison with analytical and numerical models. It is not about neglecting the study of the behavior of real complex systems, but a way to investigate independently different aspects that produce a given phenomenon. Therefore, it is not a material commonly used in the industry, but one that helps to investigate and solve industrial and scientific problems. An example of the use of model materials can be seen in Figure 2.1, which shows a real material system and a simplified one.

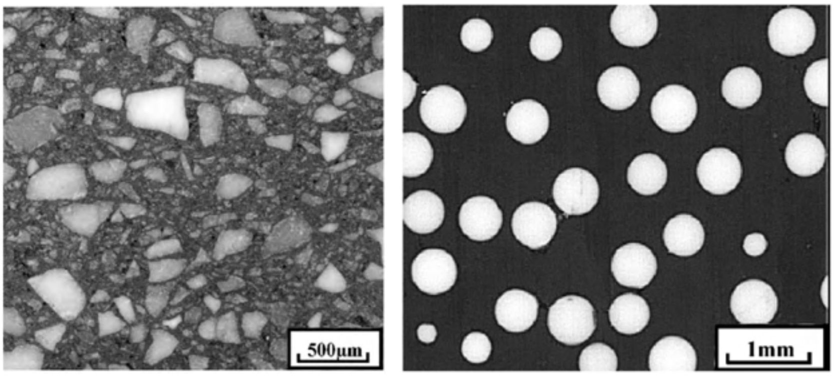

(a) (b)

Figure 2.1: Micrographs of (a) industrial refractory and (b) a simplified model material [39].

Many researchers that study crack phenomena in composite materials made use of Model composite systems (MCSs) experimentally and computationally to enable the conduction of their investigations [17, 18, 36, 37, 39, 40, 52–54]. In the study field of thermal stress in composite materials, it is interesting to contextualize model composites adopted in some important research related to this thesis.

Davidge and Green [17] developed translucent matrix model composites to visualize the position of inclusions within the matrix phase. In addition, the composite constituents were selected to present phases with similar and distinct thermal expansion coefficients to evaluate the result of the manufacturing process, which involves a temperature variation. Spheres of thoria were used as the dispersed phase, and different glass matrices as the continuous phase. Different types of cracks could be observed in the experiments depending on the CTE relation of the phases, as can be seen in Figure 2.2 [17].

A close experimental procedure as the one employed by Davidge and Green[17] was performed by André et al. [55], which adopted alumina spheres instead of thoria to create glasses matrix MCSs. Their goal was to develop a reliable numerical model to predict the amount of damage resultant in the materials manufacture and evaluate it experimentally. The model material of the experiment performed

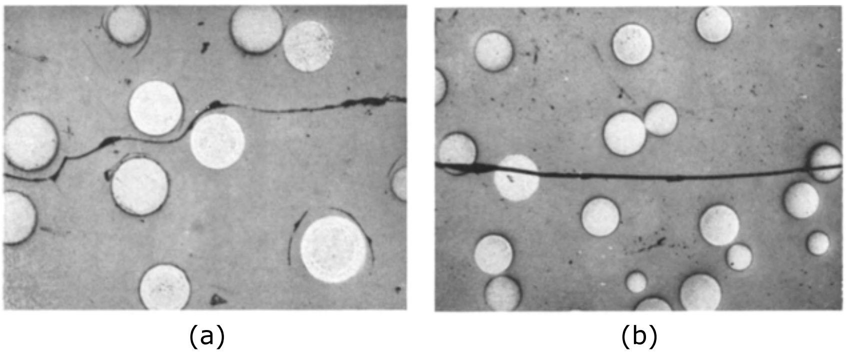

Figure 2.2: MCS of thoria spheres into different glasses matrices, with CTE mismatch between the phases of each MCS after a temperature variation. (a) Circumferential cracks; (b) Radial cracks [17].

can be seen in Figure 2.3.

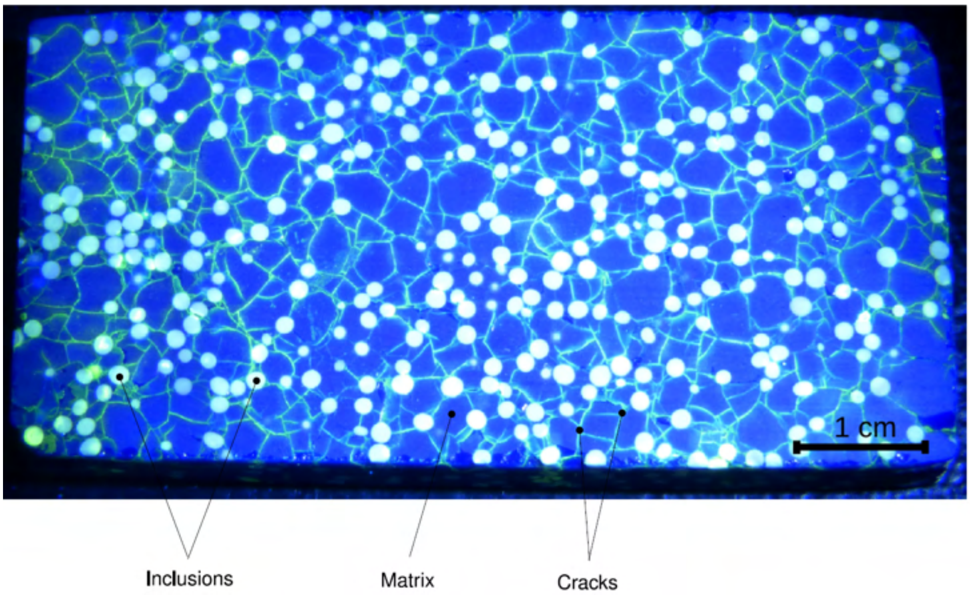

Figure 2.3: Highlight of a crack network in a MCS resultant of the manufacturing process. [55].

Joliff et al. [39] also used model composites to analyze the Young's modulus of composites formed by alumina spheres in two different glass matrices to simulate the mechanical behavior throughout the sintering process. For comparison, one glass had the same thermal expansion coefficient as alumina, while the other had a lower thermal expansion coefficient. Their study concluded that using MCS contributed to understanding the phenomena by facilitating the match between experimental and numerical results. The comparison was performed by evaluating the stiffness reduction due to the crack density increase as a function of the temperature variation.

Bobet et al. [56] conducted experiments in the fabrication of composite films to enable the application of the X-ray diffraction technique. This technique can be used in order to determine residual stresses in the material. The research aimed to study the thermal stresses caused by the manufacturing process of chemical vapor infiltration (CVI) from the dispersed phase into the continuous phase, a process typically used in manufacturing CMC's.

Llorca, Needleman and Suresh [49] performed a numerical and experimental study of the effects of voids in MMCs deformation and ductility. To obtain a high volume fraction of voids, they used two different aluminum alloys with discontinuous SiC whiskers model materials because of the knowledge of the existence of $\mathrm{Cu_2Mn_3Al_2}O$ and $\mathrm{FeCu_2Al_{17}}$ phases in such materials, which are potential void nucleation sites in order to investigate the effects of matrix void growth on deformation and ductility in metal-ceramic composites.

The studies mentioned show the relevance of applying model composite materials to observe and investigate thermal stress and fracture in composites. In addition, they highlight how the study of these materials can validate analytical and computational models. With the advance of noninvasive experimental techniques such as DIC, which provide field measurements, it is possible to expand the use of these materials to investigate more deeply the mechanical behavior of composites under temperature variation.

2.2 Mechanical and thermomechanical behavior of materials

To understand why thermal stress arises in composite systems and how it leads to crack nucleation and propagation, some essential concepts of materials mechanical behavior, material science, and fracture mechanics must be explained. Therefore, this section reviews these topics to base their most fundamental aspects on the present thesis.

The mechanical and thermomechanical behavior of materials demand analysis in different structural scales to interpret their physical response. On the atomic scale, there is how the atoms in the material bond together; on the microstructural or grain scale, there are the grains size and shape, distribution of phases, and the distribution of structural defects; and at the meso and macroscale there are the porosity, surface finish and other aspects that result from processing [46], being that all these different scales will impact material's properties. Trying to explain how all material properties are affected by the factors of each scale exceeds the need and purpose of this thesis. Herein, the material properties of interest are presented and discussed.

When an external stimulus acts on a body, it reacts according to its intrinsic properties, which may result in the arising of internal stress and strain. These can be evaluated in a given coordinate system or evaluated in terms of invariants of the stress or strain tensor [13].

The stress (σ) is the measure of how a given load intensity is distributed on a surface or body, while the strain (ε) is the measure relative to how two material points in a body change their relative distance [15, 57]. The stress and the strain can be evaluated according to a reference system adopted or in terms of the principal values, depending on the analysis interest.

The linear elastic strain (ε^e) is the strain that is directly proportional to a stress being applied over the body according to the Hooke's law (Equation 2.1) by a material property known as the Elastic modulus (E). Usually, the linear elastic strain is presented in the domain of the small strain hypothesis.

$$\sigma = E\varepsilon^e \tag{2.1}$$

Tough, E is the resistance to elastic deformation of a material to a given normal stress.

Another material property that acts in the body is the Poisson's ratio (ν), which for common materials will inflict an inverse strain in the cross-sectional dimensions of a specimen submitted to an axial loading, as indicated in Equation 2.2

$$\nu = \frac{-\varepsilon_x}{\varepsilon_z} \tag{2.2}$$

being ε_z the strain parallel to the normal load and ε_x the strain perpendicular to the normal load [15, 57, 58]. In physics terms, the Poisson's ratio is defined as the material's capacity to maintain its original volume when deformed, being the maximum value possible 0.5 and, in theory, the minimum value -1 [15, 45, 59]. To exemplify, a lot of rubbers have a Poisson's ratio close to 0.5, which implies that its volume practically does not change when it is deformed, while a cork stopper has a Poisson's ratio close to 0, which implies that when it is forced to close a bottom its cross-sectional area does not change, being an ideal choice for such a task.

Similar to the Elastic modulus, there is the Shear modulus (μ), which will relate the elastic shear strain (γ^e) to a respective in-plane pure shear stress (τ) [15, 60].

$$\tau = \mu\gamma^e \tag{2.3}$$

The stress-strain region where these statements are valid for a material is known as the elastic region. Under these conditions, after the stress is removed from the body, it will return to its initial state with no residual strain. One important aspect to be highlighted is that the Elastic modulus and the Shear modulus of a material are intrinsically related to the microstructural scale, especially to the atomic scale, as will be discussed further.

For isotropic materials under small deformations, the stress-strain relationship can be given for any pair of elastic parameters, being that each parameter can be written in terms of two others [15]. For further interest in these relations, see Table A.1 in Appendix 1.

The plastic strain is related to creating defects in the microstructural scale, especially dislocations, and happens after the linear elastic region, as seen in Figure 2.4. The relation between the stress received and the plastic strain is non-linear and each material has a particular response depending on its microstructure characteristics. The plastic strain in the material stress-strain curve arises in the elastoplastic region. Once the stress is removed from the material in the elastoplastic strain region, the elastic strain will be removed from the body's total strain, but the plastic strain remains.

It is important to clarify at this point that some materials, like most of the ce-

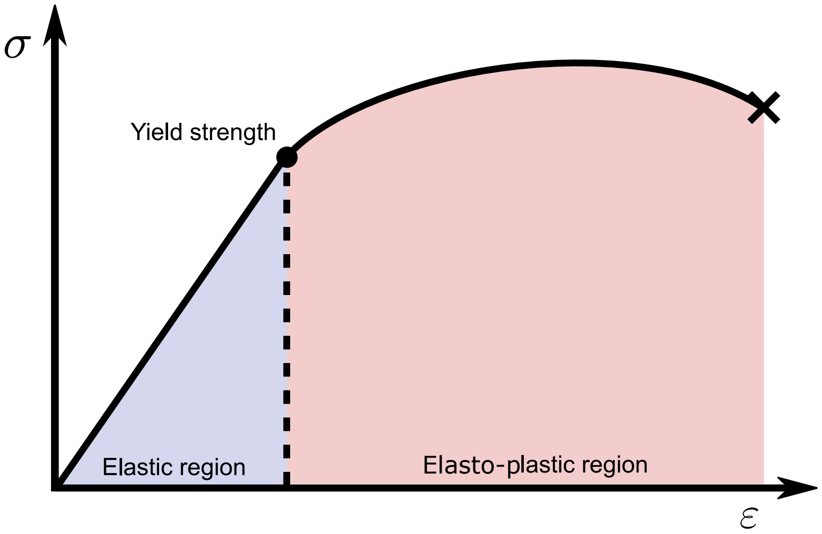

Figure 2.4: Elastic and elastoplastic regions in an engineering stress-strain curve of a ductile material with nonlinear hardening.

ramics, do not have a considerable plastic behavior when dry, as seen in Figure 2.5. Unlike metals that have simpler crystalline structures, and are governed by metallic bonds that assists plasticity, ceramic materials have more complex crystalline structures, and are governed by ionic and also the high directional covalent bonds. With that in mind, most materials can be treated in the elastic region for a lot of purposes, however, only some, like ceramics, can usually be treated as linear elastic until its fracture.

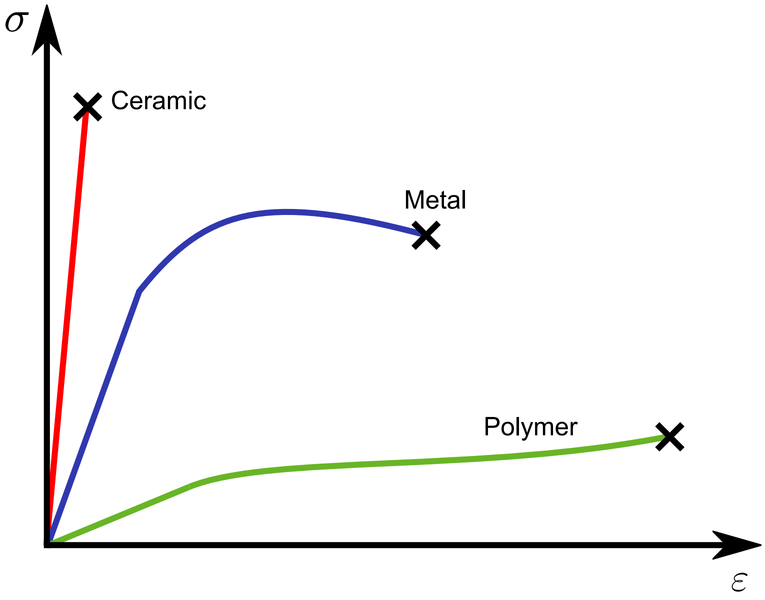

Figure 2.5: Representation of the material classes stress-strain typical behavior until fracture.

A material property of relevance to this work is the coefficient of thermal expansion (CTE, α), which relates the variation of a body dimension with its temperature variation. So, when a material has its temperature changed, a thermal strain (ε^t) appears. It is essential to know that for a given material, the coefficient of thermal expansion has different values for different temperatures.

When materials are submitted to a temperature variation, they receive or lose energy in the form of heat. This increase or decrease in energy results in an amplitude vibration change among the atomic material structure, which macroscopically can be seen by an expansion or shrinkage of the material's dimension. The CTE, is a physical property of the materials that relates a variation in length of a material to a variation in temperature in it.

One way to establish this material property is as the ratio between an infinitesimal thermal strain $d\varepsilon^t$ to an infinitesimal temperature variation dT [1]:

$$\alpha_t = \frac{d\varepsilon^t}{dT} \tag{2.4}$$

This CTE definition is tangent or differential CTE (α_t). However, a simpler and more ordinary definition is the secant or technical CTE (α_s) that is given as the relation between a resultant thermal strain to a temperature variation ΔT, with respect to a reference temperature, that produces it:

$$\alpha_s = \frac{\Delta L}{L_0\,\Delta T} \tag{2.5}$$

where ΔL is the change in length and L_0 is the length in the initial temperature. Despite being a simpler manner to measure the CTE value, the reference temperature used to measure this parameter will influence in the result, furthermore, $\alpha_s \rightarrow \alpha_t$ as the relationship between strain variation and temperature variation tends to be linear. If this rate between strain and temperature is non-linear for a material, using α_s would be unwise for an analysis [61].

The CTE measurement of materials is of high importance in a range of engineering processes, whether for the project of components regarding their application, their response during steps in its manufacture, or the impact on effective properties of materials. Furthermore, in composite systems, the CTE mismatch between phases is an intrinsic problem in the manufacturing process that requires temperature variation and in applications where composites are subjected to temperature variations[18, 32]. In these cases, stress among the phases arises that may result in material damage or failure. Further physical interpretation of the CTE is explored ahead.

2.2.1 Atomic bonds, potential energy and interatomic distance

A lot can be understood at the atomic level by looking at the atomic bonds. Equal or distinct elements can establish bonds according to the electronic behavior of the elements and the environment possibilities – pressure, temperature, atoms, or molecules to bond, etc. The periodic table of elements classifies the elements as metals, nonmetals and noble gases, being that the last ones are already stable and so will no longer be discussed. With the metal and nonmetal classes of elements, there are three possibilities of combination, which deliver the three types of strong bonds between atoms; the metallic (between metal elements), the covalent (between nonmetal elements), and the ionic (between a metal and a nonmetal elements). Also, there is the van der Waals interactions, which results from the interaction of polar molecules [15, 59].

Fundamentally, metals have predominantly metallic bonds, ceramics have predominantly ionic and/or covalent bonds and polymers have predominantly covalent and van der Waals interactions. The importance of this knowledge resides in the understanding that the metallic non-directional bonds make metals resistant, tough and yet ductile. Despite the covalent bond, the weak van der Waals bonds make polymers have low melting points and strength but have high deformation capacity. Lastly, the covalent and ionic bonds make ceramics have high melting points, Elastic modulus, but contribute to its brittleness due to the directionality and strength of these bonds [15, 59].

Each bond between atoms or ions has a particular strength that can graphically be expressed in terms of the potential energy in relation to the interatomic distance between two atoms. The total potential energy is obtained by the sum of the attraction energy and repulsion energy, obtained by integrating the attraction and repulsion forces by the interatomic distance. In this graph, the minimum energy value represents the distance where the sum of the attraction and repulsion forces equals zero. This means that in the absence of external energy, the distance between the atoms at best stability is $d0$, in which the minimum energy is represented as $E0$. In Figure 2.6, it can be seen the potential energy valley resultant of the sum of attraction and repulsion energies of the interaction between two atoms [15, 59].

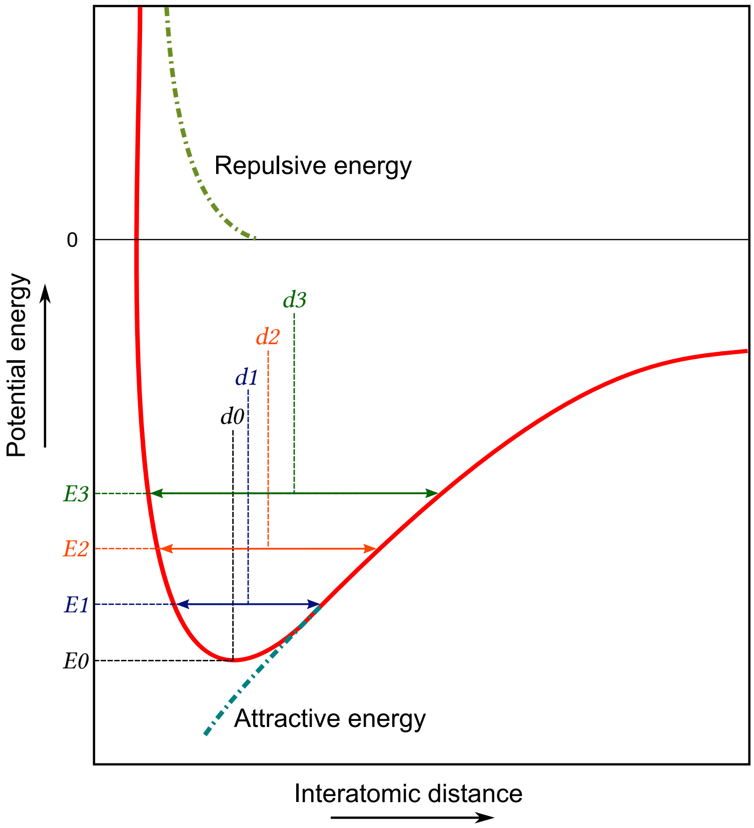

Figure 2.6: Energy valley of the interaction between two atoms in function of the interatomic distance.

The potential valley reveals many macroscopic material properties, assuming that this potential energy behavior is valid for the rest of the solid. The energy is closely related to temperature and atomic vibration. As the energy of the system increases, for example, from $E0$ to $E1$, two interesting aspects come to attention. First, for the energy $E1$, there are two stable interatomic distances, which shows that the atoms are vibrating, varying their interatomic distance between these values of interatomic distance. Second, for the asymmetry existent in the potential valley, the mean interatomic distance rises as the energy rises, which gives a physical meaning for the coefficient of thermal expansion (α). Therefore, the smaller the derivative of the potential valley higher the coefficient of thermal expansion of the material [15].

Another interesting aspect that should be observed in the potential energy valley is its depth. As can be seen, when the temperature and the energy rise in this system, the mean distance between the two atoms gets bigger until it grows exponentially, which refers to the melt of the material or the atomic separation, for example, by mechanical forces. Therefore, the deeper the valley, the larger the energy gap to separate the atoms, and consequently, the higher the melting point of the material and its elastic modulus [15].

Summing up, the element types that form a material will result in certain types of bonds, being that each bond can be analyzed in terms of the potential energy as a function of the interatomic distance. The energy displayed in the potential valley can be closely related to macroscopic material properties, such as the elastic properties and the CET.

2.2.2 Linear Elastic Fracture Mechanics (LEFM)

Fracture mechanics is an approach developed to improve the understanding of material failure on the macroscopic scale. The traditional approach to material failure analysis related only the applied stress to the yield or tensile strength, with the field of fracture mechanics development, this subject gained a new way to be analyzed. Fracture mechanics brings a more accurate method to evaluate the material failure by inter-relating the applied stress, the fracture toughness and the flaw size. The importance of fracture mechanics, especially by considering the flaws, can be exemplified once although an estimate for the cohesive strength is given by $\frac{E}{\pi}$, experimental results of brittle materials fracture strength give results three or four orders lower [13].

In the field of fracture mechanics, the most fundamental and also the first fracture topic to be approach in any general book is the Linear Elastic Fracture Mechanics (LEFM), not only because it was the first approach developed, but also in reason of its basal character that substantiate more advance concepts in fracture mechanics. The LEFM satisfies the fracture behaviour analysis of materials that fracture in the linear elastic region, like most of ceramics and some metals.

2.2.3 Basic concepts in fracture mechanics

The first concept to be explain is the strength. The strength of a material is the measure of how much stress a material can receive before it crosses some kind of limit. For example, the yield strength delimits the transition between the elastic and plastic regions; the ultimate tensile strength, the maximum tensile stress a material can reach, and the fracture strength, the stress a material is supporting when fractured. However, there is an important aspect that should be observed when looking at strength values. They usually are obtained as engineering value and not as real ones, once in the tests that they are obtained it is not considered the variation of the sample's cross-section area. Figure 2.7 exemplifies this context.

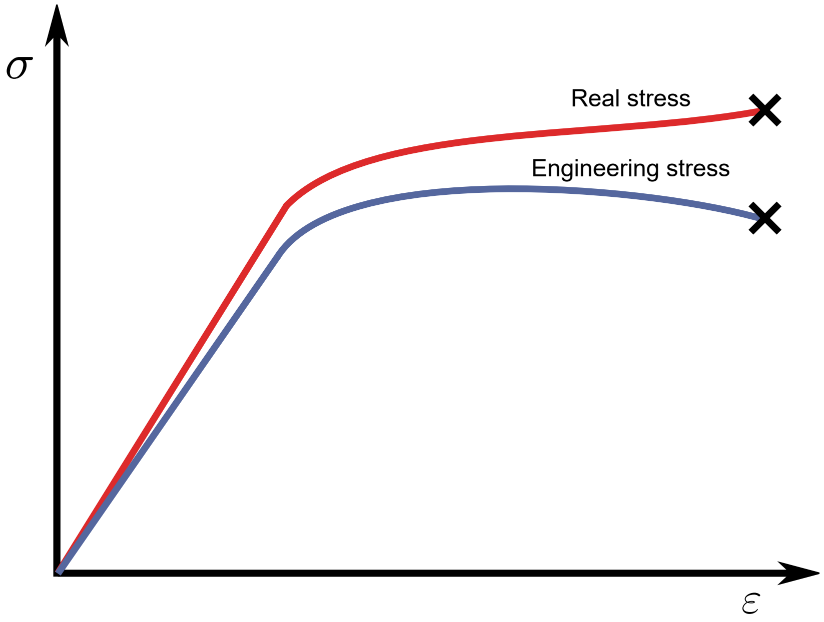

Figure 2.7: Representation of the real and the engineering stress for a tensile test in a sample material.

The toughness, on the other hand, is a measure of how much energy a material can absorb until it fractures, in other words, it is the energy of deformation per unity of volume prior to fracture, therefore the area under the stress strain curve of a material. It is also interesting to know that when only the energy necessary to pass from the elastic to the plastic region of a stress strain curve is considered, this property is known as the material resilience.For a material that has a linear elastic behavior until fracture, the material toughness and the material resilience are the same [3]. The Figure 2.8 illustrates these properties.

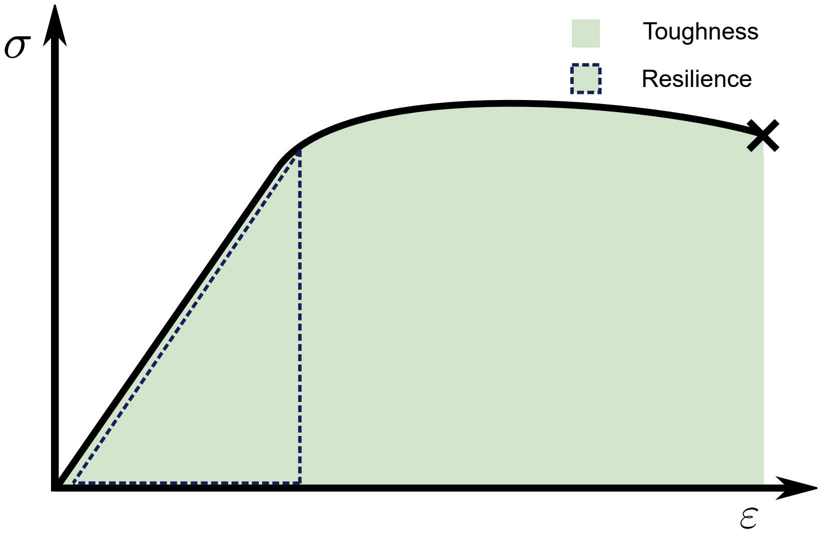

Figure 2.8: Representation of a material toughness and resilience in a stress strain curve.

Another important concept that needs to be clear is the stress concentration factor. This parameter presents how many times a flaw increases the stress in relation to the applied stress in the material or system evaluated.

A parameter related to the stress concentration factor is the fracture toughness that can be evaluated in terms of the critical stress intensity factor. The critical stress intensity factor refers to a critical value of stress concentration that implies in a crack propagation. Another parameter that can be used to evaluate the crack propagation (fracture toughness) but by an energy approach is the critical energy release rate that has a direct connection with the stress intensity factor.

The fracture energy and the energy to create a new surface are intrinsically related, once the fracture energy is the creation of two surfaces. The surface energy exists because a surface is a defect in the atomic net, once the elements in the surface are not stable for the lack of fulfillment of its bonds. So, the energy to create a crack is the energy necessary to break the atomic bonds of the fractured area.

One last concept that is important to be explained is in relation to the stability of a crack growth. The crack stability depends on the fracture toughness of the material and can be seen by the R curve. The crack growth is the dissipation of the strain energy in the material. When the stress applied in a material increases in such a way that the driving force to crack propagation is higher than the fracture resistance R, it will lead to an unstable crack propagation. However, if for example a material is submitted to a stress that will lead to a crack growth to a new stable crack size with a higher value of R, it is called a stable crack propagation.

2.2.4 Fracture initiation in the atomic level

Explained the basics about material properties, atomic bonds and other important concepts, now it will be presented a basic and simplified idea of how and why a linear elastic material fractures in the atomic level to illustrate how occurs the formation of major flaws in the material that is the main issue discussed on the field of fracture mechanics.

The initiation of a defect in the bulk of a material begins with the breach of atomic bonds or appearance of a vacancy in the net. To better comprehend the explanation, take a look at Figure 2.9. In this figure, it is possible to see in the continuous red line the resultant force of the interaction between two atoms. $d0$ is the distance where the resultant force is equal to 0, and so, the most stable distance between the atoms. To separate an atom from another, there is a cohesive force to be overcome and the energy of the bond, that is the area under the resultant force in the positive quadrant painted in red.

The cohesive strength (P) of the bond in a distance x from $d0$ can be estimated as one half of the period of a sine wave (λ_H) as can be seen in Equation 2.6

$$P(x) = P_c sin\left(\frac{\pi x}{\lambda_H}\right) \tag{2.6}$$

being P_c the cohesive force.

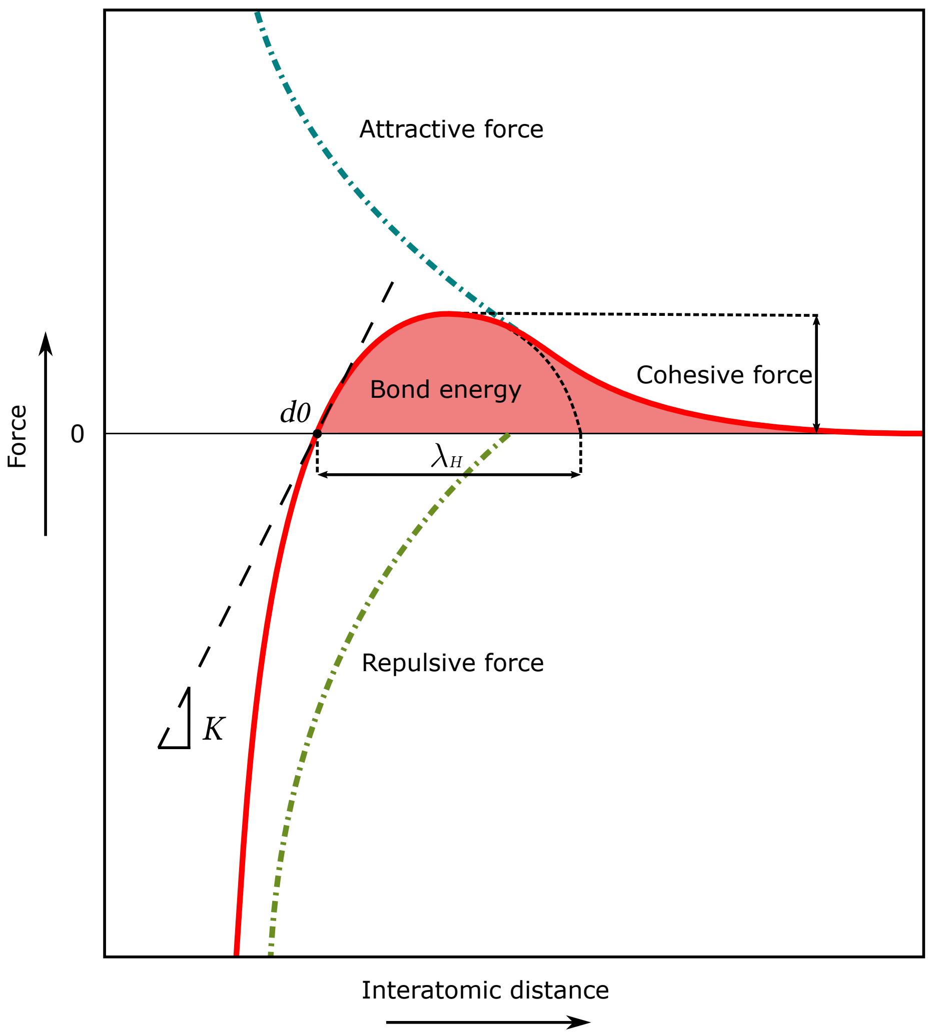

Figure 2.9: Force resultant of the interaction between two atoms in function of the interatomic distance.

For small displacements it can be established a linear relation as:

$$P(x) = P_c \left(\frac{\pi x}{\lambda_H} \right) \tag{2.7}$$

and the bond stiffness K, can be defined as:

$$K = P_c \left(\frac{\pi}{\lambda_H} \right) \tag{2.8}$$

multiplying both sides of this equation by the number of bonds per unit area and the gauge length $d0$, converts K to Young's Modulus and P_c to the cohesive stress

σ_c as can be seing in Eguation 2.9.

$$\sigma_c = \frac{E\lambda_H}{\pi d0} \tag{2.9}$$

If λ_H is approximately equal to the interatomic distance the equation can be simply written as [13]:

$$\sigma_c \approx \frac{E}{\pi} \tag{2.10}$$

The surface energy (γ_s) is equal to half of the fracture energy once the nucleation of a crack involves the creation of two surfaces, therefore the expression for the surface energy is given by:

$$\gamma_s = \frac{1}{2}\int_0^{\lambda_H} \sigma_c sin\left(\frac{\pi x}{\lambda_H}\right) dx = \sigma_c \frac{\lambda_H}{\pi} \tag{2.11}$$

Therefore, the cohesive stress can be written as:

$$\sigma_c = \frac{\gamma_s \pi}{\lambda_H} = \frac{E\lambda_H}{\pi d0} = \sqrt{\frac{\gamma_s E}{d0}} \tag{2.12}$$

Once defects in the atomic level as vacancies begin to agglomerate, they create linear and three-dimensional dislocations that eventually can result in micro-cracks. Then, with micro-cracks coalescence, they become a macro-crack that is a potential danger to the material mechanical behavior due to the stress concentration that this type of damage brings with it. Therefore, the knowledge and the processing of the microstructure scale of the material has a major part in the final mechanical properties of the material once the energy in the atomic bonds of the structure will define the creation of defects in the micro-scale and also the microstructure itself will establish the difficulty in the movement of this defects in the structure that are the beginning of micro-cracks nucleation.

2.2.5 Stress concentration approach

The importance of taking in account the flaws resides in the concentration of stress in such defects, where the first evidence of stress concentration in flaws was provided by Inglis [62]. In his study, Inglis analyzed the stress in elliptical

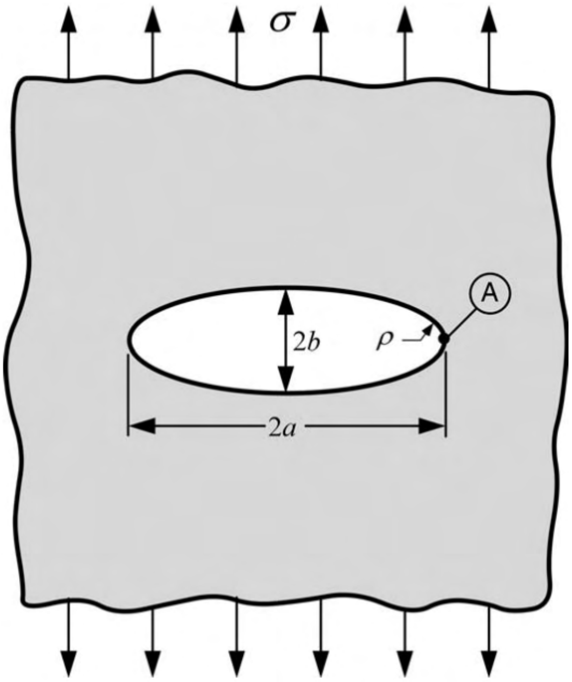

Figure 2.10: Elliptical hole in a flat plate [13].

holes in flat plates and came to an expression to evaluate the stress concentration factor. For this, it is considered an infinite plate or large enough to despise boundary effects. In this plate there is an elliptical hole of larger dimension axis $2a$ and smaller dimension axis $2b$ and also the plate is under an applied stress (σ) perpendicular to the major axis as illustrated in Figure 2.10.

By calculations Inglis concluded that the stress at the edge of the major axis (σ_a) is given by Equation 2.13: [62]

$$\sigma_a = \sigma\left(1 + \frac{2a}{b}\right) \tag{2.13}$$

As a becomes higher than b an elliptical hole becomes to take a form close to a crack, in this case it is more convenient to work in terms of the radius curvature $\left(\rho = \frac{b^2}{a}\right)$. The stress concentration factor at the tip of the hole or crack (K_t) is the ratio of σ_a for σ. Also it can be said that the curvature radius ρ for a micro-crack is close to the interatomic distance $d0$ So considering $a >> b$ K_t is given by Equation 2.14

$$\frac{\sigma_a}{\sigma} = K_t = \sqrt{\frac{4a}{\rho}} = \sqrt{\frac{4a}{d0}} \tag{2.14}$$

Finally, a rough estimate of the fracture stress for a micro-crack nucleation (σ_f) can be obtained by the combination of the Equations 2.14 and 2.12[13]:

$$\sigma_f = \sqrt{\frac{E\gamma_s}{4a}} \tag{2.15}$$

However, an important issue that must be taken into account to evaluate correctly a problem with these and other equations, is the crack size. In the model case discussed in a plate "bulk" crack, it was defined that the crack has a total length of $2a$ and a is equal to half of the crack length. However, in the case of an edge crack, the stress in function of the crack length increases by two. Therefore, a must be considered as the total crack length to obtain correct results.

2.2.6 Energy balance approach

An estate of equilibrium is the one where a material body may come to the lower potential energy as possible. Therefore, from the first law of thermodynamics, or the conservation of energy, Griffith [63], determines that the nucleation or propagation of a crack occurs to maintain the potential energy of the system (U) raised due to strain energy and external work done (Π) by converting it in work to create new surfaces (W_s). An important aspect introduced by Griffith in the development of the energy balance approach was the need to take the crack depth in consideration for real macro-cracks in engineering applications. So, he's equations are based on a very similar model and considerations of Inglis, with the exception that it is considered a crack depth B. If $a >> B$, then the two approaches will have a close answer. The energy balance proposed by Griffith in a crack area dA can be expressed according to Equation 2.16 [63]:

$$\frac{dU}{dA} = \frac{d\Pi}{dA} + \frac{dW_s}{dA} = 0 \ \ or \ \ -\frac{d\Pi}{dA} = \frac{dW_s}{dA} \tag{2.16}$$

Applying solid mechanics to calculate the variation in the mechanical potential energy of the model, Griffith came to the following equation:

$$\Pi = -\frac{\pi\sigma^2 a^2 B}{E} \tag{2.17}$$

and the work need for the creation of two new surfaces is given by:

$$W_s = 4aB\gamma_s \tag{2.18}$$

So, applying Equations 2.18 and 2.17 in Equation 2.16 the fracture stress (σ_f) for a certain crack length can be obtained as:

$$\sigma_f = \sqrt{\frac{2E\gamma_s}{\pi a}} \tag{2.19}$$

The same way, a critical crack length (a_c) for a given stress can be obtained as:

$$a_c = \frac{2E\gamma_s}{\pi\sigma^2} \tag{2.20}$$

Finally, a more common way to describe the driven force to the crack propagation is in terms of the energy release rate ($\mathcal{G}$), that is the derivative of the potential energy with respect to the crack area and can be calculated according to equation 2.21:

$$\mathcal{G} = \frac{\pi\sigma^2 a}{E} \tag{2.21}$$

Being that the energy release rate that relates an σ_f to an a_c is the fracture toughness criterion known as critical energy release rate ($\mathcal{G}_c$) or as more popular known the fracture resistance R. When $\mathcal{G} \geq R$ crack propagation occurs.

2.3 Cracks in composite materials due to CTE mismatch and temperature variation

This section presents how composite systems are affected by temperature variation and what kind of mechanical response can be expected of a material's phase CTE mismatch. To properly present the subject, some solid mechanics theory is presented, and then, used to analytically approach the issue of interest.

2.3.1 Displacements, strain and stress in a solid

From observing the stress state in an infinitesimal element of a continuous solid in the absence of volume forces, it is possible to calculate the sum of the resulting forces for each direction of the used coordinate system. The divergence of the stress tensor ($\nabla \cdot \boldsymbol{\sigma}$), which describes the result of this sum, must be null for the body to be in equilibrium:

$$\nabla \cdot \boldsymbol{\sigma} = \mathbf{0} \tag{2.22}$$

where ∇ is described according to the adopted coordinate system. The present research project analyzes the solid in a quasi-static condition, so the acceleration components are neglected.

Once the equilibrium conditions are established, the compatibility relationships allow the determination of an expression that relates displacements and strains. The expression for the obtained strain tensor is given by:

$$\boldsymbol{\varepsilon} = \frac{1}{2}\left(\nabla \mathbf{u} + \nabla \mathbf{u}^{\mathbf{T}}\right) \tag{2.23}$$

where $\mathbf{u}$ is the offset field.

The relationships between stresses and strains can be written from the generalized Hooke's Law, i.e.:

$$\boldsymbol{\sigma} = \mathbf{C} : \boldsymbol{\varepsilon}^{e} \tag{2.24}$$

being $\boldsymbol{\sigma}$ the stress tensor, $\mathbf{C}$ the constitutive tensor of the material and $\boldsymbol{\varepsilon}^e$ the elastic strain tensor of the material. For an isotropic material, the Equation (2.24) can be rewritten, using the Lamé parameters (λ, μ), such as:

$$\boldsymbol{\sigma} = \lambda \boldsymbol{I} tr(\boldsymbol{\varepsilon}^{e}) + 2\mu \boldsymbol{\varepsilon}^{e} \tag{2.25}$$

When a material is subjected to temperature variation, the total strain ($\boldsymbol{\varepsilon}$) is that resulting from the sum of the elastic ($\boldsymbol{\varepsilon}^e$) and thermal ($\boldsymbol{\varepsilon}^t$) – in case of disregarding any inelastic portion –, thus, the tensor of elastic strains of the material is described as:

$$\boldsymbol{\varepsilon}^{e} = \boldsymbol{\varepsilon} - \boldsymbol{\varepsilon}^{t} \tag{2.26}$$

where the thermal strain can be given by the product between the temperature variation (ΔT) and the thermal expansion coefficient (α). The thermal strains only influence the normal strains, so it follows that:

$$\boldsymbol{\varepsilon}^t = \alpha \, \Delta T \, \mathbf{I} \tag{2.27}$$

where $\mathbf{I}$ is the identity tensor.

Once the constitutive (Equation (2.25)), compatibility (Equation (2.23)) and equilibrium (Equation (2.22)) equations have been developed, it is possible to combine them in order to find a general solution to a set of problems. During the development of analytical models, boundary conditions must be used to find the parameters referring to the model solution for a specific problem. In the next section, the relationships presented here are applied to the problem of a cylindrical inclusion surrounded by a matrix and subjected to a temperature variation.

2.3.2 Spherical inclusion surrounded by an infinite matrix exposed to temperature variation

The calculations for the interfacial stress arising from a temperature variation for a spherical inclusion in an infinite matrix was described by Selsing[16] and used by Davidge and Green [17]. In Selsing's work, an approach based on analytical equations for vessels thick-walled pressure was employed. A different deduction approach to the same case will be presented in here, showing how to determine the field of displacements, deformations and stresses, as well as the interfacial stress. The equations developed here are described succinctly, since a cylindrical model that will be presented in greater detail. A representation of the case described in this subsection can be seen in Figure 2.11.

The mechanical and thermomechanical properties of the inclusion and the matrix are described based on the Lamé parameters (λ and μ) and the CET (α). The sub-indices lower case i and m are used to name the inclusion and the matrix domain, respectively, and the upper case I and M are used when referring to intrinsic properties of the inclusion and matrix, respectively. The domain occupied by the inclusion is defined by $r \in [0, r_i]$ and the matrix domain by the complementary region, $r \in (r_i, \infty)$. The adopted boundary conditions are the symmetry of revolution around the θ and ϕ axes; the restriction of displacements from the

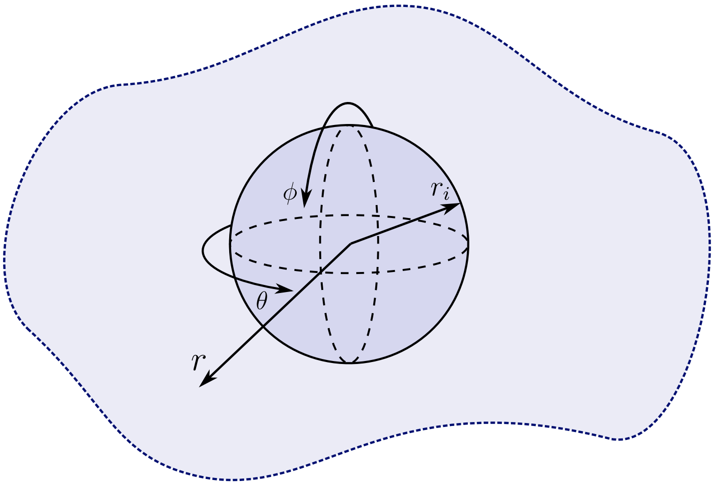

Figure 2.11: Spherical inclusion surrounded by an infinite matrix.

center of inclusion; and that the stress components, in particular the radial component, tends to zero as the radius tends to infinity ($\lim_{r\to\infty}\sigma_{rr}(r) = 0$).

In spherical coordinates, once the hypothesis of symmetry of revolution is adopted for the θ and ϕ directions, it can be considered that the normal deformations in each of these directions are equivalent and that the derivatives as a function of θ and ϕ are null. Therefore, the compatibility relations between deformation and displacement for this case can be written as:

$$\begin{aligned} \varepsilon_{rr} &= \frac{\partial u_r}{\partial r} \\ \varepsilon_{\theta\theta} &= \varepsilon_{\phi\phi} = \frac{u_r}{r} \\ \varepsilon_{r\theta} &= \varepsilon_{r\phi} = \varepsilon_{\theta\phi} = 0 \end{aligned} \tag{2.28}$$

In order to obtain the stresses from the deformations, Hooke's Law generalized for spherical coordinates is adopted using Lamé parameters:

$$\begin{aligned}
\sigma_{rr} &= \lambda(\varepsilon_{rr} - \alpha\Delta T + \varepsilon_{\theta\theta} - \alpha\Delta T + \varepsilon_{\phi\phi} - \alpha\Delta T) + 2\mu(\varepsilon_{rr} - \alpha\Delta T)\\
\sigma_{\theta\theta} &= \lambda(\varepsilon_{rr} - \alpha\Delta T + \varepsilon_{\theta\theta} - \alpha\Delta T + \varepsilon_{\phi\phi} - \alpha\Delta T) + 2\mu(\varepsilon_{\theta\theta} - \alpha\Delta T)\\
\sigma_{\phi\phi} &= \lambda(\varepsilon_{rr} - \alpha\Delta T + \varepsilon_{\theta\theta} - \alpha\Delta T + \varepsilon_{\phi\phi} - \alpha\Delta T) + 2\mu(\varepsilon_{\phi\phi} - \alpha\Delta T)\\
\sigma_{r\theta} &= 2\mu\varepsilon_{r\theta}\\
\sigma_{r\phi} &= 2\mu\varepsilon_{r\phi}\\
\sigma_{\theta\phi} &= 2\mu\varepsilon_{\theta\phi}
\end{aligned} \tag{2.29}$$

Then, introducing the compatibility equations (Equation (2.28)) into Equation (2.29), we have:

$$\begin{aligned}
\sigma_{rr} &= (\lambda + 2\mu)\left(\frac{\partial u_r}{\partial r} - \alpha\Delta T\right) + 2\lambda\left(\frac{u_r}{r} - \alpha\Delta T\right)\\
\sigma_{\theta\theta} = \sigma_{\phi\phi} &= (2\lambda + 2\mu)\left(\frac{u_r}{r} - \alpha\Delta T\right) + \lambda\left(\frac{\partial u_r}{\partial r} - \alpha\Delta T\right)\\
\sigma_{r\theta} = \sigma_{r\phi} &= \sigma_{\theta\phi} = 0
\end{aligned} \tag{2.30}$$

Checking the balance of the body (Equation 2.22), we obtain:

$$\frac{\partial \sigma_{rr}}{\partial r} + \frac{2}{r}(\sigma_{rr} - \sigma_{\theta\theta}) = 0 \tag{2.31}$$

and, substituting the equations of σ_{rr} and $\sigma_{\theta\theta}$ into the equilibrium equation, an ordinary second-order differential equation is obtained, whose solution is the radial displacement field, i.e.:

$$\frac{d^2 u_r}{dr^2} + \frac{2}{r}\frac{du_r}{dr} - \frac{2u_r}{r^2} = 0 \tag{2.32}$$

The general solution of Equation (2.32) is given by:

$$u_r = A\,r + \frac{B}{r^2} \tag{2.33}$$

where the constants A and B must be identified based on the boundary conditions of the problem. As there are two regions with different properties (inclusion and matrix), there are four parameters to be identified: A_i, B_i, A_m and B_m.

The boundary conditions of the problem are $u_r(r=0)=0$, $\lim_{r\to\infty}\sigma_{rr}(r)=0$, and the condition of continuity of displacements and radial stresses at $r=r_i$. From the first boundary condition, $B_i=0$ is obtained, making the displacement in the inclusion domain depend exclusively on the term A_i. The second condition allows us to identify that $A_m=\alpha_m\Delta T$.

To obtain the interface radial stress equation in order to compare it with the Selsing expression, it is then necessary to establish a system of equations based on the continuity conditions in $r=r_i$, i.e.:

$$\frac{B_m}{r_i^3}=A_i-\alpha_m\Delta T \tag{2.34}$$

$$(A_i-\alpha_i\Delta T)(3\lambda_I+2\mu_I)+\frac{4B_m\mu_M}{r_i^3}=0 \tag{2.35}$$

Substituting Equation 2.34 into Equation 2.35 we obtain that:

$$A_i=\frac{((3\lambda_I+2\mu_I)\alpha_i+4\mu_M\alpha_m)\Delta T}{3\lambda_I+2\mu_I+2\mu_M} \tag{2.36}$$

Thus, the radial interface stress is written as follows:

$$\sigma_{rr}(r_i)=-(3\lambda_I+2\mu_I)(A_i-\alpha_i\Delta T) \tag{2.37}$$

and subsequently, using the A_i expression, an equation equivalent to that described by Selsing for the interface pressure (here described in Lamé parameters) is obtained:

$$\sigma_{rr}(r_i)=-\frac{4\mu_M(3\lambda_I+2\mu_I)(\alpha_i-\alpha_m)\Delta T}{3\lambda_I+2\mu_I+4\mu_M} \tag{2.38}$$

2.3.3 Interfacial stress in a spherical inclusions composite system due to temperature variation – A parametric investigation

A sensitive and straightforward parameter to begin with is the coefficient of thermal expansion (CTE) which has a clear influence in the stress state of composite systems submitted to a temperature variation. It is important to clarify that the CTE is an intrinsic material property that is not affected by discontinuities in the material medium, being that a solid plate or a porous one made of the same material and with the same dimensions will respond in the same way to a temperature variation assuming that there are no restrictions to its expansion.

To show the effect of the CTE in a heterogeneous system, one may observe a system composed of a spherical inclusion inside a representative volume of an infinite matrix. The inclusion has a radius r_i (at room temperature) and a CTE α_I, and the matrix has a centered hole with a radius r_i and a CTE α_M. If these phases are assembled at room temperature assuming a perfect interface condition, one can describe the thermomechanical behavior of this simplified system when it is submitted to a temperature variation (Figure 2.12).

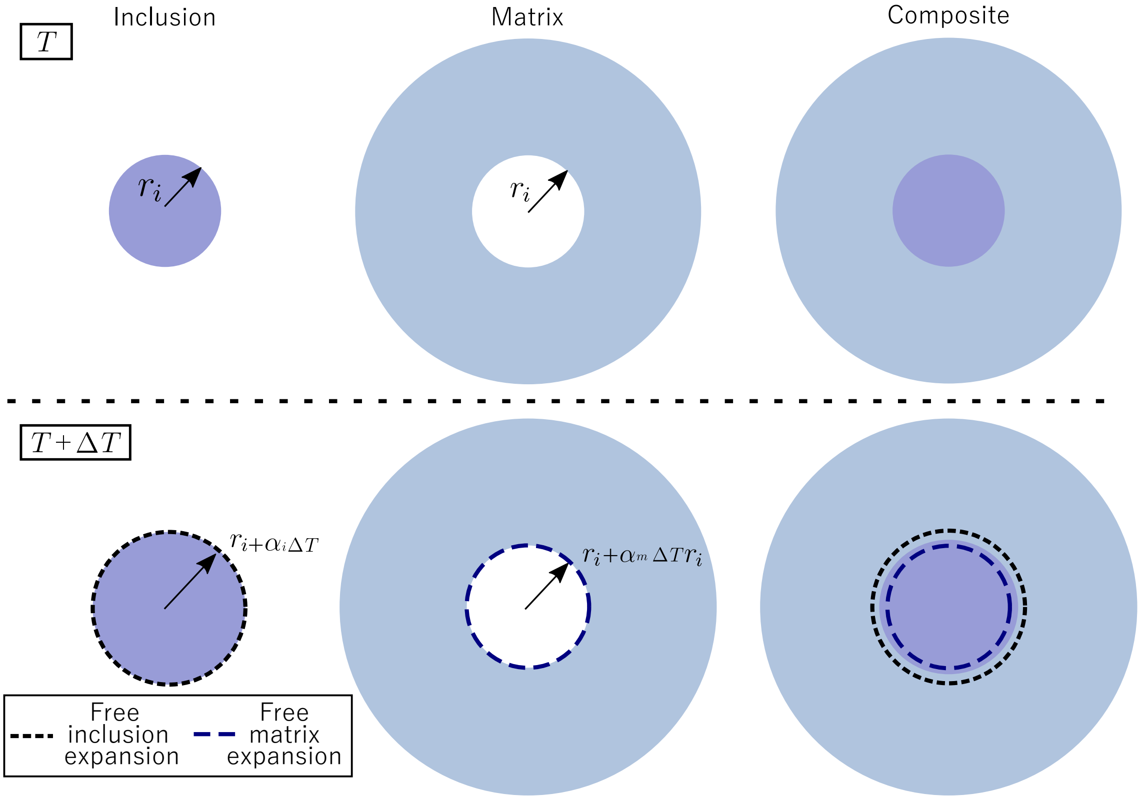

Figure 2.12: Representation of the response of a heterogeneous system with different CTEs phases to a temperature variation.

Therefore, it can be seen that for a $\alpha_I \neq \alpha_M$, with a temperature variation, interfacial stress will arise since each of the phases expands with a different magnitude, and the greater the difference between the thermal expansion coefficients of the materials, the greater will be the stress. Thus, the CTE is a key parameter when only thermal loads are applied. Other material properties also influence the stress in heterogeneous systems submitted to temperature variations. However, if there is no CTE mismatch between the phases, other material properties will no longer influence the thermomechanical response since no thermal stress will appear from a temperature variation.

For a more convenient approach to the reader, it will be presented first the influence of more traditional elastic properties effects in the interfacial stress for a temperature variation as described in the example mentioned, and after other elastic parameters influence that represents more physically the problem.

The interfacial radial stress $\sigma_{rr}(r_i)$ for a single inclusion embedded in an infinite matrix as a function of the Young modulus E, the Poisson's ratio ν and the CTE α of the matrix ($_m$) and inclusion ($_i$), can be described according to Selsing's equation [16]:

$$\sigma_{rr}(r_i) = -\frac{(\alpha_I - \alpha_M)\,\Delta T}{\dfrac{1+\nu_m}{2E_m} + \dfrac{1-2\nu_i}{E_i}} \tag{2.39}$$

The Young modulus represents the stiffness of the material. The first aspect to observe is that the position of the interface matrix/inclusion in reason of a temperature variation will be very influenced by the stiffness relationship between the phases once the stiffest material, with a higher Young's modulus, will have more weight in the imposition of the final position of the interface after a temperature variation. Concerning the interfacial stress of the system, the higher Young's modulus of the phases, the higher the interfacial stress will be.

The Poisson's ratio is not a simple property to be interpreted in the evaluation of interfacial stress, even in this simplified system. Evaluating its value from 0 to 0.5, the interfacial stress will increase as the matrix Poisson's ratio is higher and as the inclusion Poisson's ratio is lower.

To illustrate the mechanical properties influence on the interfacial stress as described in the previous paragraphs, the Figure 2.13 presents an example using the Selsing's equation to compute the interfacial stress. In the Figure 2.13, a standard materials properties and temperature variation are defined and to each plot it can be seen the interfacial stress variation for a set of Poisson's ratio of one of the phases and for a variation of Young's modulus of one of the phases. The standard condition is: $E_I = E_M$ = 100 GPa; $\nu_I = \nu_M$ = 0.25; $\alpha_I = 20^{-5}\,°$C^{-1}; $\alpha_M = 10^{-5}\,°$C^{-1}; ΔT = 100 °C.

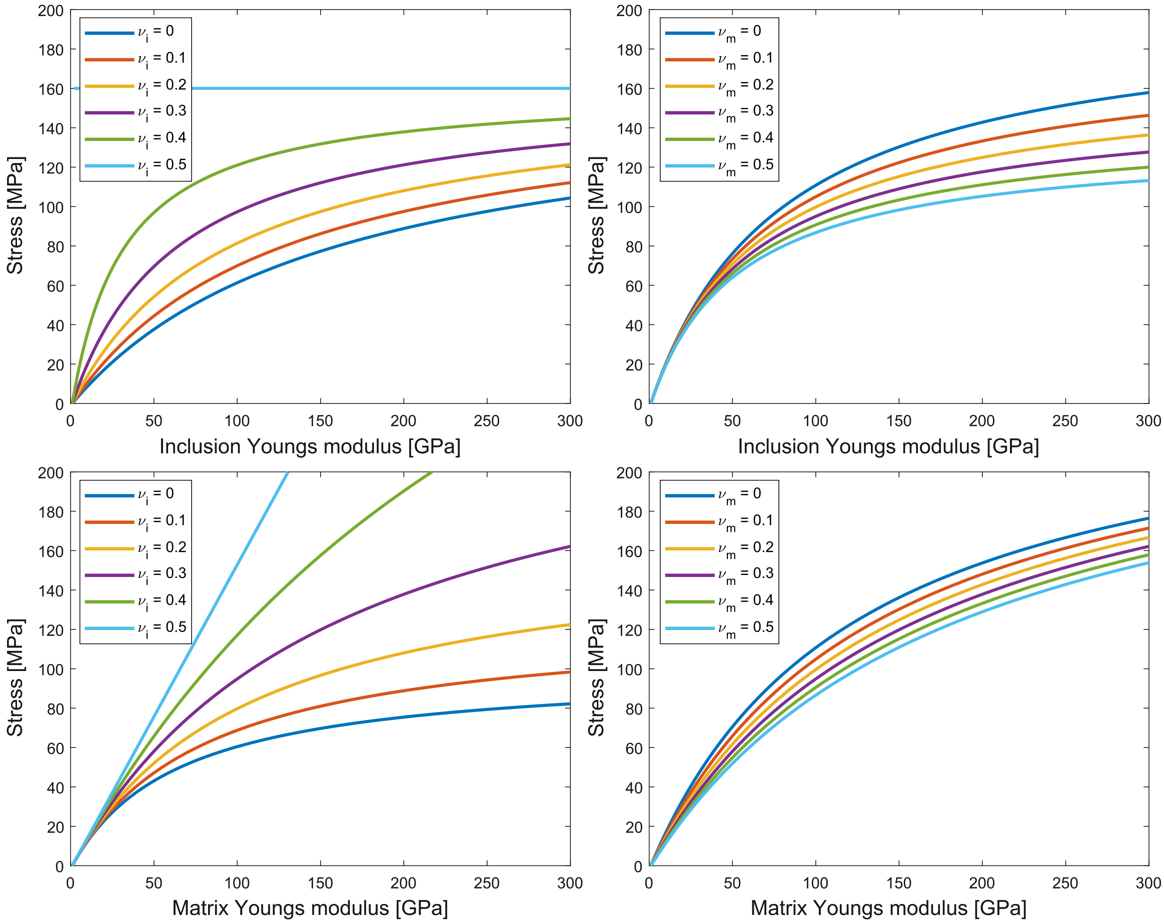

Figure 2.13: Influence of Young's modulus and Poisson's ratio for different matrix and inclusion properties variation in the interfacial stress resultant of a homogeneous temperature variation of a single inclusion in an infinite matrix. where the standard conditions are: $E_I = E_M$ = 100 GPa; $\nu_I = \nu_M$ = 0.25; $\alpha_I = 20^{-5}\,°$C^{-1}; $\alpha_M = 10^{-5}\,°$C^{-1}; ΔT = 100 °C.

By the plot analyzes it comes to attention that the Young's Modulus of the matrix and the Poisson's rate of the inclusion are quite important in the resultant stress, this aspect will become clearer with a change in perspective by a re-written of Selsing's equation using other elastic constants.

Selsing's equation can be written in other mechanical properties, as the Lame's parameters (λ and μ) as done by Zago [64]:

$$\sigma_{rr}(r_i) = -\frac{4\mu_M(3\lambda_I + 2\mu_I)(\alpha_I - \alpha_M)\Delta T}{3\lambda_I + 2\mu_I + 4\mu_M} \tag{2.40}$$

Comparing Equations 2.39 and 2.40 it comes to attention that in the second one, the interfacial radial stress depends only on one elastic parameter from the matrix (μ_M), which brings the possibility that the inclusion parcel could also be described by only one parameter, which happens to be true. Then, the interfacial radial stress for a single inclusion embedded in an infinite matrix can be expressed in terms of the Bulk modulus of the inclusion and the Shear modulus of the matrix as:

$$\sigma_{rr}(r_i) = -\frac{12K_I\mu_M(\alpha_I - \alpha_M)\Delta T}{3K_I + 4\mu_M} = -\frac{(\alpha_I - \alpha_M)\Delta T}{\dfrac{1}{3K_I} + \dfrac{1}{4\mu_M}} \tag{2.41}$$

Therefore, an analysis using the same standard properties as before to evaluate the influence of the Bulk modulus of the inclusion (K_I) and the Shear modulus of the matrix (μ_M) can be observed in Figure 2.14. For the variation of each property, the other remain constant in a standard condition. Despite not being the most common couple of mechanical properties to describe the thermo-elastic mechan-

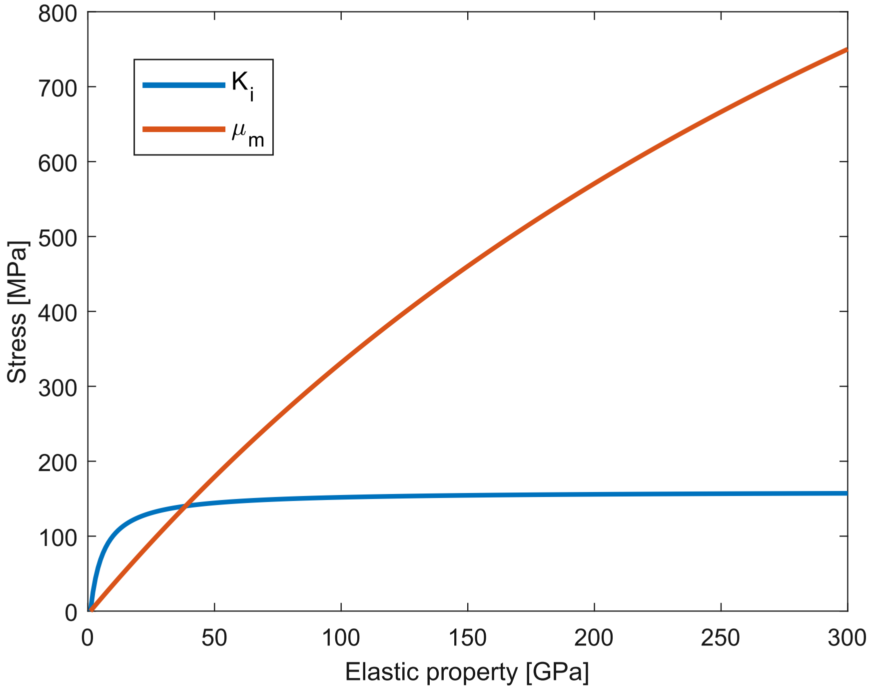

Figure 2.14: Influence of the Bulk modulus of the inclusion and the Shear modulus of the matrix in the interfacial stress as a result of a temperature variation. For the stress varying K_I, $E_M = 100$ GPa; $\nu_M = 0.25$, and for the stress varying μ_M, $E_I = 100$ GPa; $\nu_I = 0.25$.

ical behavior of a problem, it is interesting that only one mechanical property of each phase is enough to describe the interfacial stress behavior of this system, which is quite helpful to physically understand the phase's interaction mechanical response in reason of a temperature variation. To digress in, why ν_I is such a sensible elastic property for the interfacial stress, when $\nu_I \rightarrow 0.5 \; K_I \rightarrow \inf$.

The summarized influence of the discussed elastic parameters in the interfacial radial stress can be seen in Figure 2.15.

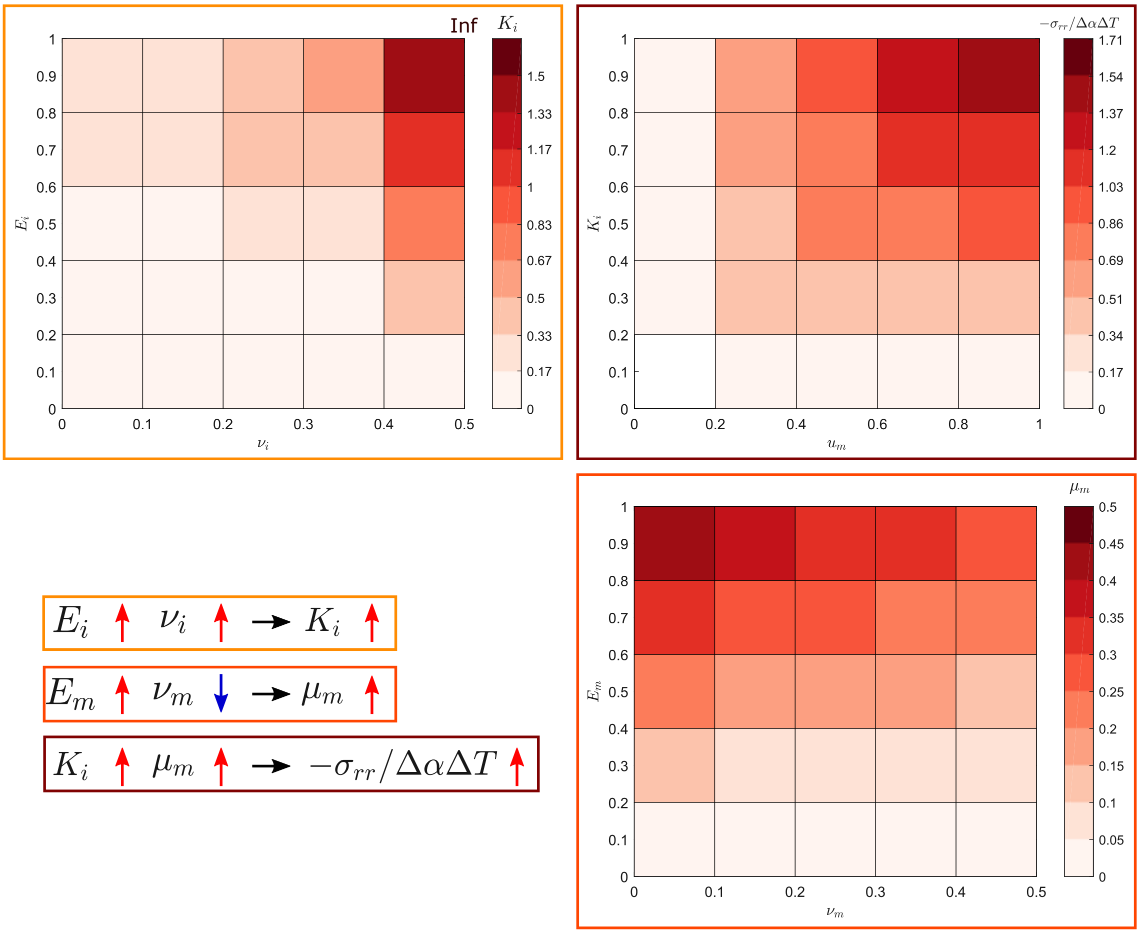

Figure 2.15: Sensibility of the Young's Modulus and Poisson's ratio in the Bulk and Shear modulus, and sensibility of the Bulk and Shear modulus in the interfacial radial stress.

Driven by the interest to explore the interfacial stress of a single spherical inclusion inside a matrix and in order to facilitate the reader's understanding of this subject, a more elaborate chart is presented based on Equation 2.41.

In Figures 2.16 the Y axis presents the influence of the elastic parameters of the inclusion (K_I) and matrix (μ_M) in the interfacial stress. In the X axis, there are

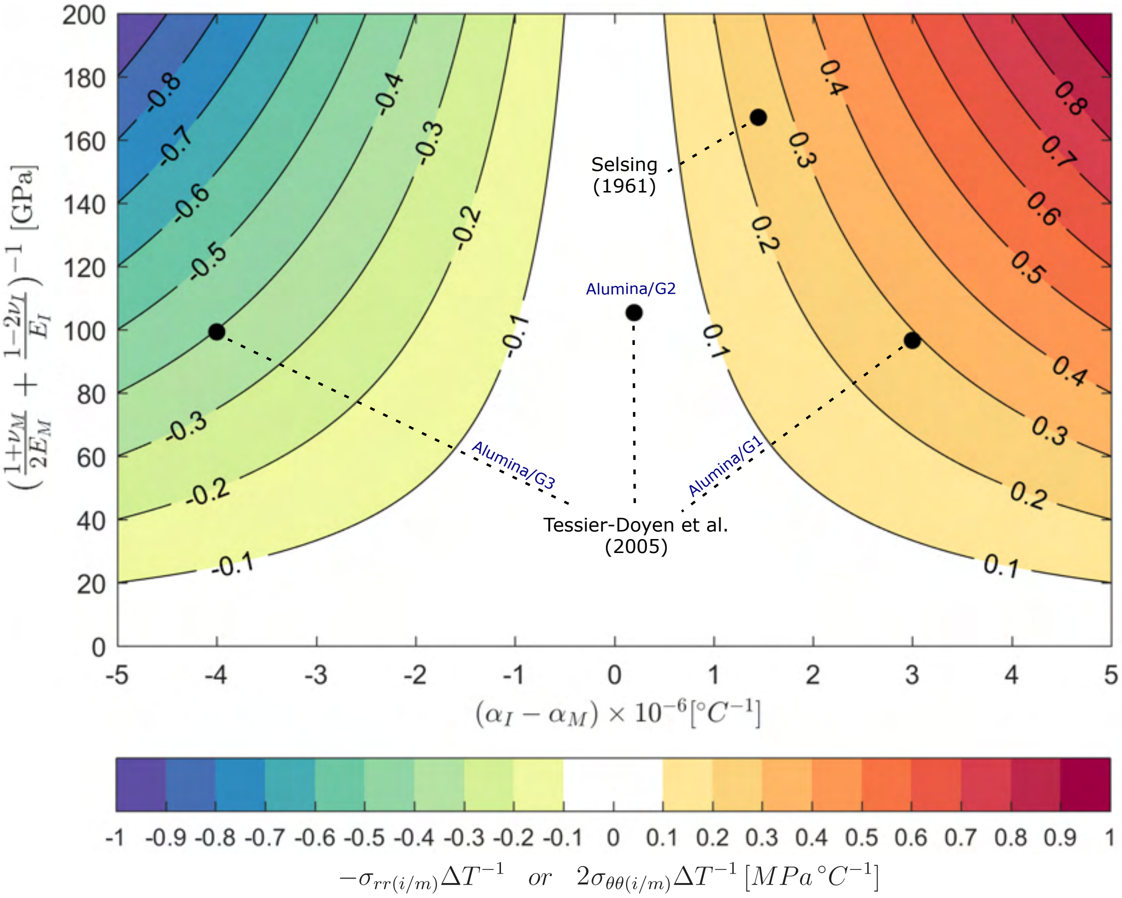

Figure 2.16: Interfacial stress caused by temperature increase for a spherical inclusion into an infinite matrix as a function of the inclusion and matrix elastic parameters, and the mismatch between the phases ($\alpha_I - \alpha_M$), for the matrix domain [16, 18]. This diagram is a graphical display based on Equation 2.39, where the interfacial stress per °C of a biphasic system can be represented by a point. The vertical axis contains the mechanical properties relation, and the horizontal axis their CTE mismatch. For example, for Selsing's system, the tangential interfacial stress will increase for each degree Celsius of temperature in ~0.25 MPa.[65]

values for the CTE mismatch between the phases, considering the CTE mismatch as $\alpha_I - \alpha_M$. Finally, the color map presents the resultant interfacial stress values per °C of temperature variation. These values of stress are computed considering a perfect interface condition between the phases. An aspect that is important to emphasize is that the values presented are the ones in the matrix' domain of the interface. While the radial stress is continuous when transitioning from the inclusion's to the matrix' domain, the tangential stress has opposite signs in each domain. Also, knowing that the tangential stress for this spherical case has half the magnitude and opposite sign as the radial stress for the matrix domain, it can be easily obtained according to:

$$-\sigma_{rr} = 2\sigma_{\theta\theta} = 2\sigma_{\phi\phi} \tag{2.42}$$

2.3.4 Analytical model for a single cylindrical inclusion into an infinite matrix

In here it is presented equations developed to attain an analytical model describing the displacement of a single cylindrical inclusion embedded in a matrix under temperature variation. This model was used to understand the interaction between the phases and also for some post-processing of the experimental results.

The analytical model represents a single cylindrical inclusion of radius r_i into an infinite matrix (Figure 2.17). The equations were developed in cylindrical coordinates, with the origin of the coordinate system being the center of the circle, which represents a cylindrical inclusion whose faces are parallel to the plane (r,θ). It is important to reiterate that the terms with sub-index i are properties or parameters referring to the inclusion phase, while those with sub-index m are properties or parameters referring to the matrix phase. Thus, λ_I, μ_I and α_I refer to the inclusion's properties, and λ_M, μ_M and α_M refer to the matrix' properties. The inclusion is defined for $r \in [0, r_i]$ and the matrix phase in the complementary region, $r \in (r_i, \infty]$.

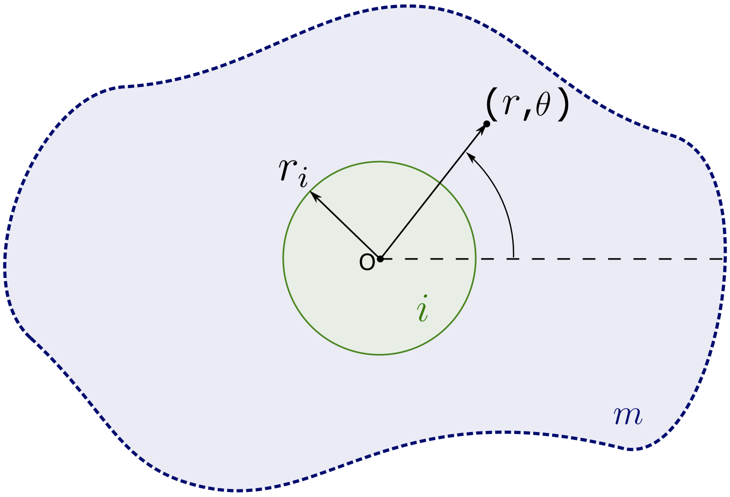

Figure 2.17: Cylindrical inclusion into an infinite matrix [65].

Four conditions define the problem. The first boundary condition established is the radial restriction of motion of the center of the inclusion ($u_r(r = 0) = 0$). A condition of perfect interface between inclusion and matrix was also assumed, that is, $u_{r_i}(r_i) - u_{r_m}(r_i) = 0$ and ($\sigma_{rr_i}(r_i) = \sigma_{rr_m}(r_i)$). Finally, only the action of temperature variation is considered, so when the matrix radius tends to infinity, any stress in the system, in particular the radial stress σ_{rr} will tend to zero ($\lim_{r\to\infty} \sigma_{rr}(r)$ = 0).

The problem is axisymmetric around the axis z, so the stress, strain or displacement values for a given radius around this axis have the same value, regardless of the angle θ.Finally, as the model describes a cross-section of the matrix and fiber in the fiber's transverse direction, it is considered that, with the axis z in cylindrical coordinates being the longitudinal axis of the fiber, there is no variation in the results for different values of z.

In cylindrical coordinates the elastic strain tensor can be written from Equation 2.26 as follows:

$$\boldsymbol{\varepsilon}^{\mathrm{e}} = \begin{bmatrix} \varepsilon_{rr} - \alpha\Delta T & \varepsilon_{r\theta} & \varepsilon_{rz} \\ \varepsilon_{r\theta} & \varepsilon_{\theta\theta} - \alpha\Delta T & \varepsilon_{\theta z} \\ \varepsilon_{rz} & \varepsilon_{\theta z} & \varepsilon_{zz} - \alpha\Delta T \end{bmatrix} \tag{2.43}$$

then using the 2.25 Equation, one can write the generalized Hooke's Law for a plane (r, θ):

$$\boldsymbol{\sigma} = \begin{bmatrix} \lambda & 0 & 0 \\ 0 & \lambda & 0 \\ 0 & 0 & \lambda \end{bmatrix} \left(\varepsilon_{rr} + \varepsilon_{\theta\theta} + \varepsilon_{zz} - 3\alpha\Delta T \right) + 2\mu \begin{bmatrix} \varepsilon_{rr} - \alpha\Delta T & \varepsilon_{r\theta} & \varepsilon_{rz} \\ \varepsilon_{r\theta} & \varepsilon_{\theta\theta} - \alpha\Delta T & \varepsilon_{\theta z} \\ \varepsilon_{rz} & \varepsilon_{\theta z} & \varepsilon_{zz} - \alpha\Delta T \end{bmatrix} \tag{2.44}$$

Thus, the equations that describe the components of the tensor $\boldsymbol{\sigma}$ are obtained:

$$
\begin{aligned}
&\sigma_{rr} = \lambda(\varepsilon_{rr} - \alpha\Delta T + \varepsilon_{\theta\theta} - \alpha\Delta T + \varepsilon_{zz} - \alpha\Delta T) + 2\mu(\varepsilon_{rr} - \alpha\Delta T) \\
&\sigma_{\theta\theta} = \lambda(\varepsilon_{rr} - \alpha\Delta T + \varepsilon_{\theta\theta} - \alpha\Delta T + \varepsilon_{zz} - \alpha\Delta T) + 2\mu(\varepsilon_{\theta\theta} - \alpha\Delta T) \\
&\sigma_{zz} = \lambda(\varepsilon_{rr} - \alpha\Delta T + \varepsilon_{\theta\theta} - \alpha\Delta T + \varepsilon_{zz} - \alpha\Delta T) + 2\mu(\varepsilon_{zz} - \alpha\Delta T) \\
&\sigma_{r\theta} = 2\mu\varepsilon_{r\theta} \\
&\sigma_{rz} = 2\mu\varepsilon_{rz} \\
&\sigma_{\theta z} = 2\mu\varepsilon_{\theta z}
\end{aligned}
\tag{2.45}
$$

The strain components can be replaced using the compatibility relations, which for a system in cylindrical coordinates are expressed by:

$$\varepsilon_{rr} = \frac{\partial u_r}{\partial r} \tag{2.46}$$

$$\varepsilon_{\theta\theta} = \frac{1}{r}\frac{\partial u_\theta}{\partial \theta} + \frac{u_r}{r} \tag{2.47}$$

$$\varepsilon_{zz} = \frac{\partial u_z}{\partial z} \tag{2.48}$$

$$\varepsilon_{r\theta} = \frac{1}{2}\left(\frac{\partial u_r}{\partial \theta} + \frac{\partial u_\theta}{\partial r} - \frac{u_\theta}{r}\right) \tag{2.49}$$

$$\varepsilon_{rz} = \frac{1}{2}\left(\frac{\partial u_r}{\partial z} + \frac{\partial u_z}{\partial r}\right) \tag{2.50}$$

$$\varepsilon_{\theta z} = \frac{1}{2}\left(\frac{\partial u_\theta}{\partial z} + \frac{1\partial u_z}{r\partial \theta}\right) \tag{2.51}$$

From the application of the conditions that guarantee the axisymmetry of the problem, viz. $u_\theta = 0$ and $\partial(.)/\partial\theta = 0$, and with the introduction of the compatibility equations, the constitutive relations can be simplified and described as:

$$\sigma_{rr} = (\lambda + 2\mu)\left(\frac{\partial u_r}{\partial r} - \alpha\Delta T\right) + \lambda\left(\frac{u_r}{r} - \alpha\Delta T + \frac{\partial u_z}{\partial z} - \alpha\Delta T\right) \tag{2.52}$$

$$\sigma_{\theta\theta} = (\lambda + 2\mu)\left(\frac{u_r}{r} - \alpha\Delta T\right) + \lambda\left(\frac{\partial u_r}{\partial r} - \alpha\Delta T + \frac{\partial u_z}{\partial z} - \alpha\Delta T\right) \tag{2.53}$$

$$\sigma_{zz} = (\lambda + 2\mu)\left(\frac{\partial u_z}{\partial z} - \alpha\Delta T\right) + \lambda\left(\frac{\partial u_r}{\partial r} - \alpha\Delta T + \frac{u_r}{r} - \alpha\Delta T\right) \tag{2.54}$$

From the definition presented to obtain the equilibrium equations (Equation 2.22), the equilibrium equations in cylindrical coordinates are expressed by:

$$\begin{aligned}
\frac{\partial\sigma_{rr}}{\partial r}+\frac{1}{r}\frac{\partial\sigma_{r\theta}}{\partial\theta}+\frac{\partial\sigma_{rz}}{\partial z}+\frac{1}{r}(\sigma_{rr}-\sigma_{\theta\theta})=0\\
\frac{\partial\sigma_{r\theta}}{\partial r}+\frac{1}{r}\frac{\partial\sigma_{\theta\theta}}{\partial\theta}+\frac{\partial\sigma_{\theta z}}{\partial z}+\frac{2\sigma_{r\theta}}{r}=0\\
\frac{\partial\sigma_{rz}}{\partial r}+\frac{1}{r}\frac{\partial\sigma_{\theta z}}{\partial\theta}+\frac{\partial\sigma_{zz}}{\partial z}+\frac{2\sigma_{rz}}{r}=0
\end{aligned} \tag{2.55}$$

Again, applying the symmetry conditions, the equilibrium boils down to a single equation:

$$\frac{\partial\sigma_{rr}}{\partial r}+\frac{1}{r}(\sigma_{rr}-\sigma_{\theta\theta})=0 \tag{2.56}$$

By replacing the expression of σ_{rr} and $\sigma_{\theta\theta}$ in the equilibrium equation, this becomes just a function of the radius of the system, so we can write the ordinary differential equation that represents the problem:

$$\frac{d^2u_r}{dr^2}+\frac{1}{r}\frac{du_r}{dr}-\frac{u_r}{r^2}=0 \tag{2.57}$$

For this case, the general solution u_r is given by:

$$u_r(r)=Ar+\frac{B}{r} \tag{2.58}$$

being A and B constants to be identified from the boundary conditions of the problem.

The solution $Ar+\frac{B}{r}$ found so far describes the radial displacement for a given homogeneous system subjected to a temperature variation. As shown, the author's development of this analytical model aims to assess the interaction between the inclusion and the surrounding matrix. Thus, it is necessary to express the constants A_i, B_i (inclusion), A_m and B_m (matrix). So, the problem can be state as:

$$u_r(r)=\begin{cases}A_i r & \text{if } r\in\Omega_i\equiv[0,r_i]\\ A_m r+\dfrac{B_m}{r} & \text{if } r\in\Omega_m\equiv[r_i,\infty)\end{cases} \tag{2.59}$$

and presents the behavior shown in Figure 2.18.

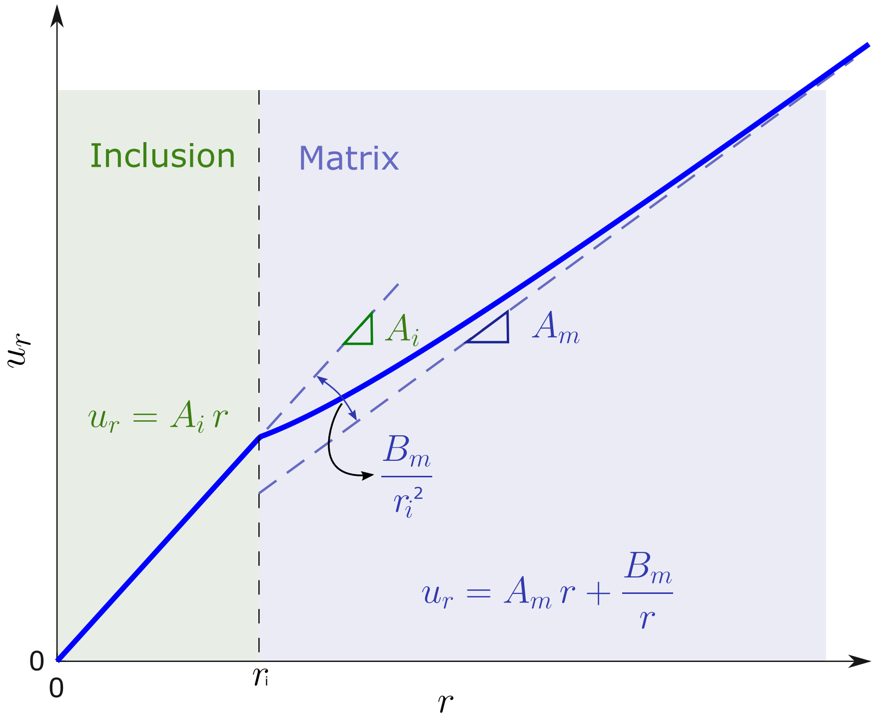

Figure 2.18: Interpretation of the model parameters. The radial displacement in the MCS is governed by the A_i parameter, into the inclusion, while A_m and B_m in the matrix [65].

A physical interpretation of the model parameters on the radial displacement can be seen in Figure 2.18. The solution has three parameters. Inside the inclusion domain, the solution is linear and its slope is given by the parameter A_i. When distant from the inclusion, the slope is governed by the parameter A_m, which corresponds only to the thermal expansion of the matrix. The transition region, close to the inclusion, is governed by the parameter B_m and decays in magnitude with $1/r$ factor. Since B_m can be written in terms of A_i, A_m and r_i, the extension of the transition region depends on the inclusion radius.

Since the developed equation is two-dimensional, to identify the constants A and B one must adopt the hypothesis of plane stress state or plane strain state. Here, the plane stress solution will be presented, for this is more representative of the experimental problem that the author will approach.

2.3.5 Plane stress state: inclusion surrounded by an infinite matrix

In the case of the plane stress state, the stresses in the z direction are null, while the strain concerning the z direction is non-zero. The expression for the normal stress in the z direction is given by:

$$\sigma_{zz} = (\lambda + 2\mu)\left(\varepsilon_{zz} - \alpha\Delta T\right) + \lambda\left(\varepsilon_{rr} - \alpha\Delta T + \varepsilon_{\theta\theta} - \alpha\Delta T\right) = 0 \tag{2.60}$$

Thus, for the stress normal to the plane to be zero, the normal strain with respect to the z direction is written as:

$$\varepsilon_{zz} = \frac{2\lambda\left(\alpha\Delta T - A\right)}{(\lambda + 2\mu)} + \alpha\Delta T \tag{2.61}$$

and therefore the radial stress equation (σ_{rr}) can be described as:

$$\sigma_{rr} = (\lambda + 2\mu)\left(A - \frac{B}{r^2} - \alpha\Delta T\right) + \lambda\left(A + \frac{B}{r^2} - \alpha\Delta T + \frac{2\lambda\left(\alpha\Delta T - A\right)}{(\lambda + 2\mu)}\right) \tag{2.62}$$

Since for $u_r(r = 0) = 0$, in order to mathematically satisfy the problem, B_i must equal 0, thus again making the offset in the inclusion domain exclusively a function of A_i. Considering that the matrix surrounding the inclusion is infinite, we have that $\lim_{r\to\infty}\sigma_{rr}(r) = 0$.

$$2(A_m - \alpha_M\Delta T)\left(\mu_M + \lambda_M - \frac{\lambda_M^2}{(\lambda_M + 2\mu_M)}\right) = 0 \tag{2.63}$$

Thus, $A_m = \alpha_M\,\Delta T$.

From the boundary conditions of the problem, the displacement and radial stress fields are continuous in the inclusion/matrix interface. Thus:

$$A_i - \frac{B_m}{ri^2} - \alpha_M\Delta T = 0 \tag{2.64}$$

$$(A_i - \alpha_I\Delta T)\left(\mu_I + \lambda_I - \frac{\lambda_I^2}{(\lambda_I + 2\mu_I)}\right) - \frac{B_m\mu_M}{ri^2} = 0 \tag{2.65}$$

Isolating $\frac{B_m}{ri^2}$ in Equation 2.64 and substituting its value in Equation 2.65 we obtain:

$$A_i = \frac{\alpha_I\left(\mu_I + \lambda_I - \dfrac{\lambda_I^2}{\lambda_I + 2\mu_I}\right)\Delta T + \alpha_M\mu_M\Delta T}{\mu_I + \lambda_I - \dfrac{\lambda_I^2}{\lambda_I + 2\mu_I} + \mu_M} \tag{2.66}$$

Replacing the value of A_i in Equation 2.64 we obtain:

$$B_m = \left(\frac{\alpha_I \left(\mu_I + \lambda_I - \dfrac{\lambda_I^2}{\lambda_I + 2\mu_I} \right) \Delta T + \alpha_M \mu_M \Delta T}{\mu_I + \lambda_I - \dfrac{\lambda_I^2}{\lambda_I + 2\mu_I} + \mu_M} - \alpha_M \Delta T \right) r_i^2 \tag{2.67}$$

The inclusion's parcel of the parameters' description can be simplified by a single elastic parameter using the relation $Z_I = \lambda_I + \mu_I - \dfrac{\lambda_I^2}{\lambda_I + 2\mu_I}$, and then, the parameters' relation are given as:

$$A_i = \frac{(Z_I \, \alpha_I + \mu_M \, \alpha_M) \, \Delta T}{Z_I + \mu_M} \tag{2.68}$$

$$A_m = \alpha_M \, \Delta T \tag{2.69}$$

$$B_m = \left[\frac{Z_I \, (\alpha_I - \alpha_M) \, \Delta T}{Zi + \mu_M} \right] r_i^2 \tag{2.70}$$

With the determination of the constants A_i, A_m, B_i, and B_m, we have the displacement field determined for this particular case. Consequently, it is possible to determine the strain and stress fields of interest in knowing the phases' material properties.In the model, the highest values of stress will occur in the interface. Therefore, it is also in this region that crack nucleation would be expected. The interfacial radial ($\sigma_{rr}(r_i)$) and tangential ($\sigma_{\theta\theta}(r_i)$) stresses for the matrix domain can be calculated as:

$$\sigma_{\theta\theta}(r_i) = -\sigma_{rr}(r_i) = \frac{2 \, Z_I \, \mu_M (\alpha_I - \alpha_M) \Delta T}{Z_I + \mu_M} \tag{2.71}$$

2.3.6 Crack patterns in composite systems due to temperature variation

In a biphasic composite with phases' different values of CTE, by the relation between the CTE of the phases and the positive or negative value of a temperature variation, two types of crack patterns may occur, assuming that only the matrix could fracture. If $(\alpha_I - \alpha_M)\Delta T > 0$, then the cracks will be radial, beginning at the interface. In the other situation, for $(\alpha_I - \alpha_M)\Delta T < 0$, the material will present circumferential cracks. Figure 2.19 illustrate these patterns.

A critical aspect is the stress behavior in each material phase. This knowledge

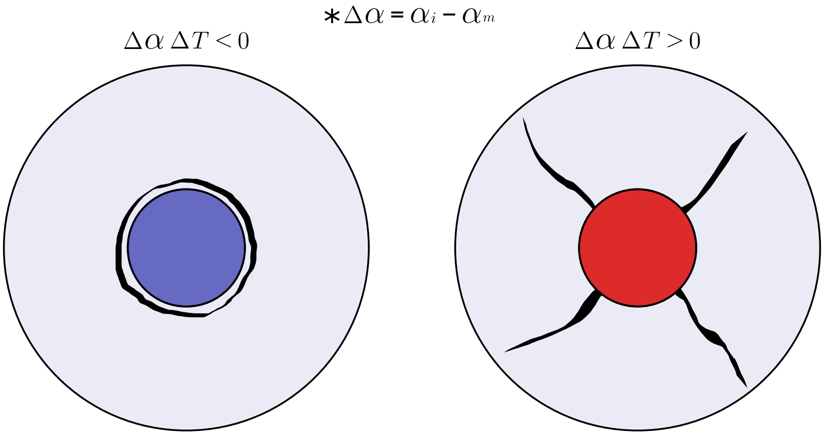

Figure 2.19: Representation of the usual crack patterns for a low volume fraction composite with a spherical inclusion, resultant of a temperature variation [65].

leads to the understanding of why certain types of cracks may occur in each domain, depending on how is the stress distribution on each domain. In the inclusion domain, the stresses are constant, and all the stresses have the same sign. In the matrix domain, the radial stress has the same value as the radial stress of the inclusion in the interface and decreases in magnitude as the material point observed is further away from the interface. The tangential stress in the matrix domain has the opposite sign of the inclusion's tangential stress in the interface and decreases in magnitude as the material point observed is further away from the interface.

These crack patterns were seen experimentally by Davidge & Green [17] where cracks resultant of the cooling process of model composites made of spherical thoria inclusions embedded in different glass's matrix were observed. However, for composites with high volume fractions, the circumferential and radial crack may coexist and interact due to the higher strain field interaction of each inclusion in the other ones, as can be seen in Figure 2.20.

To observe the effects of CTE mismatch cracks in composite materials, Tessier-Doyen [18] experimentally evaluated the variation of Young's modulus of three model composites, produced for a hot pressing process, composed of glasses matrix (G1, G2, and G3) with alumina semi-spherical inclusions via an ultrasonic waves propagation technique using contact transducers. For each material system, three volume fractions (ϕ) samples were manufactured with $\phi = 15\%, \phi =$

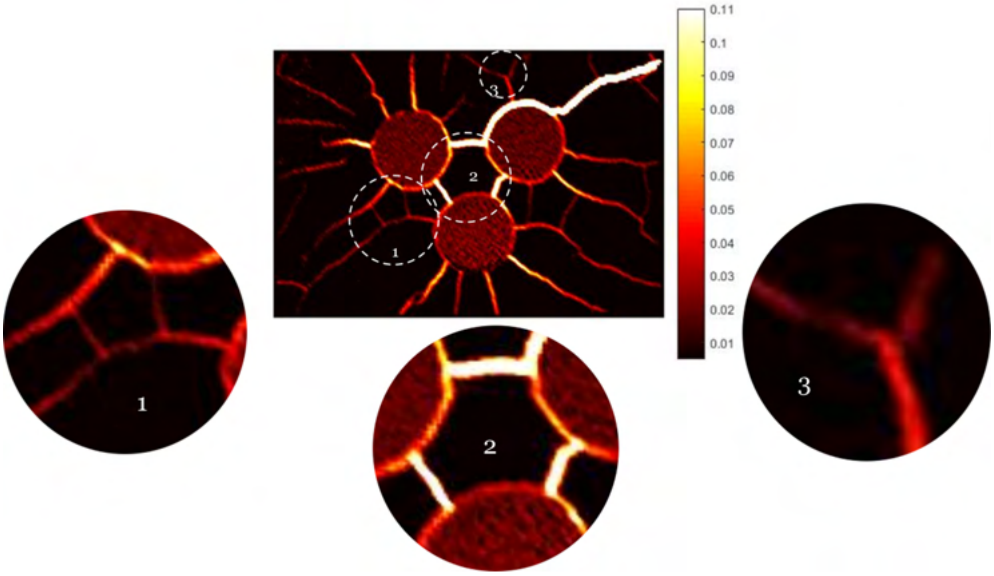

Figure 2.20: Crack patterns analyzed by the maximum principal strain via DIC for a temperature variation of a high volume fraction model composite of aluminium cylindrical inclusions in an alumina slurry matrix. Some highlights are given for complex crack phenomena been that radial and circumferential cracks can be seen in the results [65, 66].

$30\%, \phi = 45\%$ and all the samples were submitted to a temperature variation cycle. Therefore, their experimental results evaluate the effects of the $\Delta\alpha$ and of the volume fraction in the composites' effective Young's modulus regarding a temperature cycle, as can be seen in Figure 2.21. Note, that, for these results $\Delta\alpha = \alpha_M - \alpha_I$.

The top graph shows the result for a model composite with a quite low CTE mismatch between the phases, which leads Young's modulus to follow the same path during heat and cooling. The bottom left graph shows model composites with a negative $\Delta\alpha$, that produced circumferential cracks during the cooling of the hot pressing manufacture process, then, during the new heating of the samples for the measuring of E, initially, E increases due to a healing process by the closure of the existent cracks followed by a decrease in reason of the glass softening mechanism in competition with the healing process. In the cooling of this model composites, initially, the interface between the phases was better consolidated and maintained a higher E, but then new circumferential cracks appear, and the E value drops. The bottom right graph shows model composites with a positive $\Delta\alpha$, which shows similar results with the previous example, however, involving radial cracks and a more fierce competition between the phenomenon of healing and softening. The graphs also present the behavior of the glasses without inclusions [18].

$*\Delta\alpha = \alpha_m - \alpha_i$

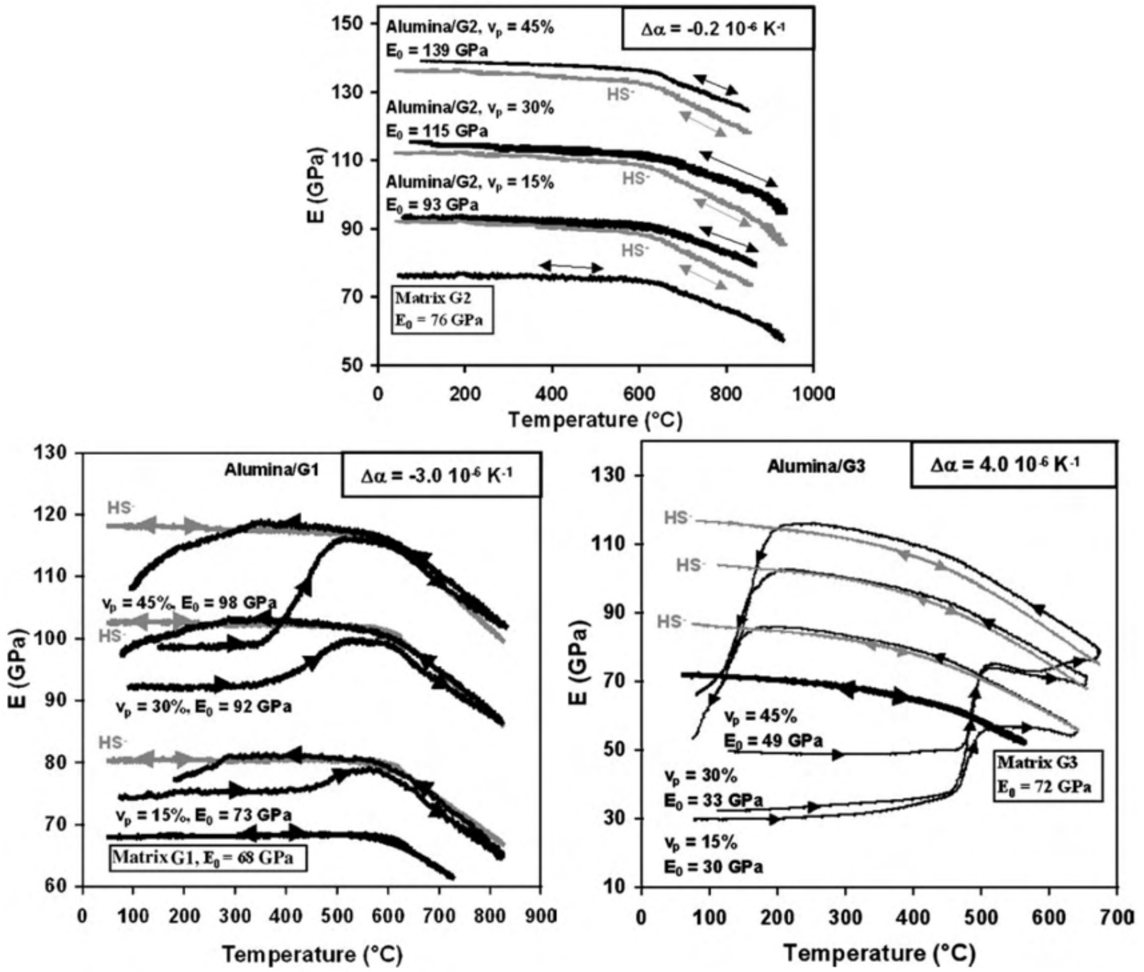

Figure 2.21: Evaluation of Young's modulus of three model composites in three volume fractions during temperature variation cycles via ultrasonic wave propagation. The black lines present the experimental results, while the gray ones present Hashin and Shtrikman's lower bound analytical model prediction for comparative [18].

Concerning the volume fraction, the results show that the higher the volume fractions, the higher the hysteresis of the curves presented. For lower values of CTE mismatch, the damage and healing effects are not visible for the temperature variation applied.

2.4 Digital Image processing

The core computational tool for the analyses of the experimental procedures executed in this research is the Digital Image Correlation (DIC). The use of DIC enhances the amount of data obtained of an experiment, and allows experimental execution inconsistencies to be identified and sometimes corrected numerically [67]. In this section, concepts about digital image processing that can help to understand the DIC technique and other post-processing tools used in the methodology and results of this thesis are presented.

The digital image processing field had developed based on the visual perception and interpretation of people, and evolved with the improvement of computational processing of two and three-dimensional data [68]. This science deals with two different perceptions – the human's and machine's – of a same object, the digital image. The digital image processing is an interdisciplinary field, once its basis comes from physics, mathematics and computer science, and its applications embraces exact, biological and even human sciences [69]. From the tinniest to the hugest things, its visual interpretation. In other words, the way human vision works exerts a great influence on the way in which technology to acquire, display and analyze images were developed. However, the acquisition of images has extended beyond what is sensitive to human eyes, expanding to all types of signals that can be captured, such as infrared images, ultraviolet radiation, acoustic signals, etc [70].

In the present thesis, the processing of digital images was used to extract data of materials properties, mechanical behavior, and damage evolution from tested specimens. For the sake of simplicity, from now on it will be considered a digital image as the one that can be obtained from a digital camera device, a photography.

2.4.1 Basic concepts of digital images

A Digital image is the result of light intensity acquire by each sensor element of a digital camera. Each one of these elements will provide a value for one pixel of the total image, being the pixel the smallest dimensional element of an image. From this explanation it is possible to define two important properties of an image, the resolution and the dynamic range.

A digital camera is a digital-analogical converter that allows the spatial and intensity discrete quantization of what in reality is a continuous thing. The resolution of an image refers to its spatial discretization, the total number of pixels that composes an image, and the dynamic range is the light intensity discretization, the range of values that each pixel of an image can assume. The resolution of an image is commonly set in terms of megapixels, and the dynamic range is set in terms of bits. Figure 2.22 shows an example of different resolutions of an image.

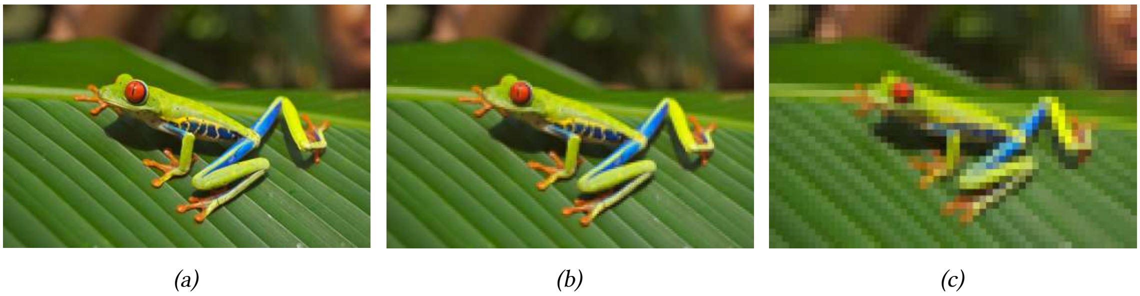

Figure 2.22: Different image resolution: (a) 1998 by 3024 pixels; (b) 111 by 168 pixels; (c) 37 by 56 pixels. Source image obtained from [71].

The bit, is the exponent of 2 that gives the number of information that a pixel may represent, if an image is said to have 8 bits – which is equal to 1 byte – it means that each pixel can assume 2^8 or 256 values of luminosity intensity. The number of bits of an image is also called the bit depth. Therefore, in a gray scale 8 bit image, the value 0 will represent the color black and the 255 value represents the color white. When talking about colored images, most of them are composed of three layers of color intensities that when added together gives the hue of each pixel. Figure 2.24 presents the three layer intensities of an image that when combined results in the colored image. Summarizing, it can be said that an image is a spatial function (f(x,y)) of intensity values. Assuming an RGB (Red, Green, Blue) image, this function can be written according to Equation 2.72.

$$f(x,y) = f_R(x,y) + f_G(x,y) + f_B(x,y) \tag{2.72}$$

Image data storage can be a little tricky. To properly understand the computer memory system, one must understand that when data processing and storage grew, the concept of Byte was introduced as being a combination of 8 bits. Also, that a kbyte $\approx$ 1024 bytes and a Mbyte $\approx$ 1024 kbytes.

With these concepts established, they can be used to explain the memory size needed to store an image in the hard drive or to store it in a buffer memory to display it. The image file size is computed as Size = Resolution × bit depth × number of image layers [bits] or Resolution × bit depth × number of image layers/8 [bytes] or Resolution × bit depth × number of image layers/8× 1024 [kbytes], and so on. Therefore, using as an example 8 bits RGB image with a resolution of 1024x1024 pixels, its size would be 1024 × 1024 × 3 × 8/(8 × 1024 × 1024) = 3 Mb.

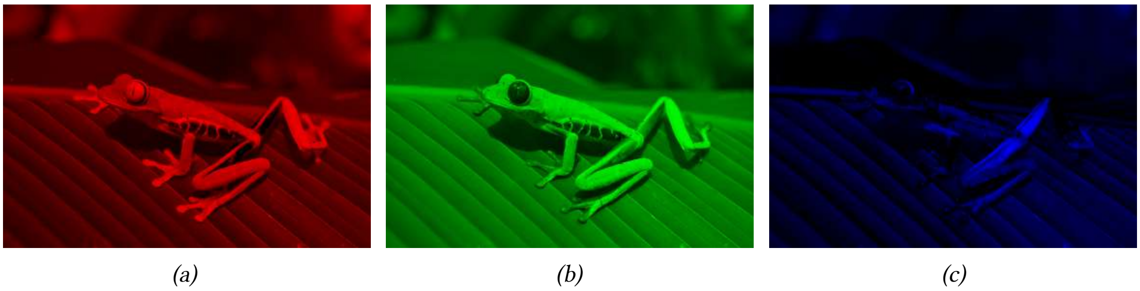
(a) (b) (c)

Figure 2.23: RGB image composition: (a) red layer; (b) green layer; (c) blue layer. Source image obtained from [71].

Another interesting image characteristic that can be used to evaluate digital images, in relation to digital image processing, is its histogram. The histogram of an image presents the pixel intensity value repetition in an image. This tool can be used to access if some values are a lot higher than others, if there is a regular distribution of intensities, if all the dynamic range possible is in use, among other applications.

Regarding the spatial intensity distribution of an image, concepts of contrast, sharpness, and blur can also be presented. The contrast relates the difference in light intensity between a pixel and its neighbors. If two regions of pixels have a high difference in light intensity, this image region has a high contrast, or it is said that this region is sharp. The act of apply sharpness to an image will result in clear borders and less smooth color transitions. In the other hand, If two regions of pixels have a low difference in light intensity the view of this image has a low contrast, or it is said that this region is blurred. The act of apply blur to an image will result in unclear borders and smooth color transitions.

A simple way to vary the contrast of an image is to modify its dynamic range.

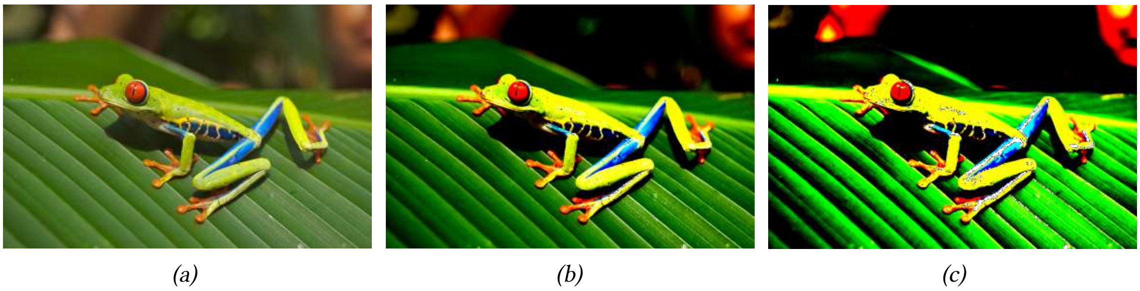

(a) (b) (c)

Figure 2.24: Gradual increase in contrast by narrowing the limits of dynamic range: (a) original image; (b) contrast increased by 60% compared to the original image; (c) contrast increased by 90% compared to the original image. Source image obtained from [71].

The larger the dynamic range, the smoother will be the color transition, the narrow the dynamic range, the sharper the color transition. When this narrowness come to its absolute, the transition value is denoted a threshold. A value of threshold makes that every value equal or above the threshold will assume the maximum value of light intensity, and every value below the threshold will assume the minimum value of light intensity, creating a binary result.

Another technique to modify the contrast and/or remove noise is the convolution. The appliance of a convolution consists in the creation of a pixel matrix that will modify each pixel value according to its intensity and the intensity values of its neighbors contained in the convolution pixel matrix. To the application of this and other techniques, it is usual or even needed the definition of a Region Of Interest (ROI). The ROI delimits where the digital image processing will be executed, and it is defined to process a specific region of pixels or to avoid the image borders, that cannot be correctly processed for example by a simple convolution.

Explained the basics about images properties and basic processing techniques, now, a small revision of field measurement techniques is presented. The idea is to show some possibilities to experimentally obtain field measurements and to explain why the DIC technique was chosen over others.

2.4.2 Field measurement with digital image processing

One of the many uses of digital image processing is in techniques to obtain field measurements using image comparison or special techniques to observe intensity variation in an image during a test. These techniques of field measurements can be used by a straight comparison pixel to pixel, using pixel clusters or with the aid of numerical region's discretization using a mesh, for example. Some techniques will be presented to show the existent possibilities, and it will be discussed why the decision by the DIC technique for this work.

Digital Photoelasticity: One of the oldest methods to evaluate strains in solids via image processing is the Photoelasticity technique. This technique is based on the change in the birefringence properties that some material presents when deformed. Figure 2.25 shows the effect of birefringence. It is applicable with the use of a polariscope in such materials that exhibits birefringence and are considered photoelastic. Over the time, the Photoelasticity evolved from a technique used to understand qualitatively the stress-strain state of materials to more quantitative and refined technique using robust software to process color fields.

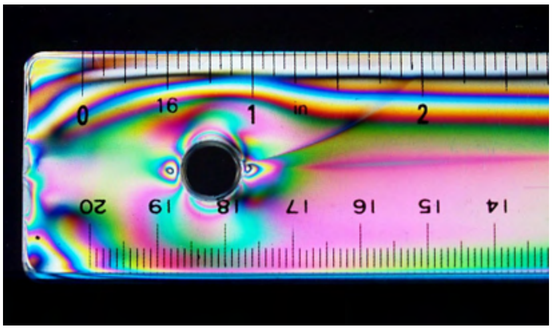

Figure 2.25: Stress Induced Birefringence: Polarized light over a polyvinyl chloride ruler photographed using an analyzing polarizer in front of camera lens. Image credit: Cran Cowan.

The great difference of this technique is that it physically displays colors that are used directly in the estimation of the stress-state with Digital Photoelasticity. The technique presents visually impressive results, however the intrinsic optical condition of the technique also limits the stress-strain discretization that it is capable to produce. Further, the restricted range of materials in which the technique is applicable lead it to be more used in the investigation of complex structure or scenarios using photoelastic materials than to actually characterize or test different material.

Despite its limitations, Digital Photoelasticity is still used in many biomedical studies and applications due to the range of organic tissues where photoelasticity is applicable (Figure 2.26 (a)). The technique is also quite impressive to deal with problems such as the identification of the crack tip in fracture tests (Figure 2.26 (b)). Furthermore, it is a simple and effective way to demonstrate to students solid mechanics concepts with experimental visual references [72].

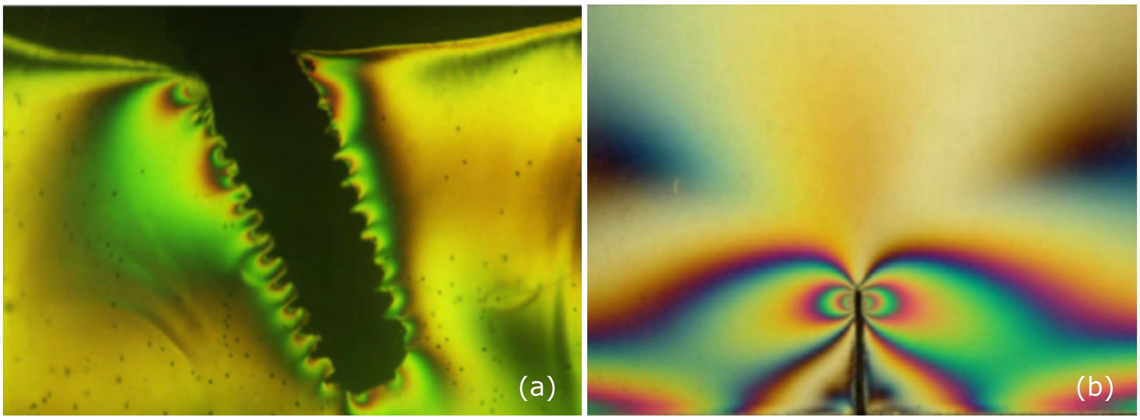

Figure 2.26: Application examples of Photoelasticity: (a) Dark field isochromatic for a load of 237N in implant at molar region [73]; (b) Experimental isochromatic image near the crack tip in an edge cracked specimen on hot plate [74].

Interferometry based techniques:

Many field measurement techniques are based on signal interference to evaluate displacement and strain – *e.g.,* Moiré interferometry, Electronic speckle pattern interferometry and Shearography. The main idea is to obtain the interference measure of a surface or focal point using a laser, a beam splitter or a similar system, some lens, and mirrors. The laser is split, and the mirrors changes the recombined beam frequency, creating an out of phase signal that is acquired with a sensor or camera. Figure 2.27 display a Shearography system. Images of the surface of different solicitations are then correlated, which results in a fringe pattern. This fringes contains information in regard to the displacement derivative in the surface, which can be measured with the reconstruction of the phase distribution [75].

Rather than the Digital Photoelasticity, these techniques are applicable to a great range of materials and can be used to attain deeper insights in regard to the mechanical behavior of materials. These techniques are specially efficient to measure small surfaces, although they can use lens systems to cover larger ones, and are specially sensible to out-of-plane displacements. Also, some interferometry based techniques can be used to measure three-dimensional displacement

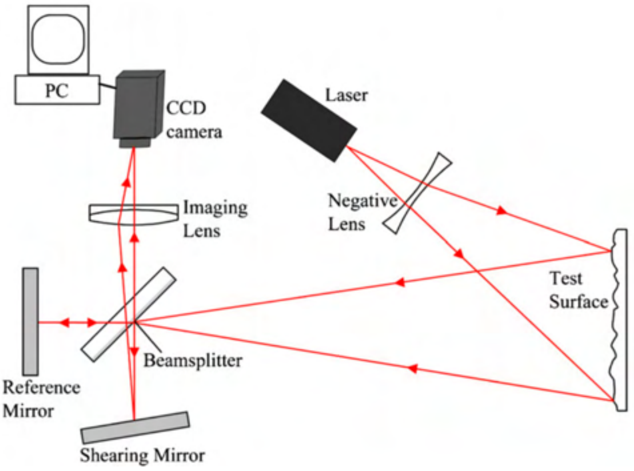

Figure 2.27: A shearography system based on a Michelson shearing interferometer [75].

as the Fringe projection and the Digital holography techniques. However, it is important to know that the implementation of them are often costly in comparison to other methodologies.

2.4.3 Digital image correlation (DIC)

The DIC is a field measurement technique to obtain the displacement fields of two or three-dimensional data in the surface or interior of a body [43, 44, 76, 77]. It is based on the continuity of the optical flux. For a 2D case, as used in this thesis, an image is defined as a bi-dimensional distribution of light intensities. For DIC, the analyzed surface is usually painted with white and black spray ink, creating a texture to improve the gradient and create a random speckle over the surface. Therefore, two images of the same body can be compared considering these intensities positions, assuming that no external factor changed the intensities values acquired by the camera or that the appropriate actions experimentally and/or numerically had been taken to correct these changes. Of course, even with all the care, it will always exist a noise of acquisition that will be further explained ahead. Let us define an image of the reference configuration as f and another in a deformed condition as g. The displacement field $\mathbf{u}(\mathbf{x})$ is obtained as the value that minimizes the gray level residual (ϱ^2):

$$\varrho^2 = \sum_{ROI} [g(\mathbf{x}) - f(\mathbf{x} + \mathbf{u}(\mathbf{x}))]^2 \tag{2.73}$$

where $\mathbf{x}$ represents the pixel position vector and ROI the region of interest. The image residual (ρ) can be defined as $\rho = g(\mathbf{x}) - f(\mathbf{x} + \mathbf{u}(\mathbf{x}))$, and in this image, it is possible to see the kinematics that diverges from the main behavior of the body being tested, illumination changes, discontinuities and new light intensities values in the image, and also acquisition noise. The noise of acquisition can be evaluated as the mean residual of the correlation of several reference images, i.e. images that present the specimen of an experiment prior to the appliance of any load.

DIC can be implemented via two different approaches, known as local and global. The local DIC operates analyzing independent regions among images and trying to find a displacement for each region that correlates then. Since no continuity is enforced, it can lead to convergence issues especially for analyzing localized phenomena like cracks. The global DIC, borrows the concepts from the Finite Element methodology, using a finite element mesh over all the domain of interest and correlates two images not as independent regions, but obtaining the displacement based on shape-functions, being the continuity of the displacement field imposed in the minimization procedure.

Therefore, in a more straightforward explanation, the field displacements obtained by the DIC are the displacement of the nodes in order to pursue the light intensity values of the reference image in a deformed one for each element in the mesh. The Figure 2.28 presents a simplified representation of the DIC process.

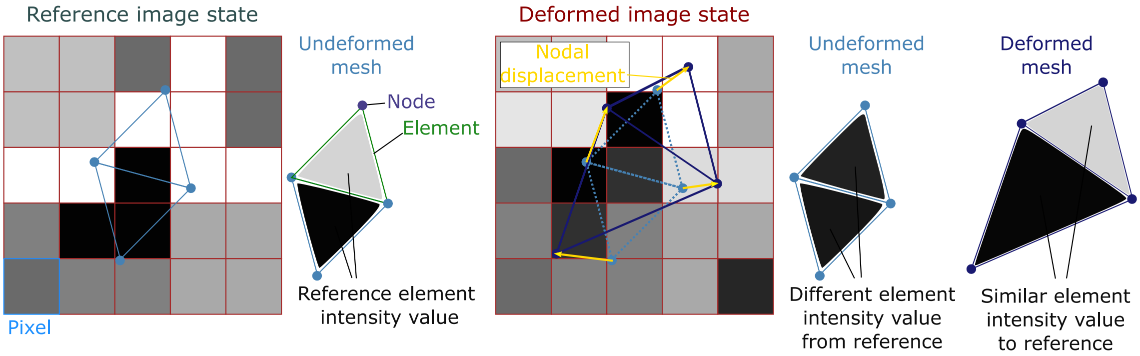

Figure 2.28: Representation of the digital image correlation algorithm obtaining of displacement field.

It is worth mentioning that, as images are a discretization of a continuous 2D signal, in the observation of a pixel region of two images in different configurations, a viewer will not see a simple pixel translation. Each pixel already represents a discrete interpolation of a continuous signal, and the displacements in the real world do not operate on discrete pixel size. Therefore, as demonstrated in Figure 2.28, a deformed image will not contain the same pixel values as the reference image, but the overall intensity of a region is expected to be preserved, apart from acquisition noise, allowing to find the best configuration for the element with a minimized residual.

Once a test assisted by DIC is conducted and a DIC analysis performed, the results will present the displacement field in the sample medium shown by the ROI. From the displacement fields, strain fields can be obtained. With these results, material properties can be evaluated numerically based on the minimization of analytical models [42, 67, 78]. It is also possible to identify other interesting phenomena in the experiments as crack nucleation, propagation, bifurcation, and coalescence [53, 54, 64, 66]. Such phenomena can be parameterized with the materials properties to obtain fracture parameters or models [79, 80].

There are also similar DIC techniques apart from the traditional application (2D using a single camera), like the stereo correlation (two or more cameras to obtain out-of-plane displacements), the Digital Volume Correlation (DVC, *e.g.,* using volumes from a tomograph), the integrated DIC (with analytical solutions used as displacement shape functions), among others [42–44, 77, 81, 82]. When discussing the most traditional use of the technique, it is interesting to notice that the material resources needed for its application is basically a camera. Several technical aspects of a camera can improve the chances of a good correlation, despite that, any camera can be used to perform a digital image correlation, which makes the technique pretty accessible to be implemented.

The technique can be used not only to analyze tests, but also to Control tests if DIC is performed live, to couple experimental information obtained using DIC with numerical simulations, calibrate material models, validate numerical tools, among other applications.

Once the technique operates on the comparison of images, an interesting insight is that it can be used in different scales. The technique can correlate images obtained by a microscope and also images of large structures, as long as the basic principles of the conservation of the optical flux has been respected in the image acquisition process.

All the DIC analyzes herein were performed in the Correli 3.0 framework [83] to measure full-field displacement and strain fields. The displacement field is discretized in 3-noded triangular finite elements shape functions $\boldsymbol{\Psi}$, *i.e.* $\mathbf{u}(\mathbf{x}) = \sum_j^N \upsilon_j \, \boldsymbol{\Psi}_j(\mathbf{x})$, with j being the degree of freedom indexation and N the number of degrees of freedom. Therefore, the nodal displacements υ_j are the degrees of freedom used in the minimization of Equation (2.73), and then, displacements in the elements are linearly interpolated. From the displacement fields, the same framework also have tools to calculate the strain fields, which are shown and explored hereafter.

2.4.4 On the benefits of using DIC for mechanical tests with temperature variation

When performing regular mechanical tests to evaluate material properties, several aspects can deceive the obtaining of trustworthy results – *e.g.,* non-parallel opposite faces of the specimen or of the test equipment, defects on the specimen causing stress concentration, crushing of porous media, etc. [67, 84]. When trying to evaluate temperature-dependent mechanical properties, these problems must be addressed once again.

The temperature-dependent Young's modulus evaluation of a ceramic using an uniaxial compression test or a three point bending test might deceive, if conducted without the proper care to the thermal expansion of the specimen and test machine parts. The Poisson's ratio evaluation in such conditions must also consider the thermal strain of the system. This is one of the arguments adopted to defend the use of dynamic tests such as the Impulse Excitation Technique (IET)[84].

One of the great advantages of tests assisted by DIC is the obtaining of full-field data, that many times, allows observing these influences and to take they into account when evaluating material's mechanical properties [67]. This way, the negative effects of static tests evaluations can be addressed, once more data is available to work with.

2.4.5 On the effects of out-of-plane displacement on image based in-plane measurements - A two camera solution

When using 2D measurement techniques to evaluate in-plane displacements, hypothesis are assumed, considering that there are no out-of-plane displacements. If that is not the case, measurement techniques that capture the parasite effects of out-of-plane motion in the in-plane measurements must be adopted or equipment that reduces these out-of-plane effects can be employed.

The problem of evaluating the influence of out-of-plane displacement on in-plane measurements has been addressed in the literature [82], and as said, there are sophisticated solutions to deal with this problem. Some of these solutions employed relies on the use of stereo vision measure techniques and 3D measure techniques [85, 86]. In the present thesis, a simpler and yet efficient strategy was adopted when such a problem had to be dealt with. Based on Sutton's equations describing the parasite effects of out-of-plane motion, a two camera set up facing opposite faces of a tested specimen can be used to compensate most of these effects by using the average displacement results of the cameras.

To use this strategy, some experimental considerations must be satisfied. The two cameras should be of the same model and be equipped with the same lens, also, the cameras must be equally distant from the specimen. If these criteria were not respected, further considerations would need to be added to employ a similar idea. In the experiments that will be presented in here, the considerations described were respected.

This two camera strategy can compensate out-of-plane translations and rotations of the specimen, however, it cannot avoid out-of-plane expansion, but in many situations this expansion is negligible. In Figure 2.29 an example of a specimen translation – of real in-plane dimensions X and Y – is represented along with the equations describing the effects on dimensions, displacements and strains in the virtual specimen perceived on images of two cameras observing the translation from opposite sides. The equations presented in Figure 2.29 presents how a translation ΔZ changes the virtual dimensions (X_s, Y_s), resulting in a horizontal (U_s) and vertical (V_s) displacement with their corresponding strain $(\varepsilon_{sxx}, \varepsilon_{syy})$, where the indices 1 and 2 are to specify the camera. L represents the original distance between each camera lens and the perceived specimen, while L_{sl} is the distance between the camera sensor and the lens. In this example, the images attained for cameras 1 and 2 will present an equal intensity distortion, but of reduction for camera 1 and magnification for camera 2. Therefore, if a measurement technique was applied to the images of the cameras, the average results of the cameras' displacement or strain would be equal to zero.

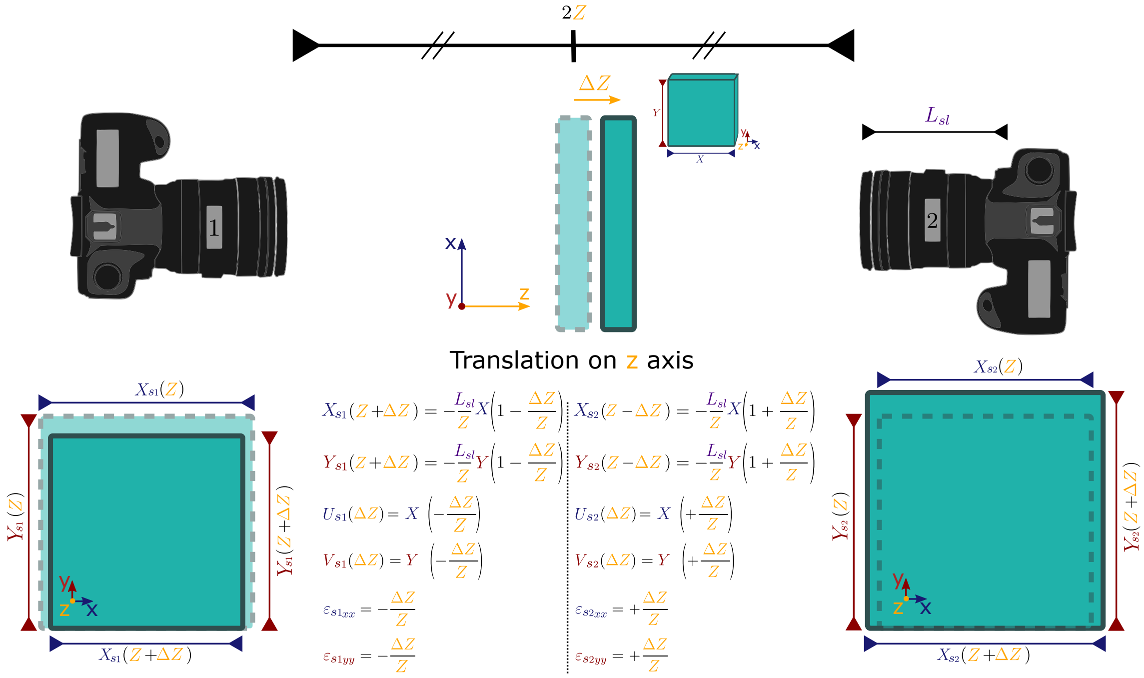

Figure 2.29: Strategy to compensate out-of-plane translation using two cameras on opposite sides of a specimen.

The equations presented also have some simplifications, once they consider that Z is relatively larger than L_{sl} for the calculation. However, if it is not the case, the strategy is still valid, but the distortions of each camera would be higher. For further in-depth of these equations, read reference [82].

2.5 Theoretical framework conclusions

Composite systems have a complex thermomechanical behavior under temperature variations. The main reason for this complexity is due to the CTE mismatch that the phases of the system may present, which can produce different stress-strain states in the material regarding aspects of volume fraction, disperse phase shape and phases properties. Analytical and numerical models can help to understand crack phenomena in such systems, but experimental data is indispensable for calibration and validation of such models. An interesting way to study such systems is with the aid of model composites designed to isolate phenomena of interest, presenting a simpler and more predictable material response. Experiments with model composites can be performed assisted by the DIC technique, producing full-field results that allow to investigate the interaction of the material phases.

3 MATERIALS AND METHODS

This chapter presents the scientific and technological aspects studied and developed to enable the conduction of the present study. The equipment and methodologies developed for conducting the experiments and the designing and process of the model composites studied are presented here.

3.1 Furnaces developed for the study

The results of experiments involving temperature were conducted in furnaces designed and constructed to allow the application of the DIC technique. This section describes the furnaces' main capacities and differences. The furnaces are designated by the letter "F" and their maximum operational temperature.

The first furnace developed was the F600. The furnace is a cubic chamber with a 400 mm edge internally. It has three borosilicate windows on the top cover that enable the image acquisition and illumination of the specimen inside. The specimen positioning faces the cover and aligns with the main window. The heater elements are finned resistors positioned at the bottom of the furnace. The F600 was the first in which the thermal experiments of dilatometry and temperature variation of model composites were performed. There was no dedicated temperature acquisition system in the experiments conducted in this furnace. Thus, the temperatures of each image acquired were registered manually according to the controller temperature display. The setup for the experiments conducted in the F600 can be seen at the top of Figure 3.1. This oven was developed in the Department of Aeronautical Engineering at EESC-USP.

The second furnace is the F900. It allows the observation and illumination of both sides of a specimen through six windows, as shown at the bottom of Figure 3.1. All the images acquired for the present discussion were gathered through the bigger windows, while 800 lumens LED blue lights were set on the others. The F900 is also equipped with two vertical zones with two separate control systems, aiming to mitigate vertical temperature gradients, and K thermocouples. All the setup is made to have the cameras, furnace windows, and samples well aligned. A temperature acquisition system was used to register the temperature of the experiments conducted in the F900. This oven was developed in the Department of Material Science Engineering at UFSCar.

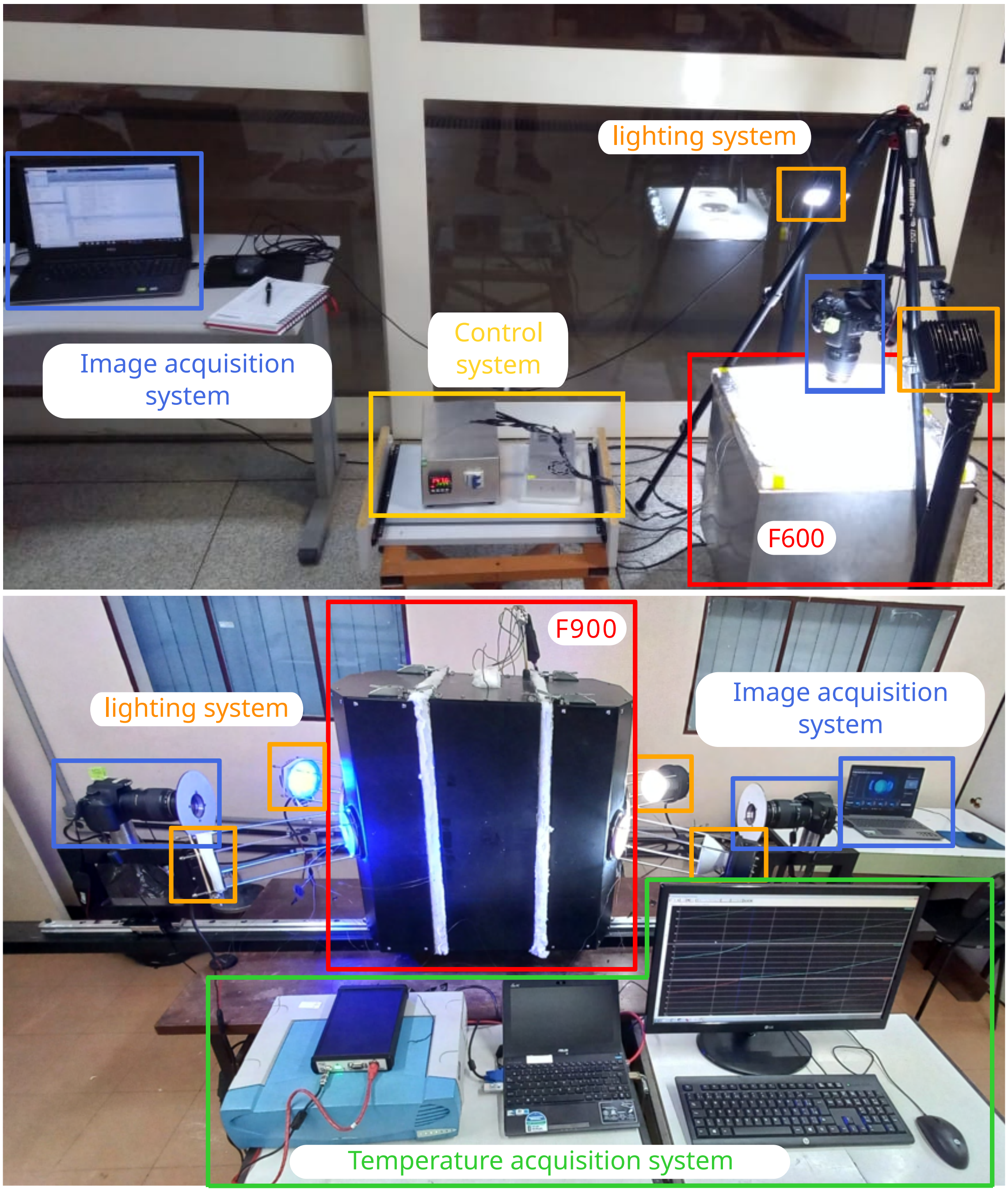

Figure 3.1: Experimental set for temperature variation experiments conducted in the F600 and F900.

The F900 was designed to be coupled to a universal testing machine (UTM) MTS Exceed E44.304 (30 kN capacity), allowing the conduction of mechanical tests – in different temperatures or with temperature variation – acquiring images of the tested specimen. There was a dimension constraint of 400 mm between the columns of the testing machine, represented in the top view of the furnace configuration in Figure 3.2. The furnace's inner cavity width was limited by the required refractory wall thickness to insulate the testing machine columns and avoid overheating. The overall internal cavity dimensions are 280 mm in height, 170 mm in width and 210 mm in depth to position specimens and loading devices. Two sliding doors close the furnace, each equipped with three transparent inspection windows, a bigger one in the center and two smaller ones at 30° angle from the former. Their respective viewports are 110 mm and 50 mm in diameter. The windows comprise two layers of quartz glass, spaced by an alumina tube (50 mm in length) for insulation purposes. It is important to note that this multi-window setup can be used in different lighting and image capture configurations, making it possible to apply stereo correlation [87]. All the images acquired for the present discussion were gathered through the bigger windows, while blue LEDs were positioned on the other ones.

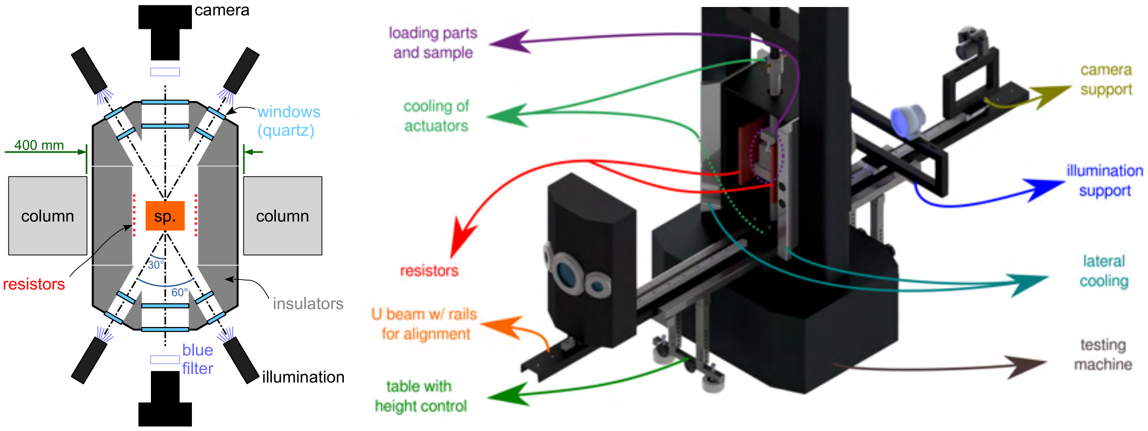

Figure 3.2: Top view and 3D assembly of the developed F900 setup to perform thermo-mechanical experiments up to 900 ℃ [88].

The furnace project was designed using Inventor™ CAD software. The main features are highlighted in Figure 3.2. Two controllers are used to have two temperature-controlled zones (operating independently) along the vertical direction. This design choice tends to decrease the vertical gradient of the temperature field. Two or more thermocouples and an independent acquisition system are used to record the temperature of the experiments conducted in the F900 furnace. Another design requirement was the mounting and dismounting from the testing machine, since it is possible to carry out experiments without controlled mechanical loading (*e.g.,* , dilatometry or creep tests with dead load). In order to perform such tests, a U-beam with rails is used for easier alignment of the cameras, furnace windows, and samples.

3.2 Solutions for conducting experiments in high temperature with DIC analysis

There are several challenges to deal with when conducting experiments in high temperatures. With the performing of DIC-assisted experiments, these challenges become even greater when considering the implications that elevated temperatures and temperature variation can input into the acquisition of images. Thermal radiation, heat waves, and the expansion of all parts inside the furnace must be considered to enable such experiments' conduction. Also, it is important that the specimen tested and artificial texture, if used, do not change their color or vanish, in the case of the artificial texture.

Heat waves are one of the most common issues for image acquisition in experiments with temperature variation. This phenomenon results from the heterogeneous temperature inside the furnace or temperature oscillations inside it, which results in refraction phenomena between the tested material and the image acquisition device that creates distortions in the image and can compromise the results of image-based analysis. To reduce this phenomenon or minimize its effects, strategies can be adopted to enhance the furnace homogeneity, independent controlled heating zones. Also, the increase in exposition time in image acquisition helps as well.

Due to radiation emission from the resistors and specimen with the elevation of temperature, several strategies in this work are adopted to diminish the variance of the light intensity and color of the specimens' surface being photographed. One of the measures adopted to improve the experiments was an investigation of the optimal illumination and image layer to perform the experiments and process the images. The main idea is to investigate how to optimize one of the image layers - “red", “green," or “blue" - to obtain the lowest variation in its color intensity over different temperatures.

It was clear that the most affected image layer was the red layer, once it was visually perceptible the increment in red light as higher temperatures are reached. Therefore, this layer was rejected as being the one that would have the highest variation in intensity. From this knowledge, being the blue layer the furthest from the red in terms of wavelength, it was decided to conduct experiments enhancing the blue layer and filtering as much as possible the red light from image acquisition. With this purpose, in the next subsections, the efforts to enhance the image quality acquisition are presented, improving the DIC analysis.

3.2.1 F900 camera lens setup

The cameras used for the experiments were two Canon Eos Rebel T7i. These cameras have a resolution of 50 Megapixels and dynamic range of 14 bits. The cameras were coupled with Canon Macro 100 lens and in many experiments it were also extensor lens (Extensor EF 2x III).

A system was machined in aluminum to couple different lenses over the basic camera lens. Blue filters with a bandwidth between 360 and 580 nm (FGB39S from THORLABS) were used to reduce the influence of black body radiation. Near-IR hot mirrors for camera protection, which reflect waves between 750 and 1200 nm (FM201 from THORLABS), were used for camera protection. Also, Neutral Density (ND) filters (ND-1000 from Rise UK and variable ND2-ND400 from K&F Concept) were used to allow longer exposition time in the image acquisition.

The blue filter blocks the influence of the red band in the image acquisition. This contributes to the optical flux continuity of the images obtained in the experiments, enabling good convergence in the DIC analysis. In Figure 3.3, the working of the FGB39S blue filter can be observed.

The ND filters reduce the intensity of all wavelengths of light from entering the camera, resulting in the need for a longer exposition time to obtain a given image if compared with the exposition time to obtain the same image without the filter. Heat waves during tests are constantly moving and can form and disappear unexpectedly. Therefore, a longer exposition time allows the obtaining of more even fields, while a short exposition time can get time frames where heat waves have

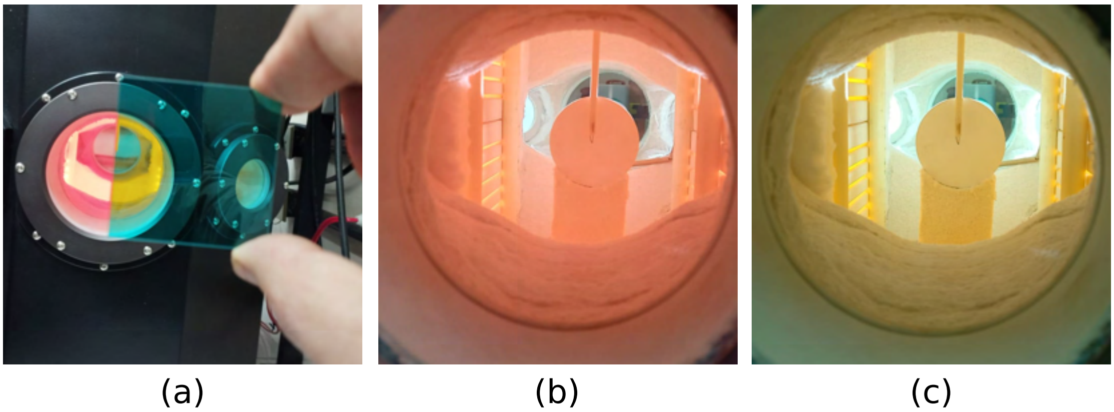

Figure 3.3: Low pass filter effect on the furnace image acquisition at 900°C: (a) Blue filter; (b) furnace interior without the filter; (c) furnace interior with the filter.

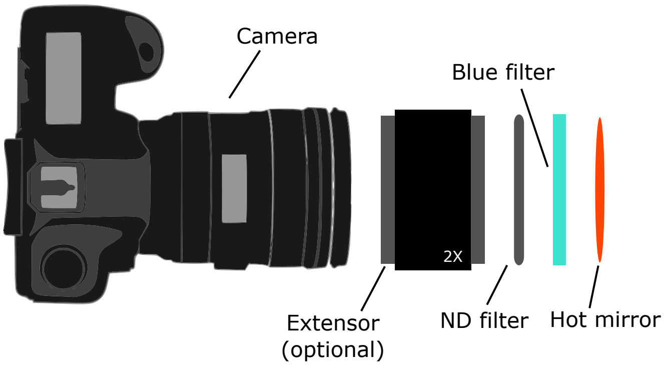

Figure 3.4: Camera lens setup for temperature variation experiments in the F900.

a high influence on the result. A common camera setup for experiments in the F900 is presented in Figure 3.4. The two cameras and lens systems described costs around 40.000 R$.

3.2.2 F900 illumination system

All the setup for conducting experiments with DIC in the furnace was optimized to use the blue layer of the images for the correlation, and the illumination was no exception. Different types of illumination were tested to evaluate its efficiency during experiments at 900 °C. The main concern regarding the illumination was the light intensity produced, especially in the blue spectrum, and its homogeneity of illumination in the specimens. Figure 3.5 brings one of the illumination tests conducted. The tests concluded that an all-blue illumination provided more stable results, a wider histogram (dynamic range) for the blue layer, and lesser variance for the blue layer when comparing reference images, as portrayed in Figure 3.6.

The different lue lighting.

Figure 3.5: Photographs of the experiment to define the lighting for the furnace and optimize the camera aperture parameter. The disc-shaped system (black and silver), attached to the end of the objective lenses, are the filter holders.

The final Illumination selected for the experiments was a 10W with 800 lumens spotlight blue projector with a narrow beam. Four are used on each side of the furnace, two per window. This illumination was selected because of its highly focused illumination enabled by a glass lens that aligns the light beams. Figure 3.7 shows the final illumination system.

3.2.3 Texture for high temperatures

Experimental results analyzed via DIC are greatly affected by the texture of the specimen. If the specimen tested does not have a natural pattern that can be used, usually, an artificial texture is prepared over the sample to create adequate conditions to apply the technique. Nonetheless, the texturing of the specimen can become a complex issue when dealing with high temperature experiments. Conventional inks cannot withstand high temperatures, and even commercial special inks for high temperatures, usually recommended for temperatures up to 600 °C, and even tough resisting, can slightly change their color.

Different strategies were tested for the texturing of specimens, being the most practical and effective the use of ceramic slip. The textures were applied by projecting droplets of the slip with the help of a paintbrush over the surface of the specimens. Creating an adequate pattern with this technique demands practice, however, as the slip is soluble in water, it is easy to correct mistakes during the

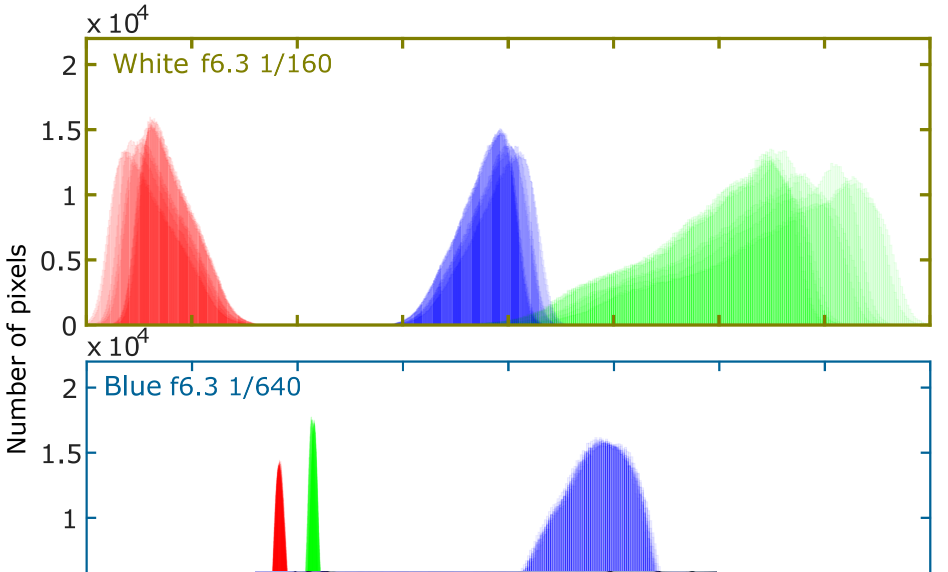

Figure 3.6: Evaluation of t s for white and blue lighting for a specimen in the F90

Figure 3.7: 10W projectors blue led illumination dedicated to one of the furnace's windows.

painting. Also, the textures created are stable for temperatures up to 900 °C. Figure 3.8 illustrates the change in contrast for a sample patterned with the silicon carbide slip before and after first heating.

The texture was also tested in a common furnace up to 1450 °C – staying one hour at this temperature – and did not stand the test, vanishing completely.

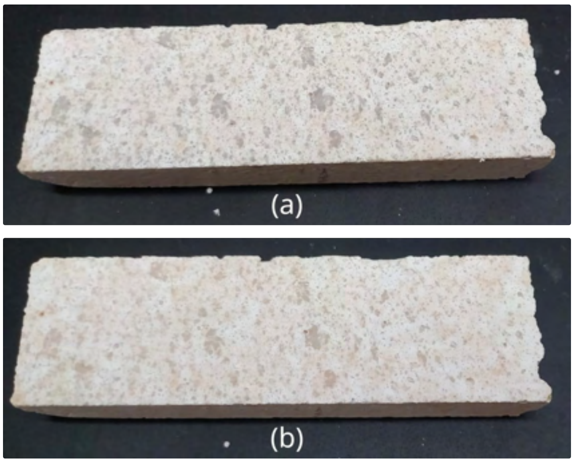

Figure 3.8: Silicon carbide slip pattern of a parallelepipedic sample (of approximately $10 \times 25 \times 120$ mm^3) (a) before and (b) after being heated up to 900℃.

However, there is no information about when the texture vanished in this process. In another experiment up to 1300 °C for several hours, the texture was used and remained visible. Therefore, more experiments at high temperatures must be made to evaluate the temperature texture limit.

For further in-depth of the problems faced when performing DIC on temperature variation experiments, see Appendix 5.2.

3.3 Materials selection

Investigate the interaction of material system phases due to CTE mismatch when submitted to a temperature variation is a main concern of this research. Therefore, the selection of the materials to integrate the model composites is of higher importance to the study, once the mechanical and thermomechanical properties of these materials will define the experimental results. The most important aspect to define these systems is the CTE mismatch among the phases, because this mismatch is the essence of the phenomena studied. Moreover, the elastic parameters also have a significant influence on the resultant stress among the phases. Finally, the matrix fracture toughness, alongside the other properties cited, will contribute to defining the temperature variation where cracks will appear.

Many materials and material systems were tested during the present research. Also, different configurations for the MCSs manufacture were used. Still, the main methodology used to manufacture the MCSs was casting alumina and colloidal silica into a silicon mold and positioning a second phase into the slurry. The mixture of alumina and colloidal silica was done following a weight proportion that depends on the type of alumina being used. The materials' ratio, defined for the casting, was evaluated empirically to use the minimum amount of colloidal silica in the process. Some specimens for different investigations and some inclusions were made by single-action powder pressing; this is due to the fact that this processing route was initially cogitated for the MCSs manufacturing process.

Once the matrix phase was decided, its properties were the base for the selection of inclusion materials that could produce the cracking of the system under temperature variation. A brass-alumina MCS was studied during the master's degree of the present author, and seeing that there were some gaps in investigations and processing to perform with this system, this was one of the systems chosen for the study. This system presents a high CTE mismatch, and the experiments performed during the previous research on the system do not fully characterize the phases or investigate in-depth aspects of the inclusion size and of the parametrization of the system cracking. Therefore, the previous results were further explored, and new MCS specimens were produced to continue the investigation.

There was also a will to create a ceramic-ceramic MCS. With the intention to create a system that under heating could produce radial cracks, two materials were brought to attention due to their CTE being higher than the one of alumina according to the literature, Magnesia and Zirconia, as can be observed in Figure 3.9. It is clear that a Magnesia inclusion would be the best candidate for an alumina MCS, however, due to lack of knowledge of pure magnesia processing routes, Zirconia was chosen as the material for a ceramic-ceramic MCS with alumina.

3.4 Specimens produced for the thermomechanical characterization

To simplify the understanding of the samples being tested in the results section, a display of the specimens manufactured is presented hereafter. Above the description of the specimens, the reference nomenclature chosen for each one is

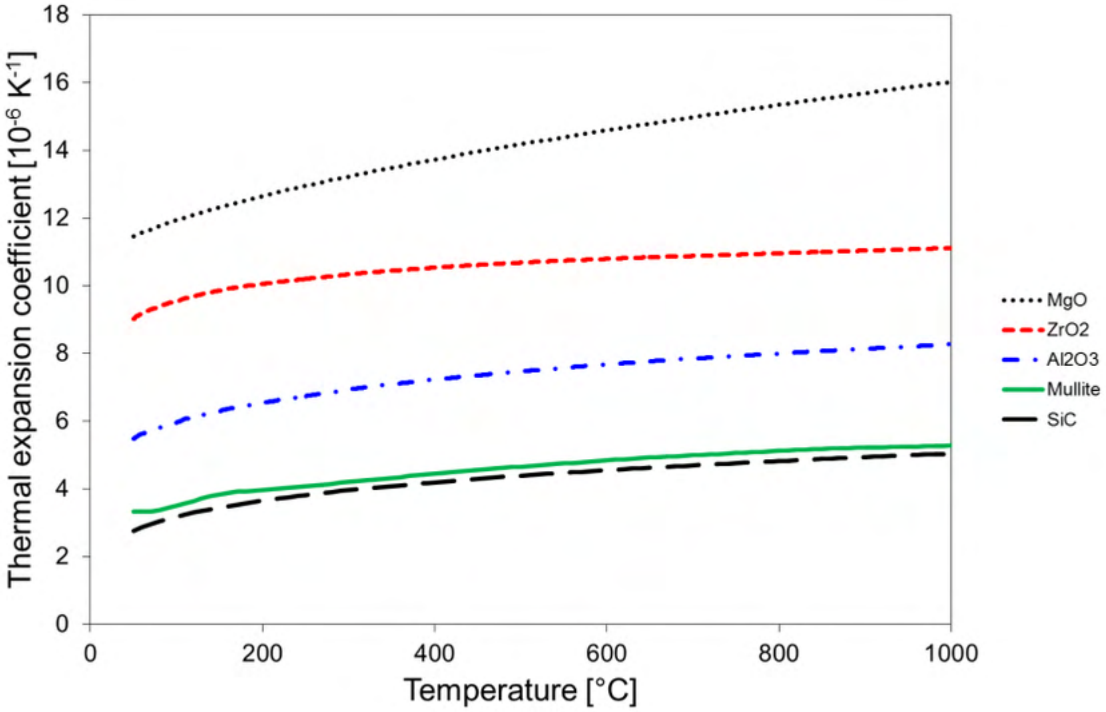

Figure 3.9: CTE temperature dependency for some ceramic materials [89].

underlined. To give some perspective of the use of each material and specimens that will be described, the materials, manufacture process, specimens geometry and function are displayed in Figure 3.10. Then, a more specific description of these different specimens are presented in the sequence. In Figure 3.10, is also showed the materials used for the matrix and inclusion of the model composites.

Most of the specimens processing was done in the ceramics laboratories of the Department of Material Engineering (DEMa) at UFSCar, but the machining of metal samples was performed at EESC-USP.

3.4.1 Pressed alumina specimen

Atomized Alumina Disc [AA-D]

The material chosen to validate the optical dilatometry tests proposed in this thesis was an atomized alumina powder with an average granule size of 75 μm. Samples were fabricated with this powder via single-acting uniaxial pressing using the equipment presented in Figure 3.11. The apparent density of the powder is 1.28 g/cm^3, and was obtained by direct measurements of the mass and volume of powder in a graduated glass by De Melo [90]. The material was supplied by

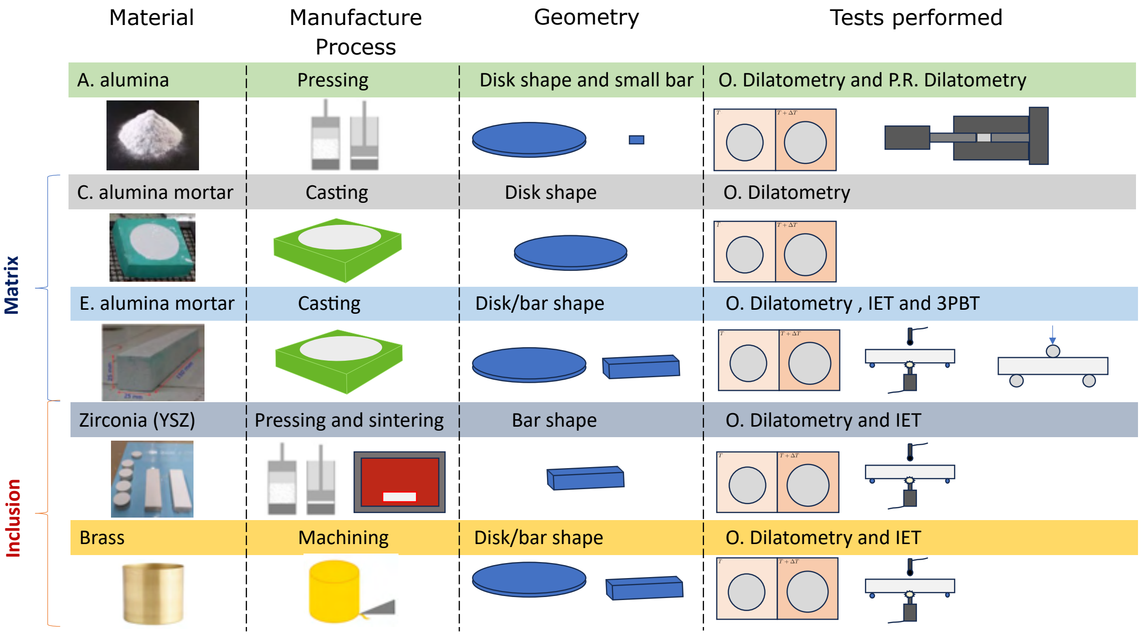

Figure 3.10: Summary of the specimen materials' manufacture, describing the type of manufacture employed, and the property characterization conducted on them.

Ceraltec Cerâmica Técnica Ltda, from Brazil. This first material was chosen for being a mechanically well-studied material inside the research group, but with a lack of information regarding its behavior with temperature. The specimens were prepared by pressing 100g of alumina using a 70 mm diameter die with a load of 40 kN.

3.4.2 Alumina slurry specimens

The alumina slurry specimens were all prepared by gel casting using a colloidal silica solution with 40% weight of silica. The specimens were cast into silicon molds after being the mixing of the constituents. The mold was then vibrated to produce more dense specimens. After molding, the mold with the material rested for two days usually at room temperature to dry and cure.

Calcined Alumina Disc [CA-D]

Calcined alumina specimens were prepared from calcined alumina powder A-2G mesh 325 μm in a 3:1 weight proportion of calcined alumina powder and colloidal silica in a gel casting process. The specimen was manufactured using a silicon mold and had 70 mm in diameter and 10 mm in thickness.

Electrofuse Alumina Square disc [EA-S]

Figure 3.11: Pressing machine used to produce specimens of atomized alumina and zirconia.

Alumina specimens were prepared from electrofused alumina powder (from Elfusa) mesh 200 in a 5:1 weight proportion of alumina and colloidal silica in a gel casting process. The specimen was manufactured using a silicon mold and had a square shape of 68.3 mm side and 0.9 mm in thickness.

An X-ray fluorescence test was performed on a crushed electrofused alumina slurry specimen to obtain its composition. The results showed a content of 84.5% of Al and 15.5% of Si, which corresponds roughly to 75% of Al_2O_3 and 25% of SiO_2.

Electrofused Alumina Bar [EA-B (1-8)]

Eight eletrofused alumina slurry bars were produced using silicon molds. The bars had a 25 mm of side square cross-section and a length of 150 mm. These specimens were produced to be used in the bar resonance technique and also the three-point bending test. Manufacturing these specimens follows a process

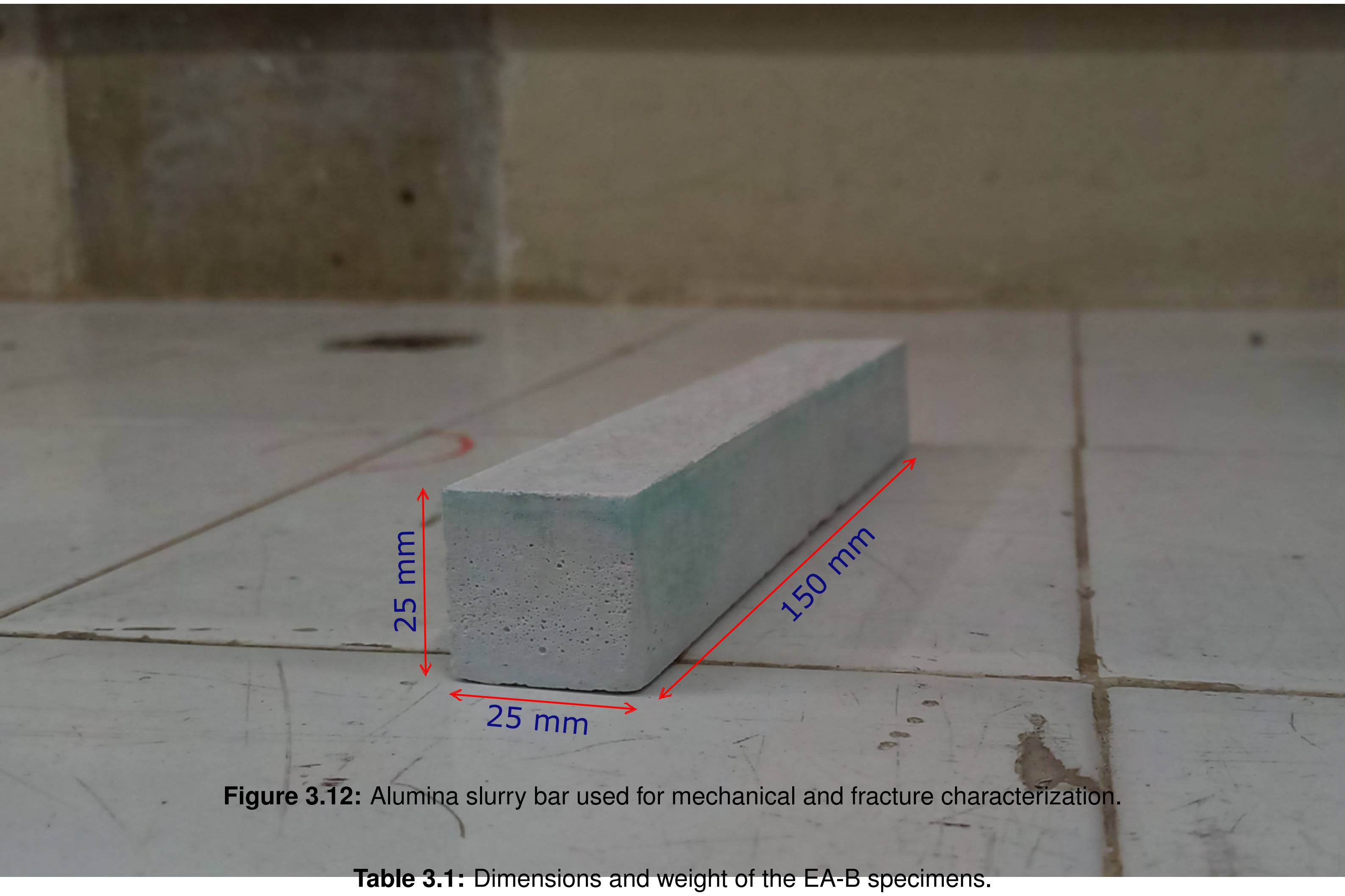

Figure 3.12: Alumina slurry bar used for mechanical and fracture characterization.

Table 3.1: Dimensions and weight of the EA-B specimens.

Specimen	Length (mm)	Height (mm)	Width (mm)	Weight (g)
EA-B1	157.5	23.5	25	235
EA-B2	158	24	25	237
EA-B3	157	24	25.2	238
EA-B4	158.5	24	25.2	237
EA-B5	158	24.9	25	233
EA-B6	158	25	24.9	236.7
EA-B7	157.3	24.2	24.6	233.2
EA-B8	157.5	24.9	24.7	238

3.4.3 Yttria stabilized zirconia specimens

Yttria Stabilized Zirconia Cylinder and Bar [YSZ-C and YSZ-B]

Specimens were produced of a Yttria Stabilized Zirconia (YSZ) mesh 300 sprayed powder, in cylinder and rectangular parallelepiped shape. The sample dimensions and weight of some specimens before sintering can be seen in Table 3.2 and Figure 3.13 (a). All samples were prepared by a pressing process with a pressure of 4 Tons using the steel dies shown in Figure 3.13 (b). After, the specimens were sintering at 1450℃, the final dimensions of the samples can be seen in Table 3.3 and Figure 3.13 (c). The linear specimen shrinkage was around 22%.

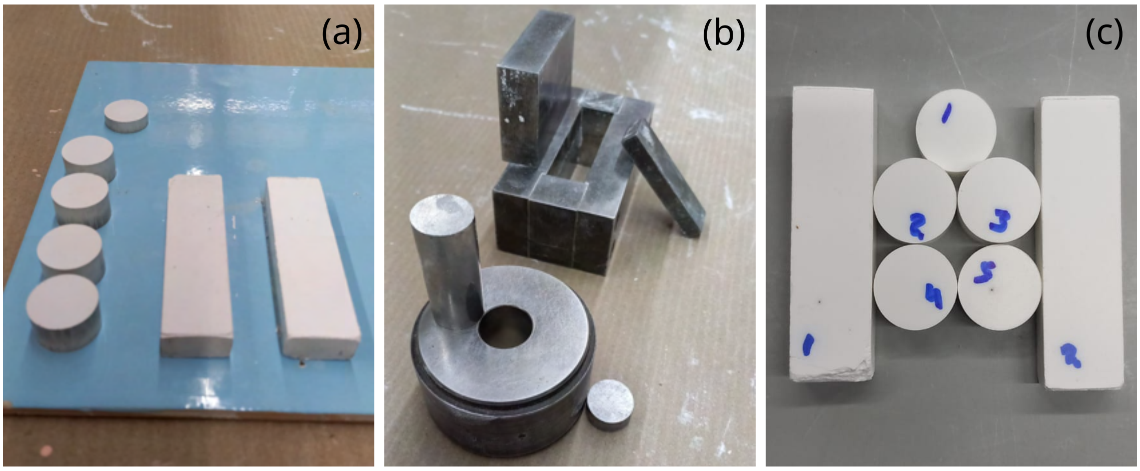

Figure 3.13: Zirconia specimens produced for dilatometry, mechanical characterisation and as inclusions for the model composites. (a) - zirconia green compacts; (b) - Steel dies used for the pressing; (c) - Specimens after sintering.

Table 3.2: Dimensions and weight of the YSZ green compact specimens.

Specimen	Diameter (mm)	Height (mm)	Length (mm)	thickness (mm)	Weight (g)
YSZ-C1	20	6	-	-	5.32
YSZ-C2	20	11.5	-	-	10.09
YSZ-C3	20	11.7	-	-	10.56
YSZ-C4	20	11.6	-	-	10.28
YSZ-C5	20	11.1	-	-	9.96
YSZ-B1	-	11.1	70.9	19.8	39.57
YSZ-B2	-	11.7	70.9	19.8	40.15

Table 3.3: Dimensions and weight of the YSZ sintered specimens.

Specimen	Diameter (mm)	Height (mm)	Length (mm)	thickness (mm)	Weight (g)
YSZ-C1	15.7	4.7	-	-	5.07
YSZ-C2	15.6	8.9	-	-	9.62
YSZ-C3	15.6	9.2	-	-	10.07
YSZ-C4	15.6	9	-	-	9.8
YSZ-C5	15.7	8.8	-	-	9.49
YSZ-B1	-	8.8	53.7	15	37.66
YSZ-B2	-	8.8	53.6	15	38.25

3.4.4 Brass specimens

Brass bar [BR-B]

A brass bar with square cross-section with dimensions of 22.2 x 22.2 x 211.8 mm and weight of 880.7 g was used to evaluate the mechanical properties of brass.

Brass disc [BR-D]

For the brass CTE evaluation, a brass disc with a diameter of 63.5 mm and a thickness of 7.75 mm was machined. This disc was tested in the F600 and F900. Black and white spray inks for temperatures up to 600 °C were used for texture in the F600 tests, and in the F900, a ceramic slip was used to produce the texture.

3.5 Model composite system specimens produced

3.5.1 Model Composite System Calcined Alumina and Brass [MCS-CAB]

This model composite was designed to be tested in the F600. It consists of a 12.7 mm of diameter single brass (C360) inclusion with a 2 mm diameter through-hole in its center embedded by an alumina slurry matrix with 120 mm of diameter made in a 3:1 weight proportion of calcined alumina powder (A-2G mesh, 325μm) and colloidal silica in a gel casting process. This alumina powder is white, has a specific mass of 3.97 g/cm^3, and the density of the loose powder is 0.7 g/cm^3. As a binding agent for the alumina powder, a colloidal silica solution with 40% weight of silica was used. A representation of the model composite manufacture process can be seen in Figure 3.14. Before the process, the mold was prepared with a Redelease® green silicon, and the template and inclusion were machined. The purpose of these materials phases was to produce a system with a high CTE mismatch to ensure the cracking of the system even for lower temperature variations.

3.5.2 Model Composite System Electrofuse Alumina and Brass [MCS-EAB]

MCS-EAB is similar to MCS-CAB; the idea was to maintain a known system that fails with low-temperature variations, and that can be well characterized. This system comprises brass as the inclusion and electrofused alumina slurry as a matrix, being that both phases were well characterized.

The model composite has 90 mm of diameter. The alumina slurry matrix was

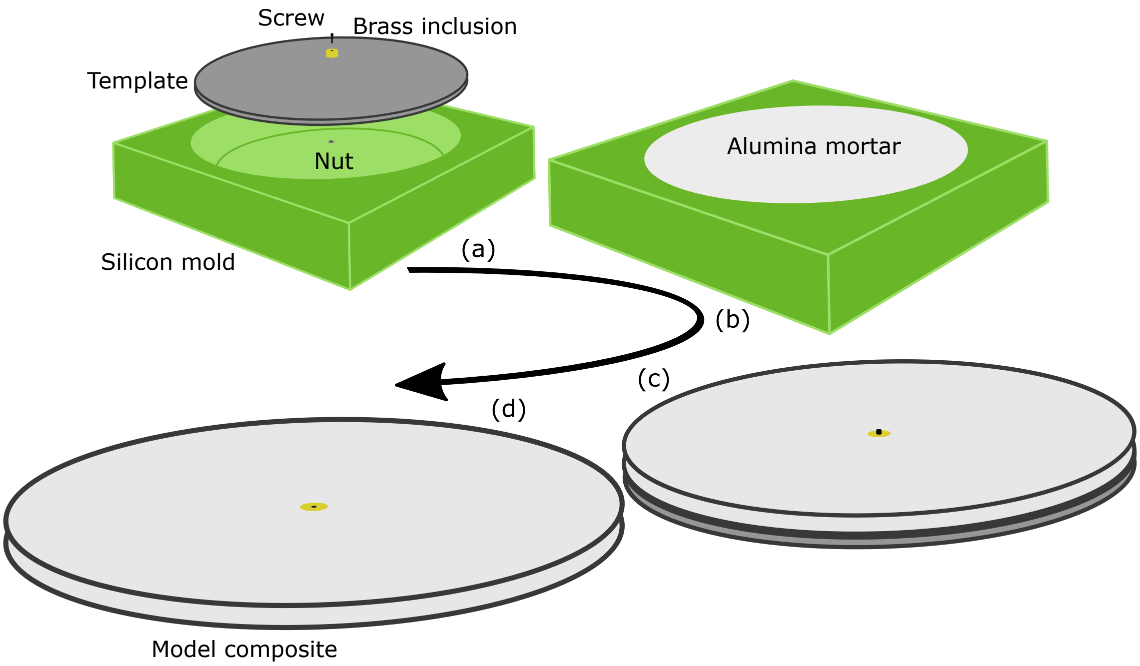

Figure 3.14: Manufacture route of the model composite: (a) assemble of the inclusion, template, and mold; (b) alumina and colloidal silica scattering over the mold, and put inside a furnace at 40 °C to cure and dry; (c) removal of the model composite and template from the mold, and sand of the model composite surface until the matrix reach the inclusion height; (d) release of the model composite from the template [54, 65].

made in a 5:1 weight proportion of electrofused alumina powder mesh 200 (Particle size $\leq 74\ \mu m$) and colloidal silica in a gel casting process. The manufacture of the specimens for MCS-EAB were similar to the MCS-CAB, however, the inclusions were manually positioned instead of fixed during the matrix scattering in the mold.

Different MCS-EAB specimen were produced. For this system, specimens were manufactured with different numbers of inclusions and also with different sizes of inclusion. Table 3.4 presents the specimens produced.

Table 3.4: List of MCS-EAB specimens produced

Inclusion diameter	1 inclusion	2 inclusions	3 inclusions	Multiple inclusions
12.7	✓	✓	✓	
8.1	✓			
4.7	✓			✓

3.5.3 Model Composite System Electrofuse Alumina and Yttria Stabilized Zirconia [MCS-EAYSZ]

This model composite was designed to be tested in the F900. The smaller difference among zirconia and alumina slurry CTE in relation to MCS-CAB, leads to the expectation of a failure due to CTE mismatch in higher temperature variations. Also, this ceramic-ceramic system represents a more realistic composite in terms of materials used for high-temperature application once many refractories are based on alumina and zirconia. It consists of a 20 mm of diameter YSZ (Yttria Stabilized Zirconia) with 3% of yttria embedded by an alumina slurry matrix with 90 mm of diameter made in a 5:1 weight proportion of electrofused alumina powder mesh 200 (Particle size ≤ 74 μm) and colloidal silica in a gel casting process. The manufacture of the specimens for MCS-EAYSZ were similar to the MCS-CAB, however, the inclusions were manually positioned instead of fixed during the matrix scattering in the mold.

3.6 Dilatometry tests

The first step in understanding and evaluating the consequences of a temperature variation acting on a composite is to know the CTE relation of the phases. In this section, the methodologies applied to measure the CTE mismatch of the phases are presented. The main idea was to validate an optical dilatometry methodology using DIC by comparing its results to those of a Push Rod Dilatometer. Then, this optical dilatometry is used to evaluate the CTE of materials of interest to this Thesis.

It is important to highlight that the CTE of a material is a function of temperature. Therefore, while the thermal strain results are typically presented as a function of a temperature variation, when computing the CTE, this value must refer to a temperature value.

The evaluation of a material's linear coefficient of thermal expansion relies on the temperature control of the sample and the appliance of a measurement technique to evaluate its change in length. These two factors, despite simple, can become real challenges. The heating or cooling of a sample must be done carefully to ensure that the sample has a homogeneous temperature and is in temperature equilibrium with the heated environment. For these reasons, many dilatometry techniques operate with small samples and ovens. Another option would be to work with lower temperature rate changes or to use long temperature plateaus. The evaluation of the length change must be done by a robust system once it deals with very small changes in length, and also because when dealing with contact measurement techniques, the expansion of the equipment parts must be taken into account to properly measure the expansion of the material.

There are some ways to evaluate the linear CTE of a material, being the simplest of them, to use a push rod dilatometer. This type of dilatometer uses a push rod with a small load to fix the sample, and measures the length change of the sample when heated. The measurement is made by a Linear Variable Differential Transformer (LVDT) system that is coupled to one of the ends of the rod while the other end is in contact with the sample. A calibration with standard samples is made to ensure no parasite influences on the equipment. Therefore, the two dilatometry techniques described here will be presented, along with the equipment used in each type of experiment, the principles involved in the methodology, and their advantages and limitations.

3.6.1 Push Rod Dilatometry

The push rod dilatometry is a contact measure technique. In order to conduct a dilatometry procedure, the equipment must be calibrated with a reference sample to ensure that all expansion of the equipment parts is being subtracted from the total expansion attained. With the calibration performed, the sample of interest can be tested and the results acquired. Being a contact measure technique in which the sample is fixed by a small pressure applied by the rod, the technique produces an accurate measure as long as the materials stiffness is not significantly reduced in the measuring temperature. This reduction in stiffness can impact the material expansion evaluation if the pressure imposed by the rod produces a strain that interferes in the real expansion evaluation.

The dilatometer used was the NETZSCH - DIL 402 C Push Rod Dilatometer, Figure 3.15. This dilatometer has an LVDT measurement system with a resolution of 1.25 nm, and can be used in to test samples up to 50 mm of length. The equipment has a precision of ± 0.1 ℃ in temperature measure.

The dilatometry was conducted with a heating rate of 5℃/min from 25℃ to 900℃ in a sample of pressed atomized alumina. First, a calibration run of the experiment was done with an alumina standard sample following the temperature set to obtain calibration parameters. After that, dilatometry of the materials of interest was conducted following the same temperature set used for the calibration run. The results are then corrected with the calibration run parameters identified, following the standard procedure suggested by the manufacturer. The dilatometry results were extracted in text format and processed in the software MATLAB® for comparison with the results attained by the optical dilatometry via DIC for the atomized alumina.

Figure 3.15: NETZSCH - DIL 402 C push rod dilatometer used for measurement of the material samples CTE.

3.6.2 Optical dilatometry via Digital Image Correlation

The principle of the optical dilatometries consists of obtaining the thermal strain via optical measure techniques and then post-processing the results to compute the linear CTE of the materials for each temperature. The optical dilatometry proposed here is executed by acquiring photographs of a specimen under a temperature variation. Images of the initial temperature of the experiment are used as the reference state to evaluate the noise of acquisition. Images are then acquired for increment temperature values and compared with one of the reference images to obtain the displacement fields that correlate the images. This strategy uses a finite element mesh to find the displacement fields between the images globally.

Optical dilatometry were conducted in both ovens, however, there are significant differences regarding the efficiency that could be achieved in each experimental setup. The F600 was conceptualized as having a vertical visualization. This setup contributes to a smaller temperature gradient in the specimen once the F600 has only one heating zone in its bottom. However, this configuration contributed to a parasite out-of-plane displacement in the results. The F900 enables the visualization of both sites of the specimen inside, allowing to deal with most of the parasite out-of-plane displacement effects by using the average values of the two opposite sides of the specimen.

For the conduction of dilatometries in the F900 the specimens were textured with high-temperature ink spray (up to 600 ℃) or silicon carbide slip (up to 900 ℃) depending on the maximum temperature envisioned for the test.

3.7 Mechanical characterization

3.7.1 Impulse Excitation Technique

The Impulse Excitation Technique (IET) is a non-destructive measurement technique based on the match, by an interactive process, of a build-up frequency obtained by a fast Fourier transform to a measured vibration frequency using a Resonant Frequency and Damping Analyzer (RFDA) software. The technique is capable to evaluate the Young's and shear modulus as well as the Poisson's ratio. The test consists of the position of a sample over two points (nodes), where the specimen is gently tapped by an excitation device in one region while a microphone captures the frequency in another region. The node points, the excitation device and microphone positioning will depend on the specimen geometry and the properties being measured. The geometry and weight of the sample are also used for the properties' evaluation. Figure 3.16 illustrates the test [84].

3.7.2 Three-point bending test

Three-point bending tests were conducted with the electrofused alumina slurry bars (EA-B) for the evaluation of its fracture stress and Young's modulus. The tests were conducted in a Universal Testing Machine (UTM) MTS Exceed E44.304 (30 kN capacity). Cameras Canon EOS 5DS were used to obtain images of both opposite sides of the tested specimens.

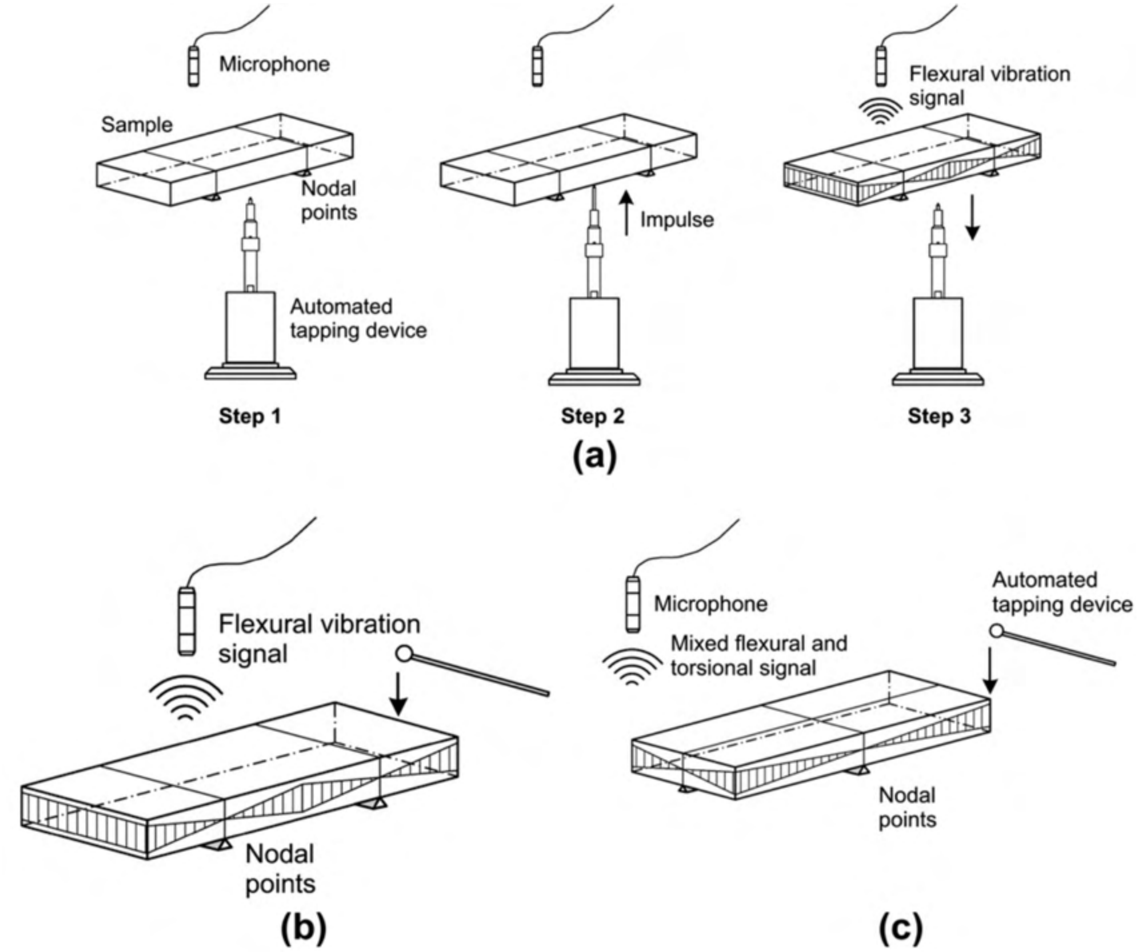

Figure 3.16: Impulse Excitation Technique (IET): (a) principle; (b) determination of the Young's and (c) the shear modulus [84].

To calculate the Young's modulus of the tested material, Euler-Bernoulli beam kinematics was used [91]. Two beam elements are needed in the present case, whose nodes are horizontally positioned at the load application points. Therefore, integrating analytical equations to describe the kinematics approach (also called Integrated-DIC [92]) enables trustworthy results while avoiding the need for post-processing displacement fields and diminishing possible uncertainty propagation. In the present case, there are 9 degrees of freedom to be determined, namely, 6 translations and 3 rotations at each element. By construction, with the selected shape functions, the displacement, and rotation fields are continuous. Further constraints were added (via 5 Lagrange multipliers), namely, continuity of the curvature, no bending moment (*i.e.,* zero curvature) at both ends of the beam, no global extension/contraction of the beam. With such hypotheses, there are only 4 degrees of freedom, namely, the three rigid body motions and the beam deflection. With such reduced kinematics, noise influence is reduced and a more robust estimate of the Young's modulus, E, is calculated from the curvature κ at the top support:

$$E = \frac{M}{\kappa \, I_0} \tag{3.1}$$

where I_0 is the inertia moment of the cross-section, M the bending moment at the load application point. The derivative of the curvature, which is piece-wise constant, is proportional to forces on the two lower supports. From this information and the global equilibrium of the beam, the bending moment is computed as a function of the applied load [93].

In order to conduct mechanical tests in high temperatures, special actuators were machined. These actuators were designed to resist elevated temperatures without oxidation and avoid excessive heat transfer to the load cell. A system made of aluminum sheets and small fans was designed and attached in the 20 mm gap between the furnace and the UTM columns (at each side) to avoid overheating (see "lateral cooling" in Figure 3.2 and "Wind cooling system" in Figure 3.18). This solution allows the lateral column temperature to be less than 50℃ while not removing too much heat from the furnace laterals, which would demand more energy to control the furnace inner temperature. Preliminary ther-

Stainless steel actuator coupling water cooling system

Stainless steel actuator coupling water cooling system CAD project

Actuator produced for high temperature tests

Figure 3.17: Actuator system for high temperature mechanical experiments.

mal analysis in Finite Element (FE) commercial codes indicated that the external part of the actuators could reach up to 300 °C if no cooling were utilized. Therefore, another cooling part was designed to be coupled at the outer end of each actuator, with inner channels connected to a water pump whose aim is to remove heat near the load cell to an external reservoir, keeping its temperature less than 40 °C (the maximum working temperature given by the manufacturer). The special actuator and the water cooling system are presented in Figure 3.17. The setup to execute the three-point bending test is displayed in Figure 3.18.

3.8 Model composite system temperature variation tests

3.8.1 F600 temperature variation tests

An experiment was designed to evaluate the interaction between the composite material's phases. The purpose of this experiment consists of obtaining the displacement fields of the biphasic model composite while it is submitted to a temperature variation, being that the model composite has a thermal expansion coefficients mismatch between its phases. The model composite is textured and placed inside the F600 (Figure 3.19). The temperature variation test consists of

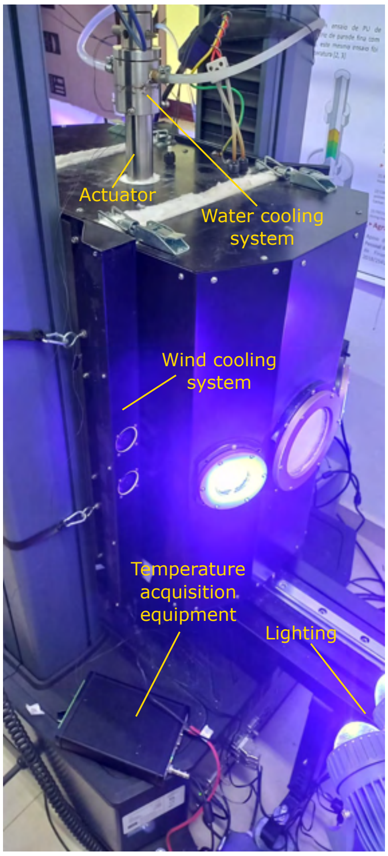

Figure 3.18: F900 during high-temperature three-point bending test.

a constant heating rate from 40 to 300 °C, after a temperature stabilization of at least 30 minutes in 40 °C. One photograph is taken per minute, and the heating rate is 1 °C per minute. The same temperature variation procedure is used to evaluate the coefficient of thermal expansion of each one of the material phases.

With the photographs of the experiment, a DIC analysis is conducted to the identification of the displacement fields using the software Correli 3.0 (implemented in MATLAB®) developed by Hild and Roux [43, 77].

3.8.2 F900 temperature variation tests

The MCS temperature variation experiments conducted in the F900 were executed according to the following procedure:

- The MCS specimen is texturized with high-temperature ink, or silicon carbide slip;
- The MCS specimen is positioned inside the center of F900 with thermocouples to acquire the temperature data;

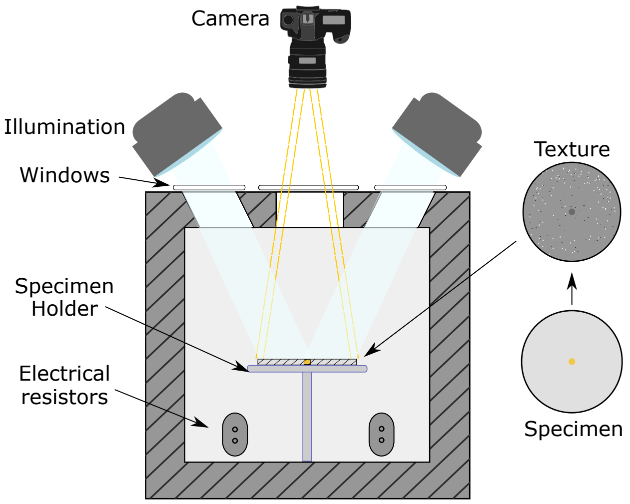

Figure 3.19: Temperature variation test assisted by DIC. Experimental apparatus and thermal chamber [65].

- The camera and illumination system are adjusted equally in distance on both sides of F900;
- Reference images are acquired to evaluate the image acquisition noise.
- The furnace is heated at a 2 ℃/min rate while 1 image is acquired per minute.

It is important to highlight that before the heating step of the experiment a rigorous experimental setup of cameras alignment, focus, and other camera parameters selection was performed. The reference images were taken for texture analysis to evaluate the quality of texture and lighting. Once the evaluation displayed good results, the experiments were performed.

3.9 Computational methodology conducted for data processing

This section is intended to make it easy to understand how data was processed in the numerous results that will be shown in the next chapter. Generally speaking, most of the data acquired experimentally were post-processed, especially the field data.

The main software tool used was MATLAB®, in which data was generated in the DIC process and gathered from the files generated by equipment (Dilatometer, LYNX® temperature measure devices, UTM, etc...), and from other software. In MATLAB® codes were developed to evaluate the thermal strain and CTE of

DIC optical dilatometry, to remove thermal and elastic effects from the model composites temperature variation experiments using fitted analytical model and FEM model results and to generally obtain different fields from the DIC results. Although several processing strategies have been used to conduct the investigations proposed in this work, the general proceeding conducted is the gather of data from different sources into MATLAB® and work the data in there. This idea is represented in Figure 3.20.

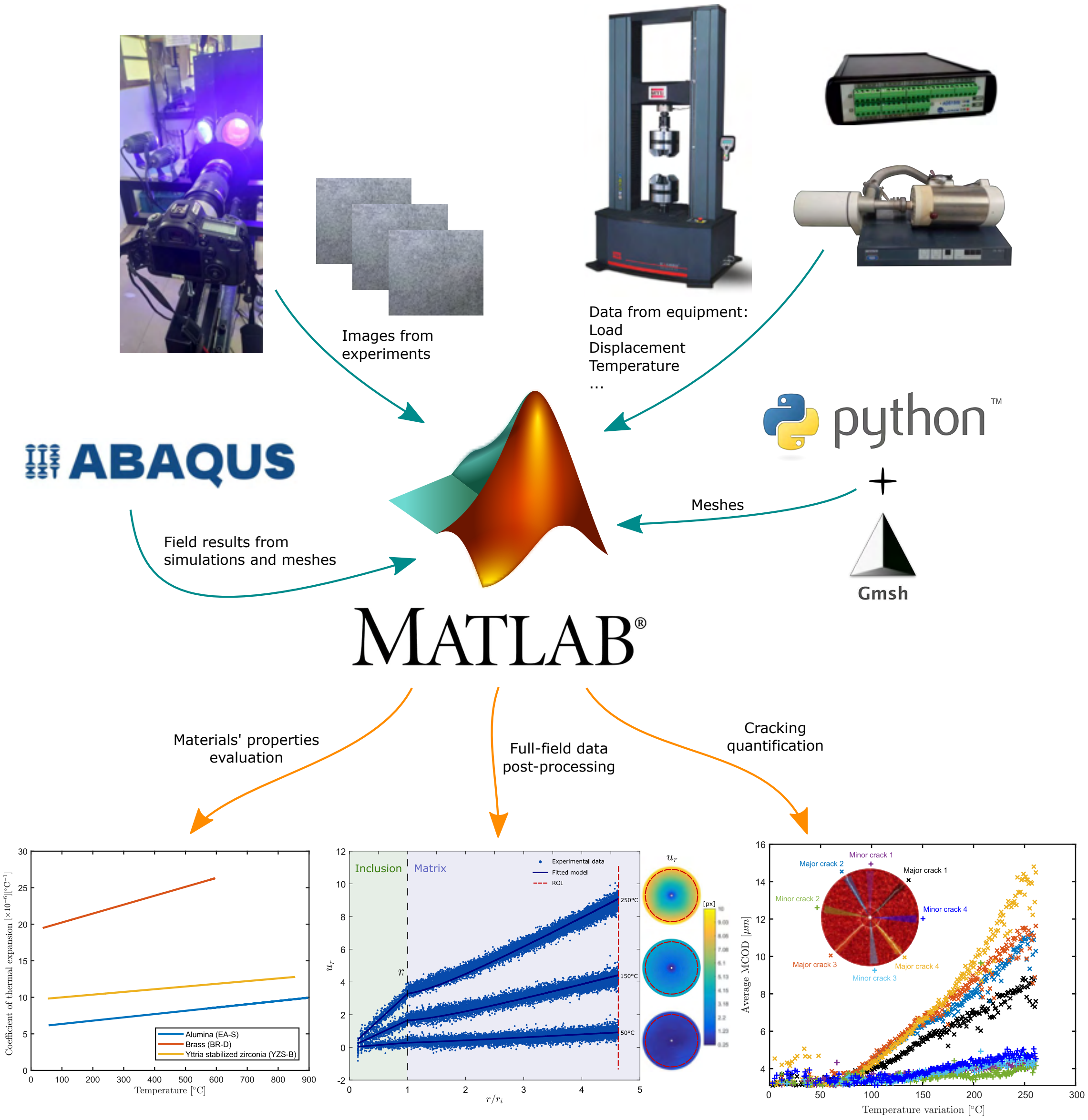

Figure 3.20: General data processing structure conducted to produce the results of the present thesis.

Most of the finite element mesh produced for the DIC was done in Python using a library to interface with the finite element mesh generator software GMSH. The mesh created were saved as mat files and imported in MATLAB® for the correlations. The mesh could be constructed directly in MATLAB®, but the Python codes developed allowed a fast and easy solution to create different mesh geometries, mesh domains, and element characteristics.

The data from experimental equipment were extracted as text files and imported in MATLAB®. The temperature acquisition device's data were used in the evaluation of CTE of materials, and as temperature information for the model composites temperature variation cracking evaluation. The data from the dilatometer was used to evaluate the optical dilatometry results through comparison. The UTM data was used as input for the Integrated correlation of the three-point bending experiments images. Only the IET experiments were not post-processed, once the RFDA software already provides the information of interest and there was no field information in regard to these experiments.

With respect to FEM simulations, the software Abaqus^{TM} was used to produce models simulating the temperature variation of the model composites. These models were developed to obtain the linear elastic response of these simulations. The resultant fields of the simulations were extracted as text files, and then, imported in MATLAB® to be used in the post-processing of the model composites temperature variation DIC results.

3.10 Materials and methods conclusion

The research conducted in this thesis is an investigation of the thermomechanical behavior of composite systems and a vast development in methodologies to investigate this subject. The development of means to investigate this subject passed through the conceptualization of equipment, specimen geometry, materials, and manufacture; texture, illumination, and image acquisition solutions; and finally, experimental procedures' development. Regarding the development of the tests, much of them were performed in redundancy or with validation, *e.g.,* optical, and push-rod dilatometry; IET and three-point bending test. Also, the chapter presents in a clear way that the main idea behind this research is not to study a specific material system but to better understand and produce experimental data on crack phenomena related to the CTE mismatch in composite systems under temperature variation.

4 RESULTS

This chapter describes the main results of this thesis regarding the investigations conducted. First, the optical dilatometry results are presented. Then, the results of the mechanical tests. Finally, results of Model Composites cracking due to CTE mismatch in temperature variation experiments are explored.

4.1 Optical dilatometries results

4.1.1 Tests for the validation of the optical dilatometry technique by comparing it to the NETZSCH - DIL 402 C push rod dilatometer

To evaluate the viability of evaluating the thermal expansion of the materials using DIC, a test comparison was made using AA-D specimens. An optical dilatometry with the two-camera set-up was conducted in the F900, while a sample of the same material was prepared to be tested in the NETZSCH - DIL 402 C push rod dilatometer. Figure 4.1 displays one of the reference images of the experiment and the mesh used for correlation.

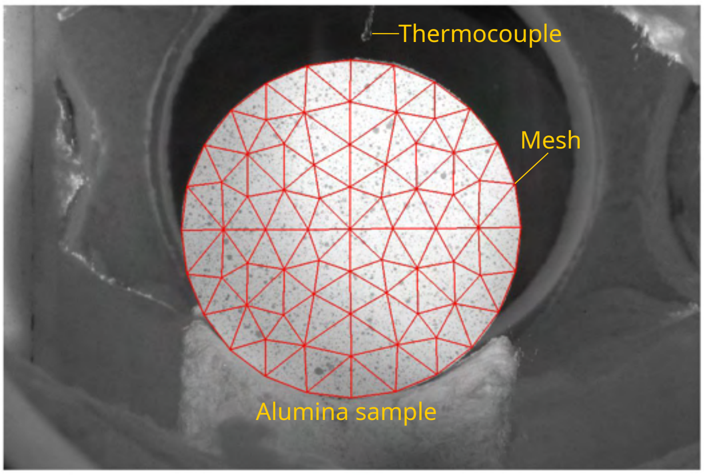

Figure 4.1: AA-D sample inside the oven and finite element mesh used for its correlation [93].

Both tests were conducted with a heating ratio of 5 °C/min. At first, the results seem to disagree. After some investigation, it was possible to conclude that the heating ratio used was too high for the optical dilatometry due to the larger volume of the sample and also of the furnace chamber. However, images of the specimen

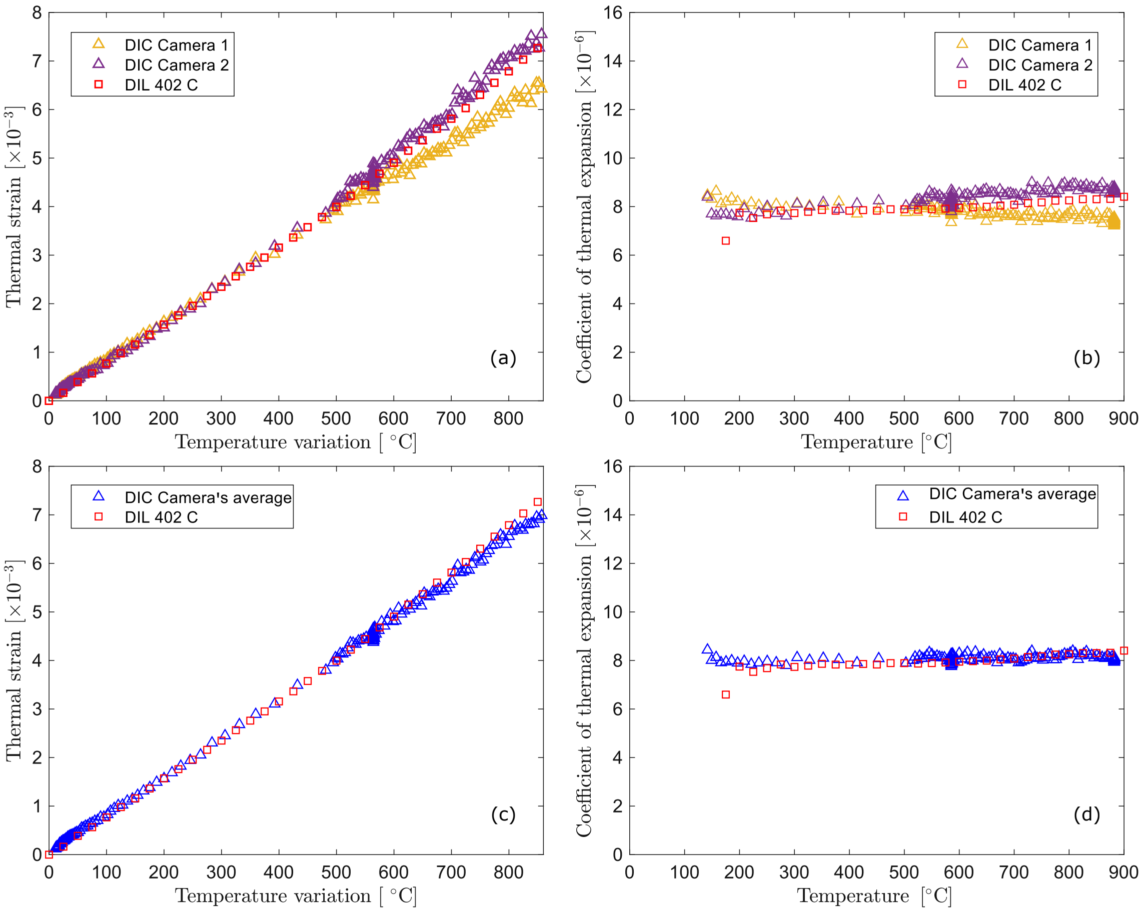

Figure 4.2: Comparison of the optical dilatometry with the push-rod dilatometry results: (a) thermal strain measured by each camera compared to the push-rod dilatometry evaluation; (b) secant CTE measured by each camera compared to the push-rod dilatometry evaluation; (c) average thermal strain of the cameras compared to the push-rod dilatometry evaluation; (d) average secant CTE of the cameras compared to the push-rod dilatometry evaluation.

cooling were attained along with the temperature register. Using this data for the evaluation of the experiment showed a very good agreement with the push-rod dilatometry when using the camera's. Figure 4.2 brings the two dilatometry techniques result comparison. In Figure 4.2 (a) and (b) it is possible to see that each camera result do not agree with each other or with the push-rod dilatometry, while in (c) and (d), the average result of the cameras presents a great agreement with the push-rod dilatometry.

4.1.2 CA and BR-D optical dilatometries (F600) - MCS-CAB constituints

Optical dilatometries in the F600 were conducted for the materials of the MCS-CAB, being the brass and calcined alumina slurry matrix. The mean thermal strain fields for the brass and alumina specimens were fitted using a homogeneous second-order polynomial, being, ε_a and ε_b, the fitted polynomials for the alumina and brass, respectively.

$$\varepsilon_a = 4.3251^{-08}\Delta T^2 + 5.4729^{-06}\Delta T \tag{4.1}$$

$$\varepsilon_b = 4.7467^{-08}\Delta T^2 + 2.1587^{-05}\Delta T \tag{4.2}$$

Figure 4.3 (a) shows the results for the thermal strain evolution measured versus temperature variation. The CTE difference between the phases ($\Delta\alpha$) at 50°C is 16.12×10^{-6} and grows linearly to 17.17×10^{-6} at 300°C (Figure 4.3 (b)). Due to the experimental setup, the displacement fields attained, and consequently, the CTEs, have a parasite increment from the out-of-plane motion of the sample [82]. This out-of-plane motion results from the sample holder support rods of stainless steel. However, since the experiments have the same procedure, the parasite out-of-plane displacement was similar, and therefore, the CTE mismatch can be considered a valid evaluation.

4.1.3 BR-D optical dilatometries (F600 and F900)

Each dilatometry conducted on the F900 was performed with image acquisition of both opposite faces of the specimens tested, with the cameras positioned at the same distance from the specimen. This procedure allows using the mean thermal strain of the faces results, which ensures the absence of out-of-plane disturbance, once the out-of-plane displacement of one side is counter-measured with the other side. This strategy, that was only possible due to the oven windows configuration, allowed to effectively measure the CTE of the materials tested, avoiding the problems faced in the F600 optical dilatometries.

It was known that the dilatometry experiments conducted in the F600 had suffered from parasite strain caused by out-of-plane motion. To accurately evaluate the CTE of Brass, a new dilatometry was then conducted in the F900 with the very same specimen once tested in the F600. This time, both sides of the specimen were photographed, avoiding the major influence of out-of-plane motion. The comparison results of the two dilatometries are presented in Figure 4.4.

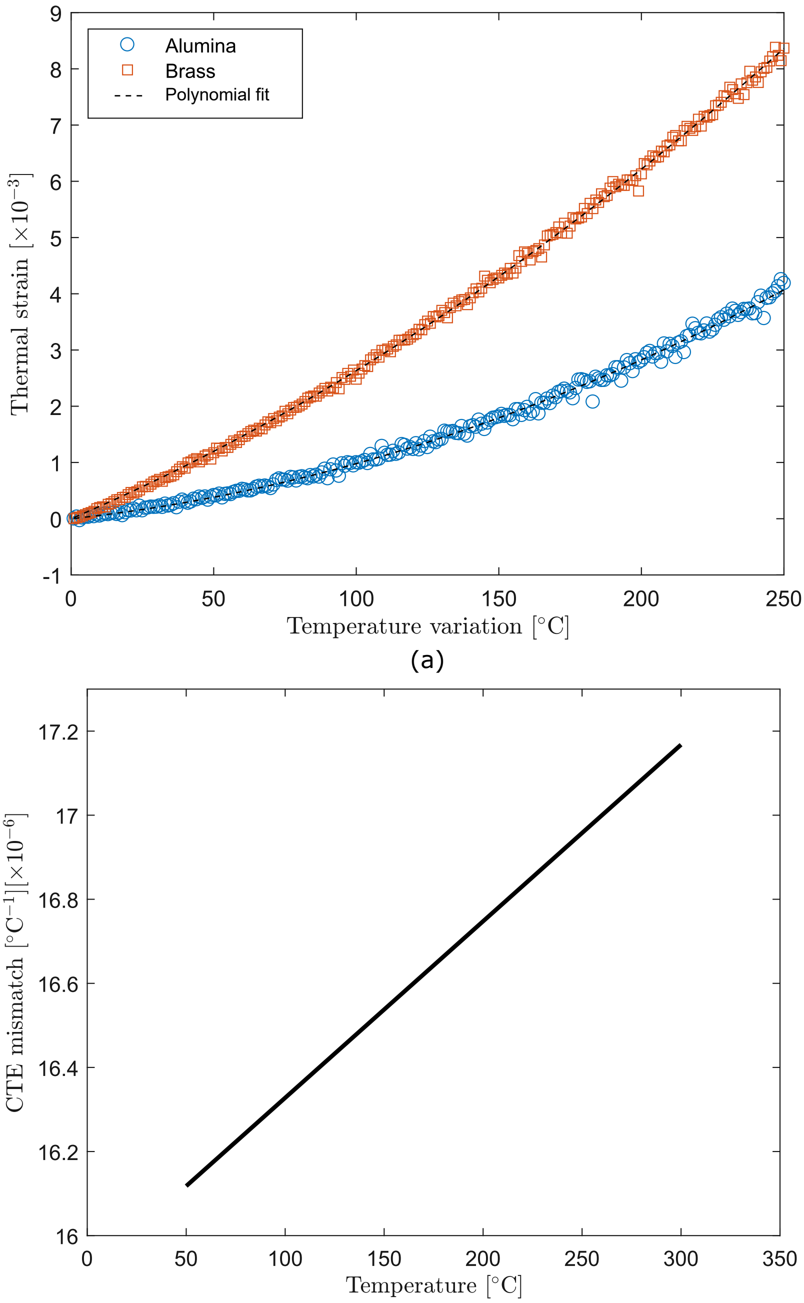

Figure 4.3: Dilatometry tests results: (a) alumina and brass thermal strain evolution for a temperature variation of 0 to 250°C attained via optical dilatometry; (b) coefficient of thermal expansion (CTE) mismatch between alumina and brass from 50 to 300°C [65].

4.1.4 YSZ-B optical dilatometries (F900)

The YSZ-B specimen was textured with a silicon carbide slurry. The dilatometry analysis carried out in the F900 furnace while acquiring images from two opposite sample faces. The cameras were positioned at the same working distance

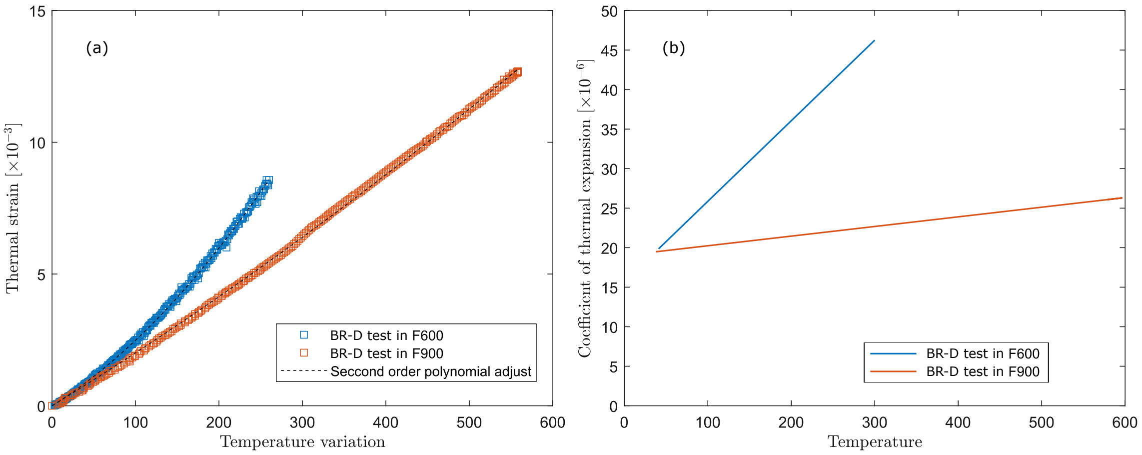

Figure 4.4: Comparison of dilatometry results of the same brass specimen tested in the F600 with one camera and F900 with two cameras: (a) thermal strain; (b) tangent coefficient of thermal expansion.

from each opposite monitored surface. This procedure allows the use of the average thermal strain between both analyzed faces, compensating for out-of-plane rigid motions. This strategy was possible thanks to the ability of visualizing two opposite faces, which allowed the Coefficient of Thermal Expansion (CTE) to be evaluated for the YSZ specimen. The temperature acquisition was obtained with a thermocouple close to the specimen. The experiment was performed with an image acquisition rate of one frame per minute and a heating rate of 2℃/min. The initial temperature was set to 50℃, and the experiment was carried out as a single ramp until the control system reached 850℃, when a dwell was kept for 30 minutes, before ending the experiment.

A blue rectangle delimits the specimen positioned over a flat surface in Figure 4.5(a,b), with the larger faces of the specimen facing each camera. A rectangular mesh with three-noded linear triangular elements (T3) with a mean size of 2.4 mm (or 179 px) was used to quantify the expansion of the YSZ specimen. The horizontal and vertical displacement fields, after removal of rigid body motions, are shown in Figure 4.5(c,d) and 4.5(e,f), respectively, for the maximum temperature of the experiment (850℃) where the displacement magnitude is less than 200 µm. The displacement uncertainties were evaluated with twenty reference images before heating started. It was on average equal to 5 cpx (*i.e.,* ≈ 0.7 µm).

The differential or tangent CTE α is calculated using the strain increment $d\varepsilon^t$

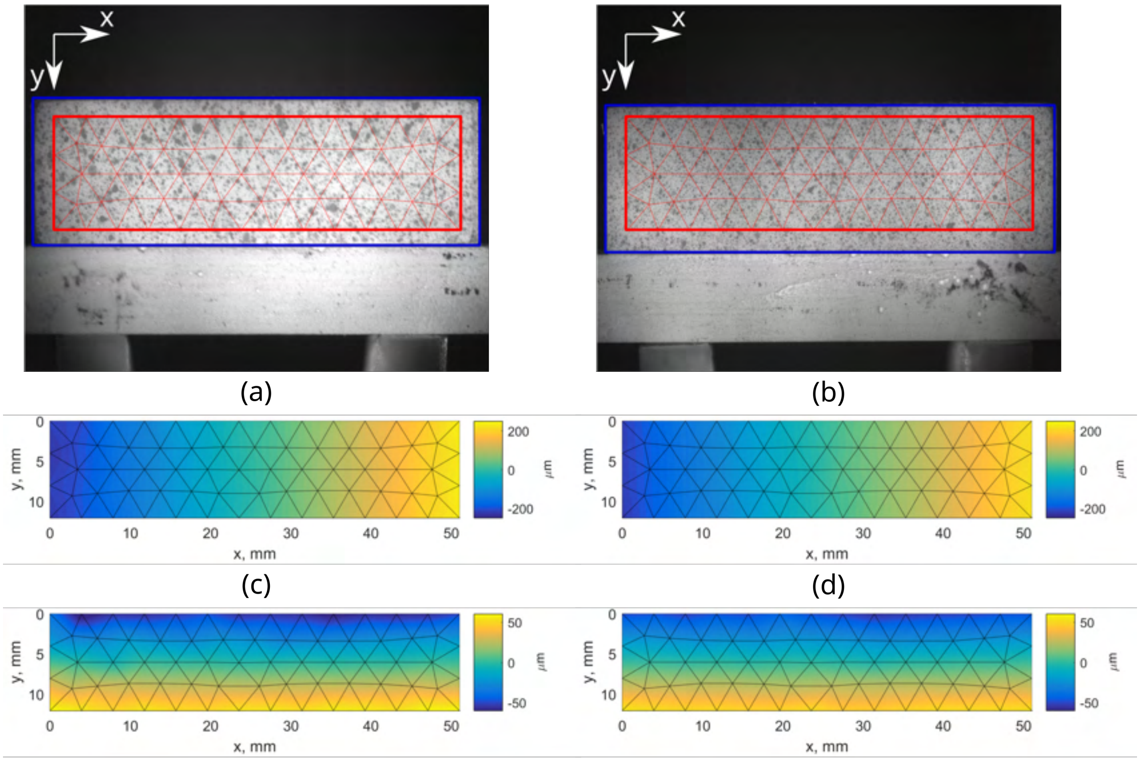

(a) (b) (c) (d) (e) (f)

Figure 4.5: (a,b) References images with the meshes (in red) used for analyzing the YSZ specimen dilatometry up to 850 ℃. (c,d) Horizontal and (e,f) vertical displacement fields for the maximum temperature. Sub-figures for the front face in (a,c,e) and for the back face in (b,d,f). In the images, 1 px ≈ 13.4 µm [93].

from an infinitesimal temperature variation dT

$$\alpha = \frac{d\varepsilon^t}{dT} \tag{4.3}$$

The CTE of YSZ was obtained by evaluating the mean thermal strain variation, $d\varepsilon^t$, which was considered as the average of the maximum and minimum eigenstrains for all the elements in the mesh as a function of the temperature variation. In the present case, the standard uncertainty of $d\varepsilon^t$ was equal to 2.5×10^{-4}.

The thermal strains measured for each camera and the corresponding average (with its standard deviation) are presented in Figure 4.6(a). The CTE values from each camera or considering their average are compared in Figure 4.6(b) to the results reported by Hayashi et al. [94], where the CTE of YSZ with different concentrations of yttria from -173 to 627 ℃ were evaluated via push-rod dilatometry. Despite differences of $\pm 1 \times 10^{-6}$ ℃$^{-1}$ in CTE values measured using the average result and by Hayashi et al. (Figure 4.6(b)), the slopes are virtually the same. The results considering both cameras separately led to different slopes. The difference in the comparison with Hayashi et al. may be explained by the different approaches to obtaining the differential CTE. While in this paper, the CTE was obtained by the derivative of an adjusted second-order polynomial of the thermal strain, Hayashi et al. used moving averages for filtering the thermal strains, evaluating the differential α from sampling each 0.2 s. Minor differences in yttria content may also lead to such differences.

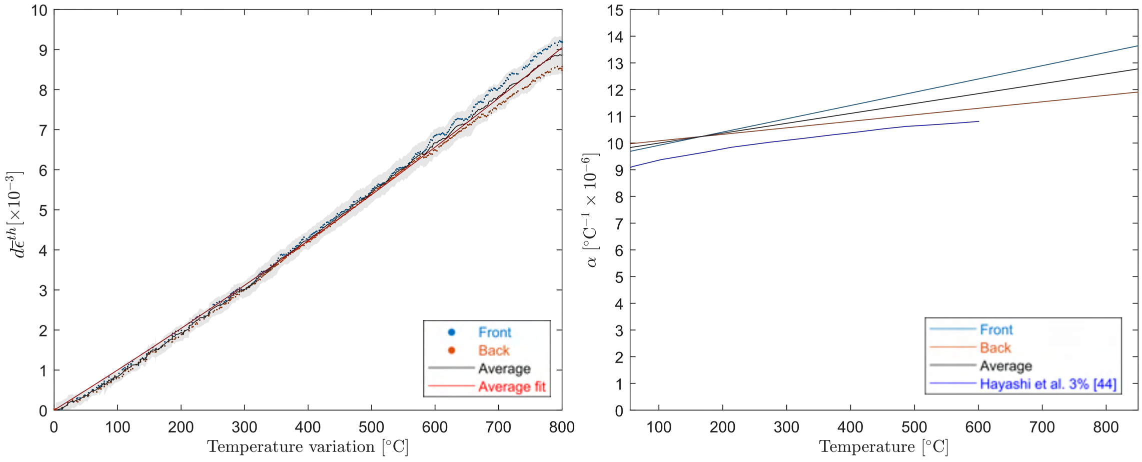

(a) (b)

Figure 4.6: Dilatometry test conducted in the F900 furnace for a YSZ specimen. (a) Thermal strain computed for DIC results with images of the two opposite faces of the specimen and its average value. A second-degree polynomial interpolates the thermal strain average to allow for the computation of the differential CTE. The gray patch shows the standard strain uncertainties. (b) Differential CTE α obtained from the DIC analyses of opposite sides of the specimen. The average of them is compared with literature results [94].

Observing the assessed thermal strain (Figure 4.6(a)) and CTE results (Figure 4.6(b)) illustrates the importance of obtaining data from both opposite sides of the sample to mitigate the effect of out-of-plane motions. This setup allows dilatometry tests to be performed for materials unsuitable for usual dilatometry setups (*e.g.,* with big aggregates in the composition), or to evaluate localized phenomena due to thermal loading.

4.1.5 EA-S, BR-D and YSZ-B optical dilatometries comparizon (F900) - MCS-EAB and MCS-EAYSZ constituents

To evaluate the CTE mismatch, attained for MCS-EAB and MCS-EAYSZ, the dilatometry results of these materials were compared. All the results used here were from dilatometry conducted in the F900, meaning that the out-of-plane displacement is compensated using the two-camera setup. The material constituents dilatometry results are presented in Figure 4.7. It is possible to observe that the mismatch of the proposed systems presents a positive value of $\Delta\alpha$ ($\alpha_I - \alpha_M$), which results in a radial crack pattern with temperature increase. Also, it is clear that the MCS-EAB would have a much more prominent mismatch compared to MCS-EAYSZ.

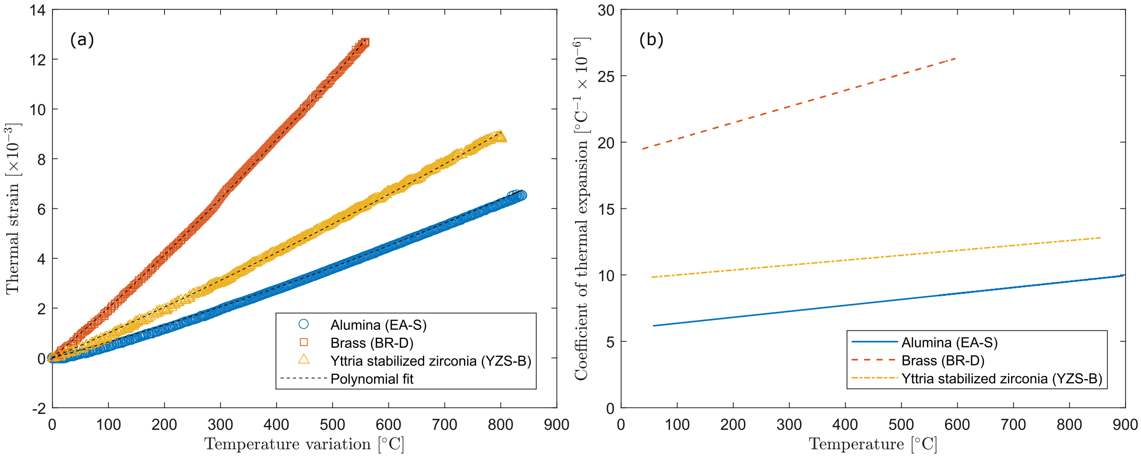

Figure 4.7: Dilatometry results of MCS-EAB and MCS-EAYZS constituents: (a) thermal strain; (b) tangent coefficient of thermal expansion.

The thermal expansion mismatch of the material systems are displayed in Figure 4.8. In this graph it can be observed that not only MCS-EAB has a higher system CTE mismatch, but also it is one that increases with temperature increase, while the MCS-EAYSZ CTE mismatch decreases with the increase in temperature.

4.2 Material mechanical characterization of the Model Composites phases

4.2.1 Elastic parameters' evaluation via Impulse Excitation Technique

Elastic parameters of some materials of interest for the model composite were evaluated using the impulse excitation technique. The equipment used for the

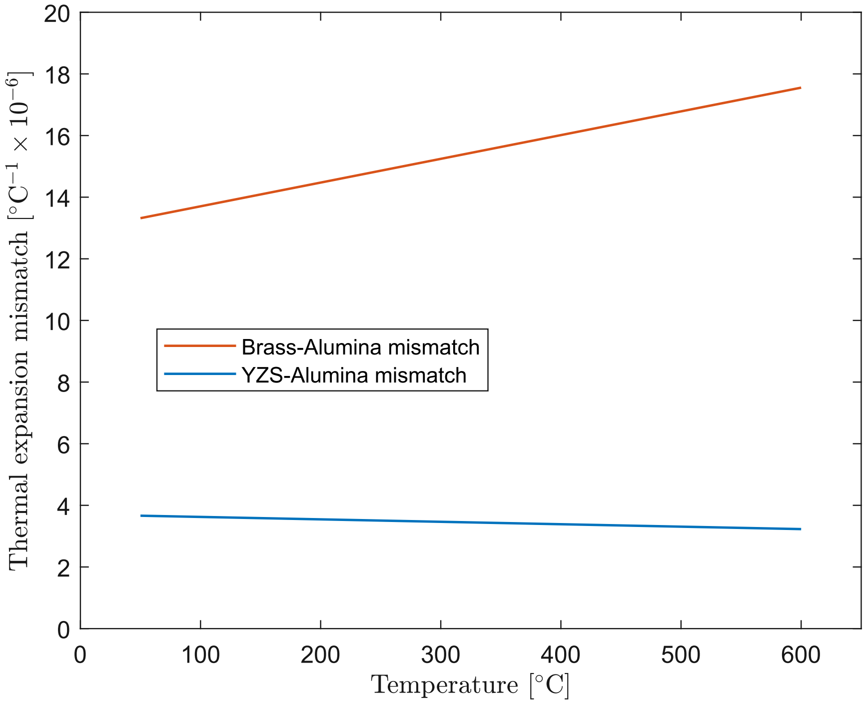

Figure 4.8: Thermal expansion mismatch of MCS-EAB and MCS-EAYSZ in function of temperature.

tests at room temperature was the RFDA MF system 23. This test analyzes resonant frequencies and their damping produced in a specimen when subjected to an impulse produced by an exciter. With the geometrical dimensions and the mass of the tested, elastic properties can be computed from the resonance frequencies obtained from the performance of a test. In Figure 4.9 it can be observed the equipment in use.

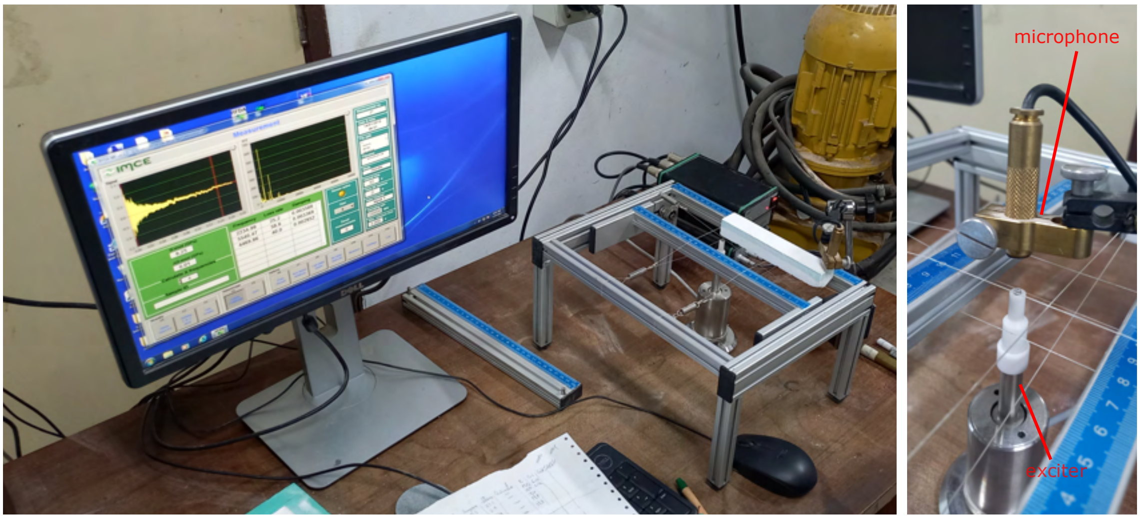

Figure 4.9: Impulse excitation test equipment.

Eight bars of alumina slurry were tested using this equipment in flexural and torsion modes, which provided the Young's modulus and Shear modulus for each specimen. From these values the Poisson's ratio was computed as:

$$\nu = \frac{E - 2\mu}{2\mu} \tag{4.4}$$

The evaluated properties for the bars and the mean properties values are presented in Table 4.1.

Table 4.1: Impulse excitation technique elastic parameters evaluation at room temperature of the electrofuse alumina slurry bars.

Specimen	Young's Modulus (GPa)	Shear Modulus (GPa)	Poisson (-)
EA-B1	14.7	6.2	0.18
EA-B2	14.8	6.0	0.23
EA-B3	14.5	6.1	0.19
EA-B4	14.7	5.9	0.24
EA-B5	13.8	5.6	0.23
EA-B6	14	5.5	0.26
EA-B7	14.7	5.9	0.24
EA-B8	13.9	5.6	0.23
Mean	14.4	5.9	0.22

Some specimens of candidate materials for the model composite inclusion were also tested only in flexural mode due to its circular cross-section geometry. The zirconia specimen used was the same one used in the dilatometry test. Despite its parallelepiped shape, the small dimension of the specimen made hard the evaluation of its Shear modulus, and therefore, this evaluation was not considered. The evaluated properties for the bars and the mean properties values are presented in Table 4.2.

Table 4.2: Impulse Excitation Technique Young's modulus evaluation at room temperature.

Specimen	Young's Modulus (GPa)	Shear Modulus (GPa)
Brass	83.8	29.4
Zirconia	164	

4.2.2 Elastic and fracture parameters' evaluation via three-point bending tests assisted by IDIC at room temperature

The elastic modulus and fracture stress of the three-point bending electro-fused alumina slurry specimens tested were evaluated via integrated Digital Image Correlation (IDIC) and analytical analysis. Regular DIC was also performed to observe the displacement and strain fields of the experiments. Three specimens were tested at room temperature (EA-B1, EA-B5 and EA-B7). A specific mesh was created for the DIC for each set of images of the experiments. To exemplify the meshes used, Figure 4.10 shows one of the faces correlations of the EA-B1 specimen.

Figure 4.10: Mesh used for the correlation of one of the EA-B1 specimen's faces.

The first test was conducted using specimen EA-B1. This test had the intention to be a pre-concept of the subsequent tests. The machine was controlled in displacement with a displacement ratio of 0.1 mm/min. The image acquisition was set to 1 image/10s to obtain 10 reference images with a pre-load for noise evaluation, and then 1 image/30s for the loading stage. The specimen failed with -195.3 N of applied load and in a short span of time, being possible to obtain only one image in the load stage as presented in Figure 4.11.

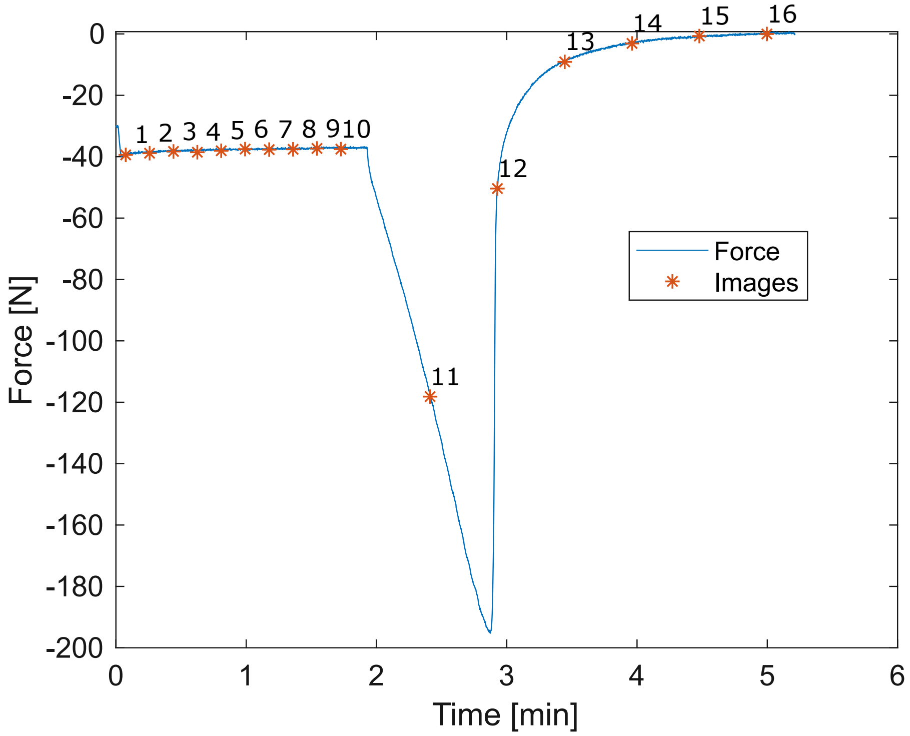

Figure 4.11: Three-point bending test force versus time in EA-B1 specimen. The asterisk shows the respective force of the images acquired of both specimen sides.

Despite not optimal, the young modulus of this specimen was evaluated via IDIC considering images 10 and 11. The analytical fracture stress (σ_f) of the specimens were computed according to:

$$\sigma_f = -\frac{F_c\, L_y\, h}{8\, I}\, ; \, I = \frac{w\, h^3}{12} \tag{4.5}$$

where F_c is the applied force before failure, L_y is the distance between the lower supports (127 mm), I the moment of inertia of the bar's cross-section, h the specimen's height, and w its width.

In the displacement results presented 1 pixel corresponds to 37.8 μm. The horizontal and vertical displacement of both specimen faces obtained via DIC can be observed in Figure 4.13. The material portrayed a pretty brittle behavior, however some crack growth could be observed, as presented in Figure 4.13.

For the next test, the specimen EA-B5 was used. From the experience attained of EA-B1, for this experiment the displacement rate was reduced to 0.01 mm/min

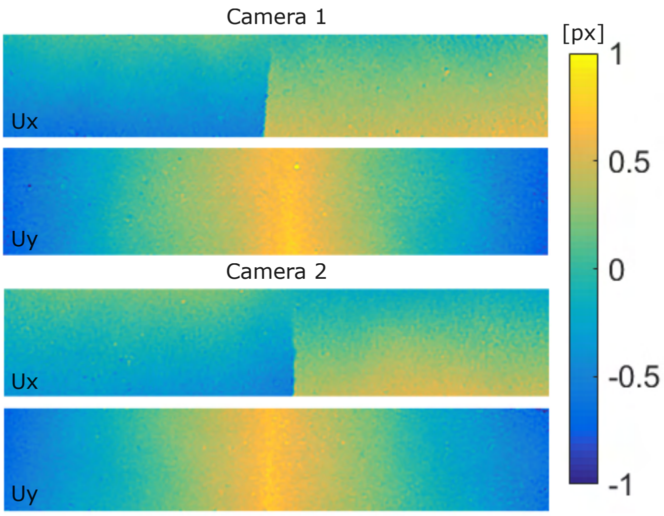

Figure 4.12: Horizontal (Ux) and Vertical (Uy) displacement fields of both faces EA-B1 of the image right after the specimen cracking.

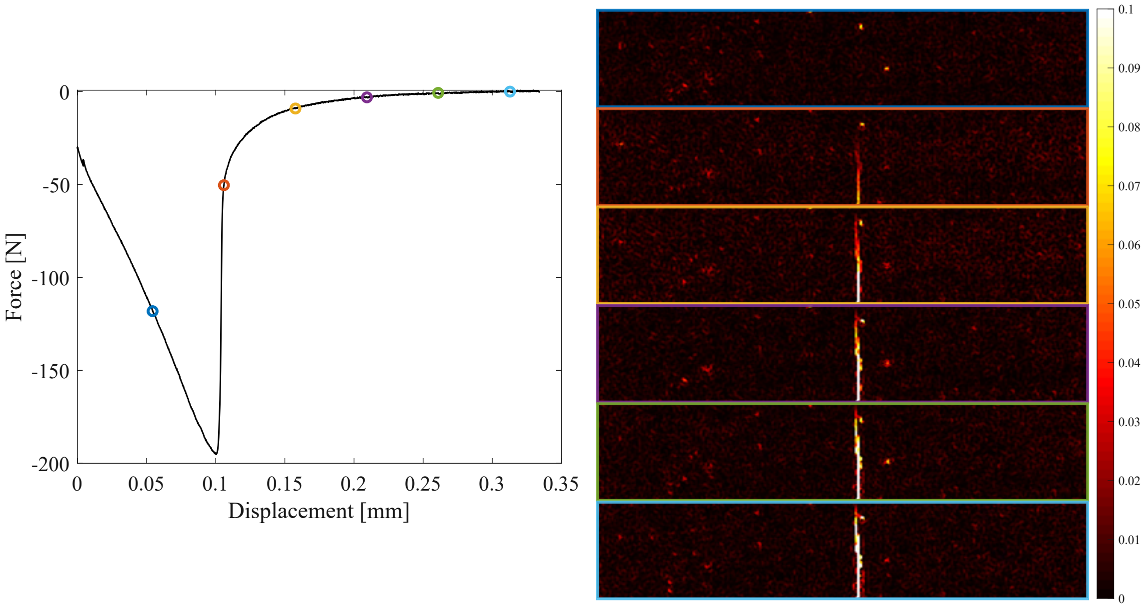

Figure 4.13: Maximum principal strain of camera 2 results to observe crack evolution on EA-B1.

and a new monotonic test was performed. The camera acquisition rate was maintained as described in the previous test. Figure 4.14 shows the force registered and images acquired during this test. In this experiment the failure of the bar was abrupt, therefore, there was no result of the specimen cracking.

The last test conducted at room temperature used the specimen EA-B7. The displacement ratio was maintained at 0.01 mm/min and a cyclic load test was performed. The camera acquisition rate was maintained as described for the

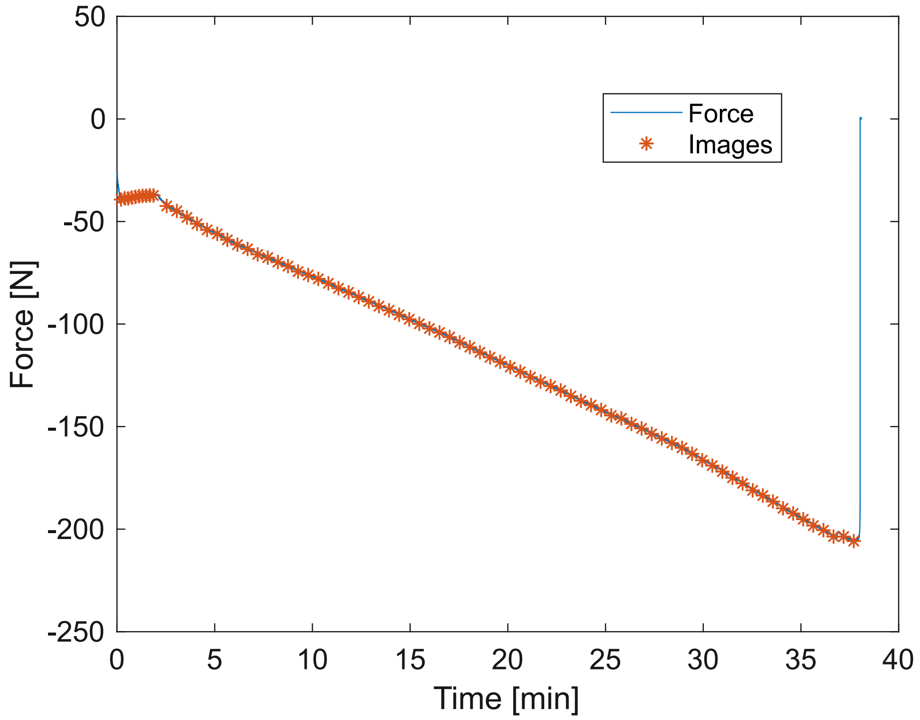

Figure 4.14: Three-point bending test force versus time in the EA-B5. The asterisk shows the respective force of the images acquired of both specimen sides.

previous test. Figure 4.15 shows the force registered and images acquired during this test.

Table 4.3 shows the parameters identified for the three-point bending tests conducted at room temperature. Despite the three different approaches executed, the results did not diverge much among the experiments and in relation to what had been observed in the IET tests. The table also presents the analytical evaluation of the fracture stress according to Equation 4.5. This calculation is brought for comparison with the values calculated via IDIC. The IDIC uses the same equation, however, it is sensible to the finite element mesh adjustment to the sample and conversion of dimensions from pixels to millimeters. Even so, the results attained were close to each other.

4.2.3 Elastic and fracture parameters' evaluation via three-point bending tests assisted by DIC at 300 °C

A three-point bending test was also conducted at 300 ℃. For comparison, the EA-B specimen was tested at room temperature without reaching the fracture stress and then tested after a temperature increase. The test was conducted with

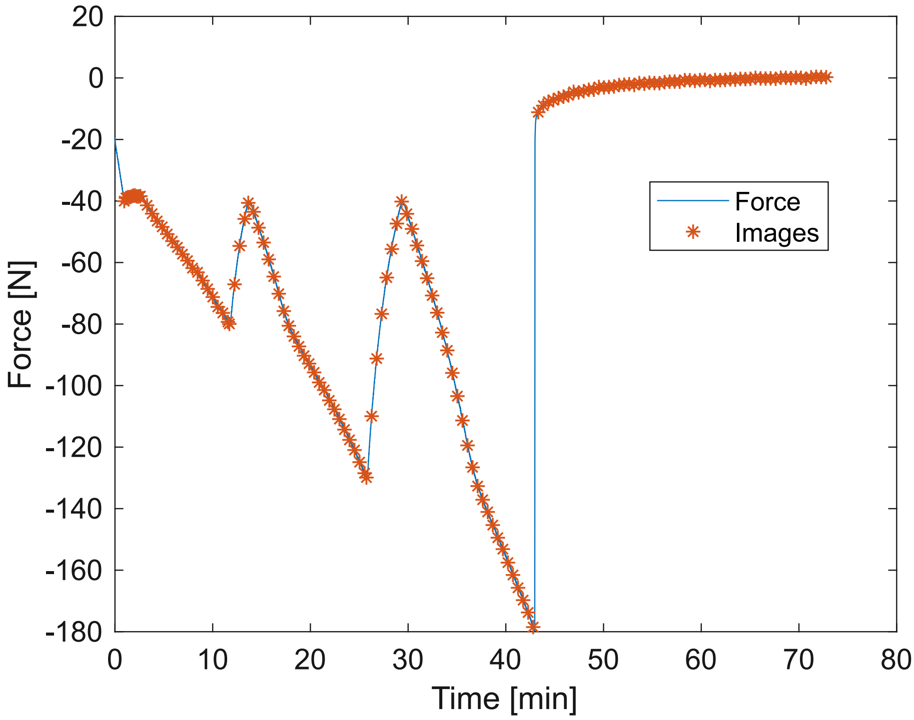

Figure 4.15: Three-point bending force versus time in EA-B7 specimen. The asterisk shows the respective force of the images acquired of both specimen's sides.

Table 4.3: Integrated DIC Elastic modulus evaluation at room temperature and fracture stress for electrofused alumina slurry bars (EA-B).

Specimen	Camera 1		Camera 2		Camera's average		Analytical
	E (GPa)	σ_f (MPa)	E (GPa)	σ_f (MPa)	E (GPa)	σ_f (MPa)	σ_f (MPa)
EA-B1	15.3	2.7	17.8	2.7	16.6	2.7	2.7
EA-B5	15.9	2.3	12.3	2.1	14.1	2.2	2.5
EA-B7	15.2	2	12.9	1.9	14	1.9	2.4
Average	-	-	-	-	14.9	2.3	2.5

the EA-B2 specimen. It was loaded for a pre-load of -30 N to -100 N at room. Then the furnace was heated to 300 ℃ and stayed at a plateau for 2 hours at this temperature for expansion stabilization of the specimen and machine parts. During the heating and plateau, a routine to compensate the expansion of the parts was used to keep the pre-load between -20 and -30 N. The loading was conducted after the 2 hour plateau, however, even then, the parts were still expanding, which can be observed in the load of the 10 reference images acquired looking at Figure 4.16 (b). This event resulted in an increase of the applied load during the acquisition of images that were supposed to be reference images.

Even though, the thermomecanical load induced over the specimen was adequate for the Elastic modulus estimation.

Because something inside the furnace vaporized over 300 ℃, the experiment had to be stopped. The routine that compensates for the expansion was stopped, and the specimen fractured. Therefore, no evaluation of the fracture stress could be made for this specimen. The results obtained are presented in Table 4.4.

Table 4.4: Integrated DIC Elastic modulus evaluation with temperature for electrofused alumina slurry bars (EA B).

Specimen	Camera 1	Camera 2	Average
	E (GPa)	E (GPa)	E (GPa)
EA-B2 (25℃)	16.4	14.2	15.3
EA-B2 (300℃)	14.3	14.9	14.6

4.3 MCS-CAB temperature variation experiments in F600

4.3.1 Experimental and numerical details of the analysis

In this analysis, it was used a triangular finite element mesh (T3) with an element edge of 30 pixels, being that 1 pixel corresponds to 17 μm. This mesh is constructed excluding the center hole from the inclusion and has a circular geometry to improve the radial displacement behavior of the matrix and inclusion. However, it is essential to clarify that the mesh does not extend to the boards of the sample, as can be seen in Figure 4.17.

A temperature variation of 250 $^{\circ}$C was performed in 250 minutes, with one photograph acquired per minute. The images were processed via DIC, and the displacement and strain fields were computed. Figure 4.18 presents the radial displacement evolution to four steps of the temperature variation of the model composite. The radial displacement field does not show apparent discontinuities, despite that radial cracks occurred after a temperature variation of circa 100 $^{\circ}$C. Additionally, the radial displacement field stays relatively symmetric along the tangential axis, which will corroborate with the equations used in the IDIC.

In order to observe the crack evolution in the model composite, the maximum principal strain displacement field is used. Figure 4.19 shows the maximum principal strain field to four steps of the model composite's temperature variation. As

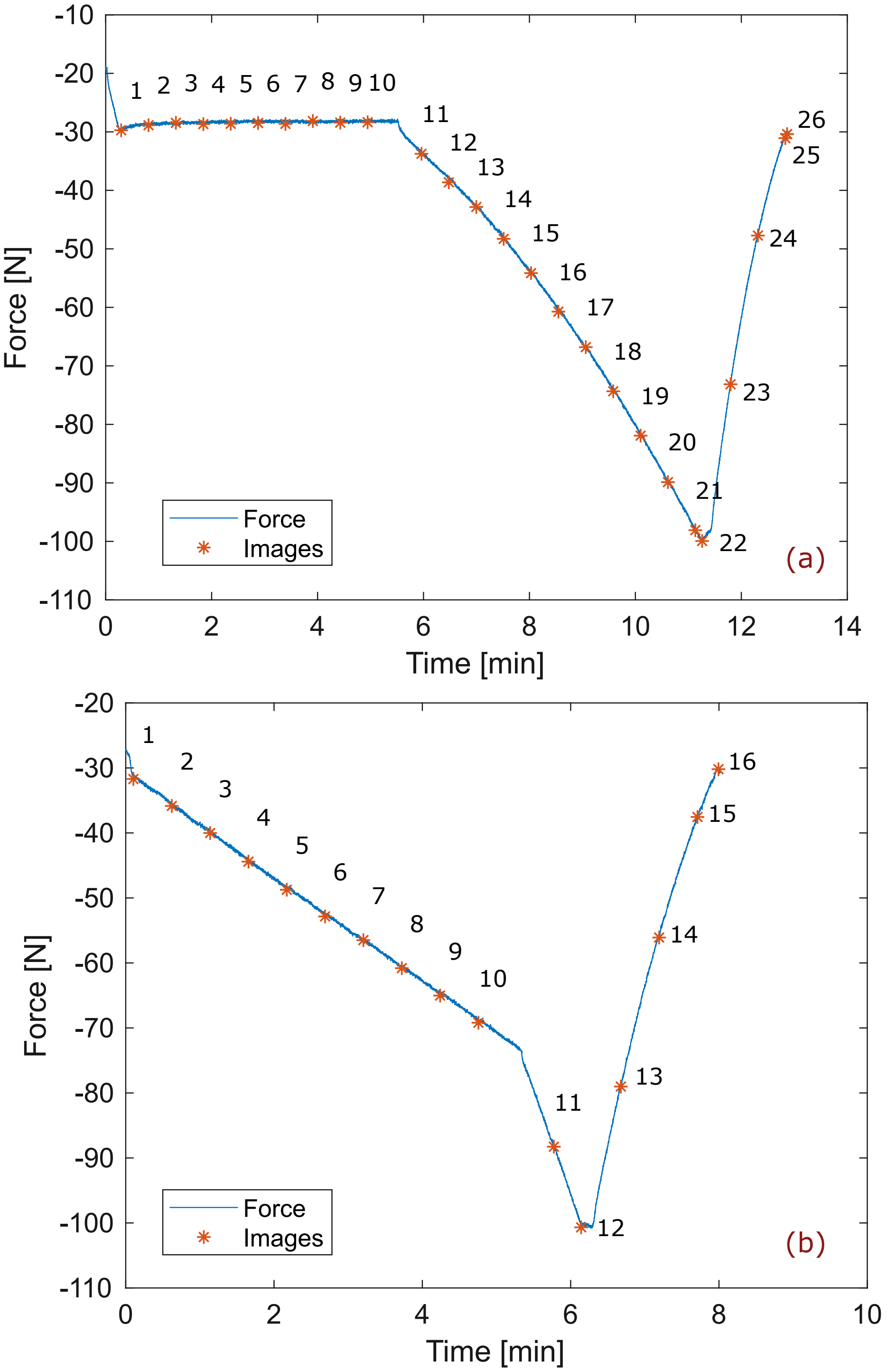

Figure 4.16: Three-point bending test force versus time in the EA-B2 specimen and images acquired of both specimen sides. The asterisk shows the respective force of the images acquired of both specimen's sides. (a) Room temperature test. (b) 300℃ test.

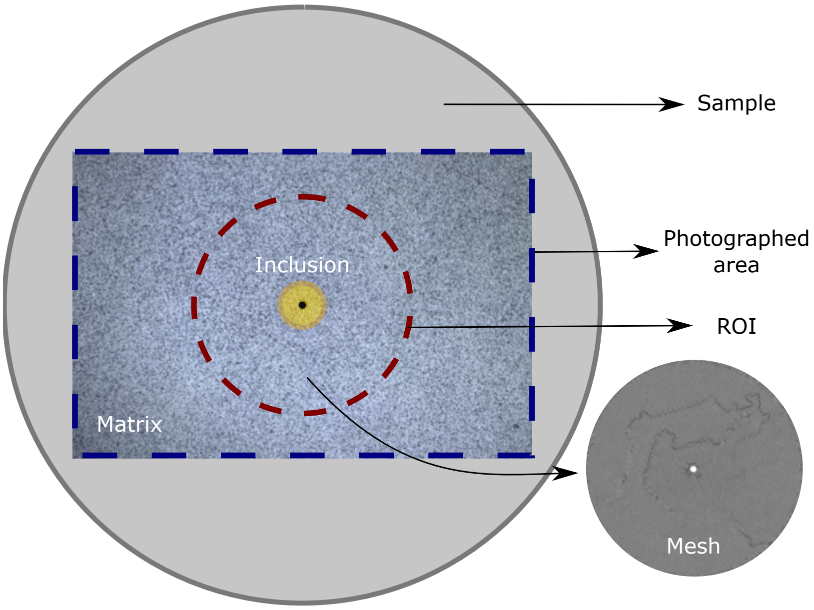

Figure 4.17: Illustrative representation of the Region Of Interest (ROI) analyzed.

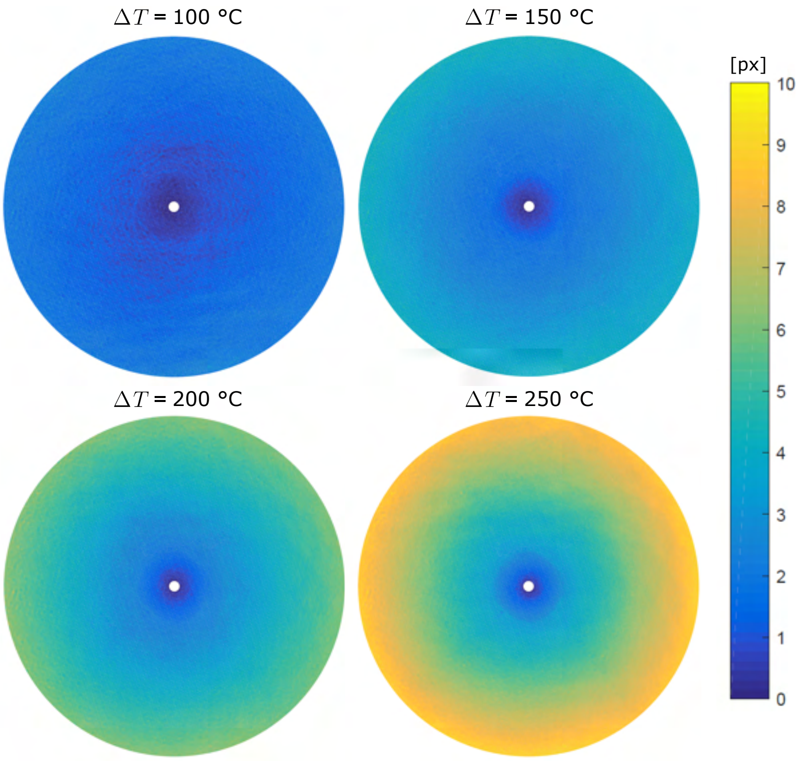

Figure 4.18: Radial displacement evolution obtained via DIC.

expected, radial cracks appear in the system as the CTE of the brass inclusion is higher than the one of the alumina slurry matrix.

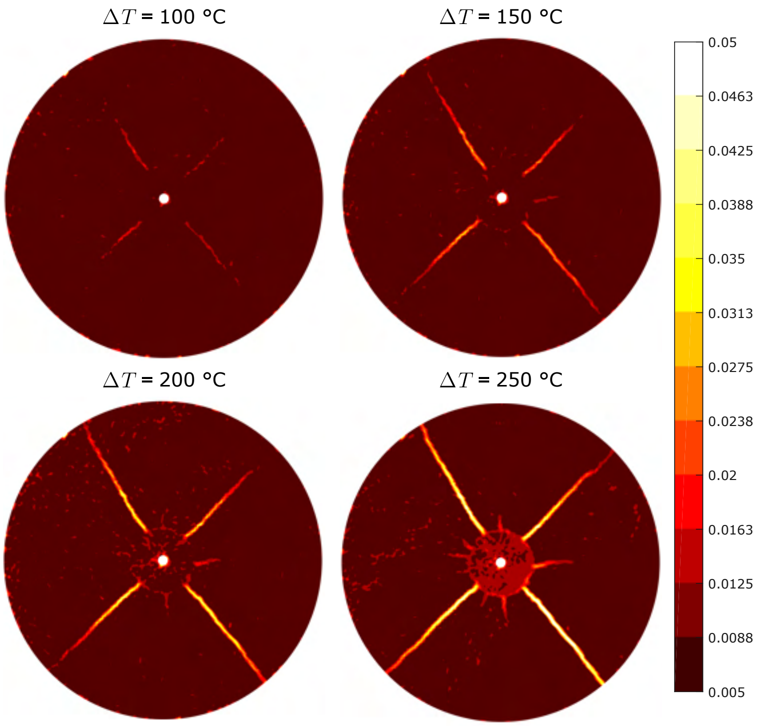

Figure 4.19: Maximum principal strain evolution obtained via DIC.

4.3.2 Full-field results and model fitting

The radial (u_r) and orthoradial (u_θ) displacement fields obtained from DIC analysis are shown in Figure 4.20. These fields are presented to 50, 150, and 250 °C of temperature variation. The 50 °C temperature variation snapshots show small values of displacement and no field discontinuities were found. For 150 °C of temperature variation, there is a clear difference in the radial displacement magnitudes for the inclusion and matrix, a visible radial gradient. Further, four major discontinuities (*i.e.* neighbor regions with extreme difference in the values of displacement) appear in the tangential displacement field, indicating the existence of cracks. At the maximum temperature variation (250 °C), the radial displacement increases and reaches 10 pixels (160 μm) of displacement in the ROI limits. The discontinuities presented in the tangential displacement field are intensified, and new ones appear almost in the bisector of the previous.

A more straightforward way to observe the system's cracking is the maximum principal strain field [65], as seen in Figure 4.21. In the temperature variation of 50 °C, there are no contrasting strain magnitudes, except for one region where a

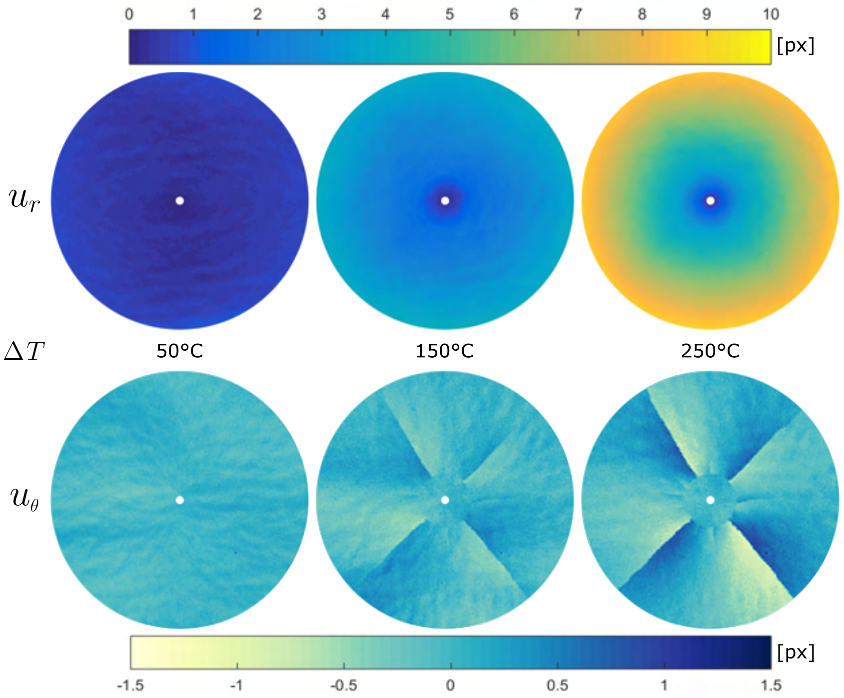

Figure 4.20: Evolution of the radial (u_r) and tangential (u_θ) displacement fields for temperature variations of 50, 150 and 250 °C. In this experiment 1 pixel of displacement corresponds to 16 μm [65].

pore appeared in the specimen surface in the southeast region during the experiment. At $\Delta T = 150$ °C, four prominent cracks forming an “X” pattern and minor cracks between each pair of major ones can be observed. With a temperature variation of 250 °C, the four initial cracks propagated to the borders of the ROI, and the minor cracks had grown and became visually evident, also, new minors appeared. It is essential to highlight that while the maximum principal strain field shows several cracks in the matrix, the radial displacement field (Figure 4.20) does not show relevant disturbances. This aspect allows the cylindrical single inclusion analytical model to fit the experimental radial displacement and identify the model parameters.

The experimental results were fitted to the analytical model for each temperature, as the radial displacement field in Figure 4.20 approximates an axisymmetric distribution. A parameter identification using a least-square fitting model was performed for the radial displacement experimental data in two steps. First, the parameter A_i is identified for the radial displacement of the inclusion domain according to equation 4.18. Then the parameter A_m is identified for the matrix do-

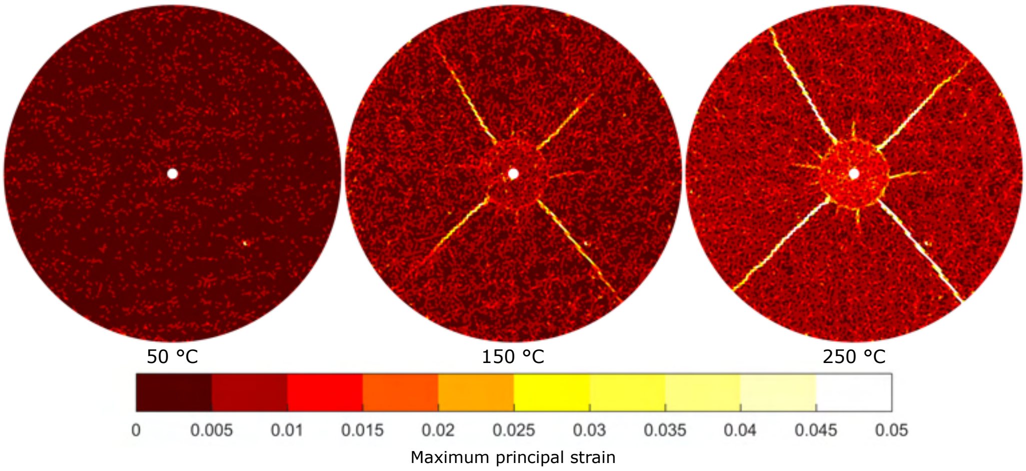

Figure 4.21: Evolution of the maximum principal strain field (ε_1) for temperature variations of 50, 150 and 250 °C [65].

main according to equation 4.18, replacing $\frac{B_m}{r}$ by $\frac{(A_i - A_m)r_i^2}{r}$, where A_m is imposed to be smaller than A_i. In Figure 4.22, it can be seen the experimental radial displacements for each mesh node versus its radius for $\Delta T = 50, 150$ and 250 °C as point clouds. The fitted parameters for the respective temperatures results in the continuous lines of radial displacement. The nodal displacements close to the inner and outer mesh edges were disregarded during the identification procedure, due to higher uncertainty in these nodes caused by the lack of gray values around these nodes.

The results show good agreement between the experimental data and the fitted model, considering that the fitted model remains inside the cloud of points. However, some issues interfere with a better adjustment of the model to the data. One of these issues is the out-of-plane displacement caused by the expansion of the sample holder supporting rods, which produces a parasite expansion in the results. Also, the analytical model does not consider discontinuities in the medium as the appearance of cracks. At last, heat waves in the oven atmosphere create optical distortions that also contribute to oscillations.

To verify the feasibility of the model fitting, a comparison between the alumina slurry thermal strain obtained in the dilatometry experiment and the Am parameter (equation 2.69) identified in the model fitting of the MCS temperature variation experiment is presented in Figure 4.23. The two data showed good agreement,

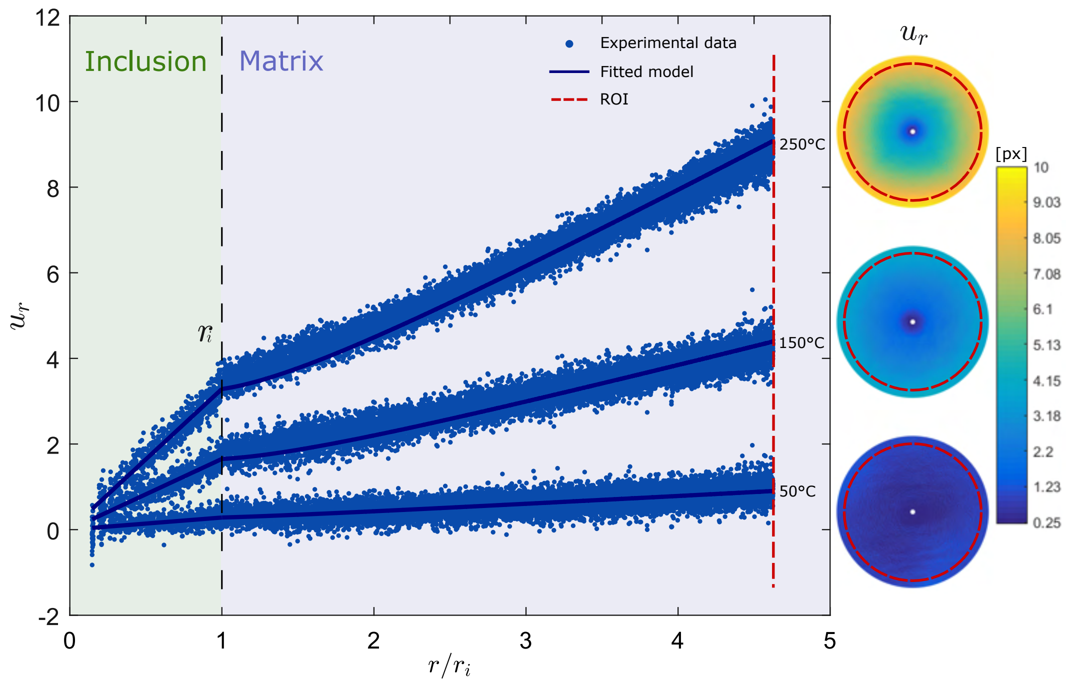

Figure 4.22: Radial displacement for three temperature variations, where r/r_i is the radial distance from the center of the inclusion divided by the inclusion's radius. In the right are displayed the radial displacement fields correspondent to each temperature variation. The analytical model presented is used to fit the experimental data [65].

corroborating to ensure the viability of using the analytical model to adjust the experimental data.

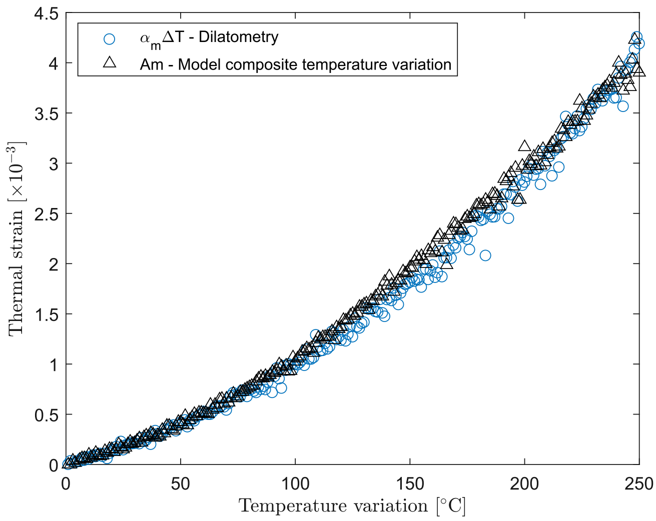

Figure 4.23: Comparison of $\alpha_M \Delta T$ obtained in the optical dilatometry test and in the analytical model fitting of the MCS temperature variation test ($A_m = \alpha_M \Delta T$) [65].

4.3.3 Evaluation of crack initiation as a function of ΔT

An elastic and thermal displacement field was obtained using the parameters discussed in Chapter 2. These displacement fields attained were derived, and the maximum principal strain computed containing only thermal and elastic components, without the influence of cracks. This field, is then subtracted from the experimental strain field, obtained directly from DIC, resulting in a field of inelastic maximum principal strain. Figure 4.24 shows the strain fields described. For the new obtained inelastic strain field, a threshold (ε^*) can be defined to quantify the cracking of the system. Several works made use of a threshold strategy, using typically a value 5 times or more the standard uncertainty of measurements [95]. It can be seen threshold values of ε^* in the order of $0.6 - 1.5 \times 10^{-3}$ (*i.e.*, between 1.5 and 3 times their uncertainty level) being used in the literature to define cracks [95–97], with meshes of similar element size as used herein. However, such works were conducted with no temperature variation and in temperatures up to 70°C, in contrast with the 300°C achieved in the MCS temperature variation experiment. For the discussion hereafter, the ε^* for the MCS experiment is defined as 0.01, ten times the noise measured for the reference images (0.001). This value was selected because it did not mask the beginning of the cracking process and also did not allow noisy regions to be defined as cracks in the final results of the analysis.

An evaluation of the crack initiation was performed by observing a region around the inclusion in the matrix domain to compute the percentage of elements considered as cracked (inelastic maximum principal strain $\geq$ 0.01) for each temperature. A temperature variation of 58°C (T = 98°C) was observed to be the critical temperature variation where the cracking of the system initiates according to the threshold defined. The MCS was intended to produce radial cracks propagating from the interface of the inclusion and matrix, which proved successful. Figure 4.25 brings the percentage of elements considered cracked for each temperature.

It is also possible to evaluate the crack opening and crack propagation by computing the Average Mean Crack Opening Displacement (Average MCOD) and

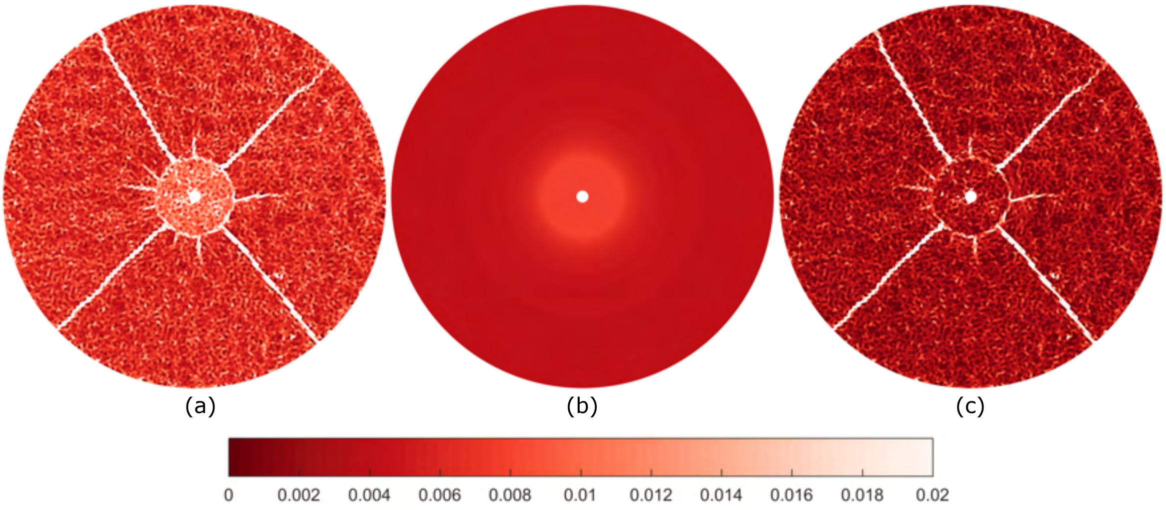

Figure 4.24: Post-processing to obtain an inelastic maximum principal strain field for a temperature variation of 250°C: (a) total maximum principal strain field obtained from the DIC; (b) elastic and thermal components of the maximum principal strain field obtained fitting the analytical model to the experimental results; (c) inelastic maximum principal strain field resultant of the subtraction of the thermal and elastic parcel from the total maximum principal strain field [(a) - (b)] [65].

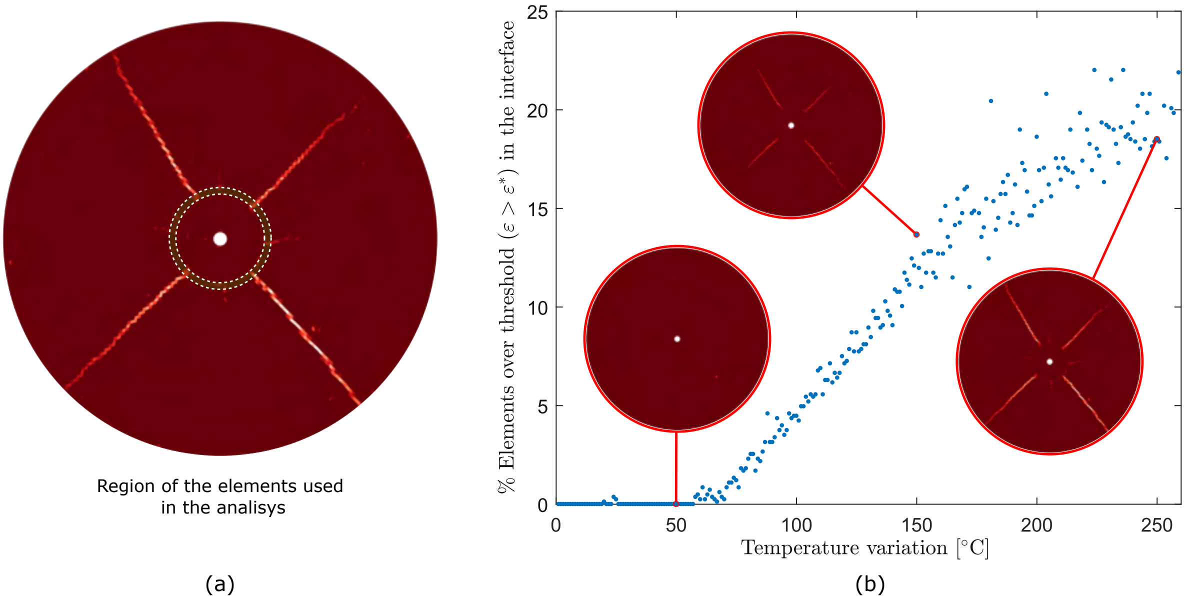

Figure 4.25: Analysis to evaluate the crack initiation in the model composite: (a) region containing the elements near the interface used to verify crack initiation; (b) percentage of elements surpassing the crack threshold of 0.01 for maximum principal strain for different temperature variations in a range between r_i and $r = 500$ pixels. In detail, the inelastic maximum principal strain field for the temperature variations of 50, 150 and 250 °C [65].

the Surface Crack Density (SCD), respectively, during the temperature variation [98, 99]. The Average MCOD is computed as the mean of the maximum principal strain of the elements above the threshold value multiplied by its respective characteristic size, *i.e.* the square root of the element area. The SCD is the fraction of a given area considered cracked over the area of all elements in the region analyzed. Figure 4.26 illustrates these parameters computation to evaluate the cracking of a ROI.

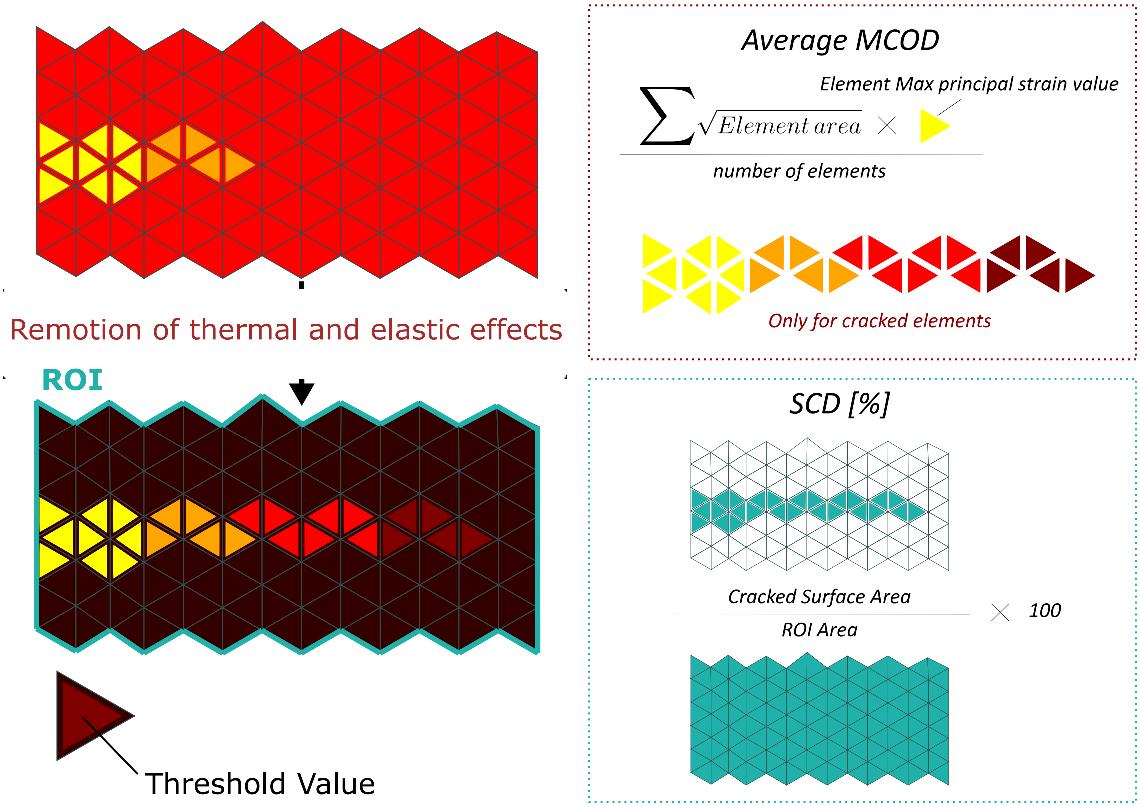

Figure 4.26: The Average MCOD and SCD [%] parameters representation. With the maximum principal strain field computed from an inelastic parcel of the strains, a threshold value defines the cracked elements. Knowing the cracked elements, the parameters can be computed according to the description inside the representation inside the dotted squares.

In Figure 4.27, eight crack sub-regions were analyzed. They are slices of ten degrees in angle containing a max radius of 1800 pixels to avoid the results near the mesh edge. The major cracks are denoted by “×" markers, while the minor cracks by “+" markers.

The SCD results showed that the major cracks increase their propagation rate at $\Delta T \approx 75°C$ and there is a tendency to reach a plateau. For the minor cracks, there is a propagation onset at $\Delta T \approx 125°C$ and a plateau is reached at $\Delta T \approx 175°C$. This indicates that the initial cracks are protagonists of the cracking process from the beginning until the end of the test, and the appearance of

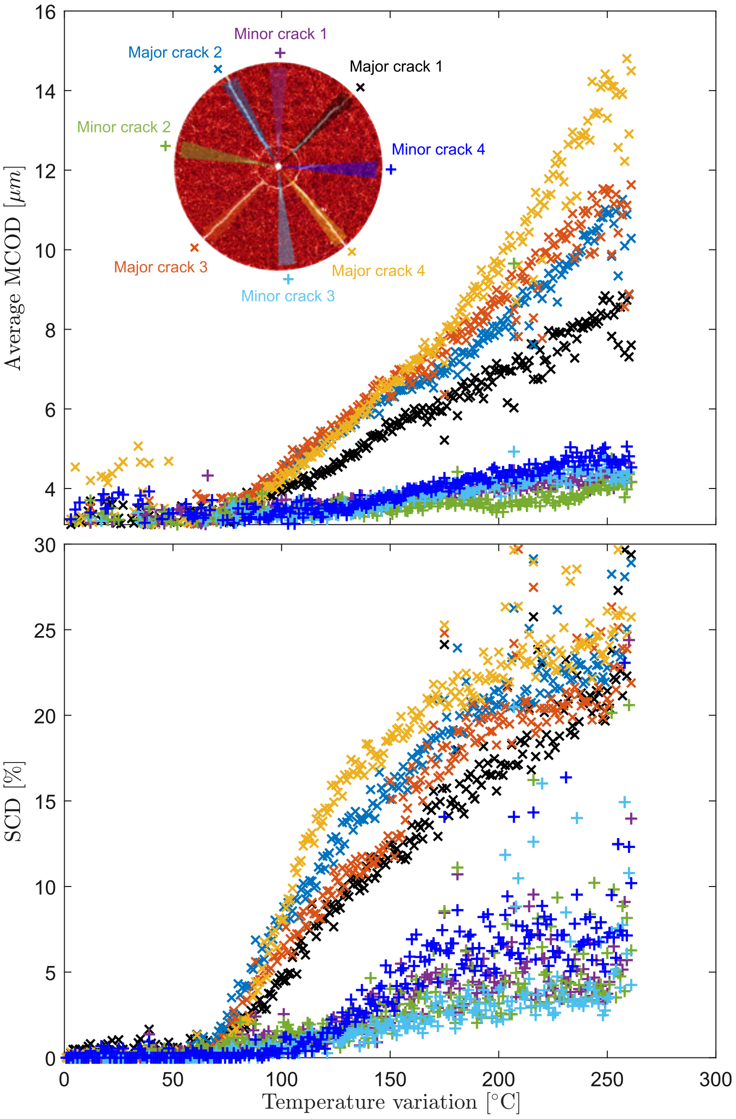

Figure 4.27: Average MCOD [μm] and SCD [%] as function of temperature variation for eight equal size regions containing a single crack [65].

new ones (a.k.a. minor cracks) does not stop their propagation. It is worth noting that the increase in the oscillation of SCD values for higher ΔT is due to experimental issues such as heat waves. Major cracks also showed average MCOD values and an increasing rate greater than the minor cracks, corroborating the assumption that the onset of minor cracks does not reduce the propagation of major ones.

4.4 MCS-CAB IDIC implementation and results

As described, an analytical model has been developed to describe the radial displacement behavior for a cylindrical inclusion inside an infinite matrix, where two constants can define the solution for the radial displacement as a function of the radius (r), i.e.:

$$u_r = Ar + \frac{B}{r} \tag{4.6}$$

The problem has two domains, the matrix domain and the inclusion domain, and the radial origin of the analytical description is the center of the inclusion. In order to apply a kinematic model to the response of the model composite, it is assumed a plane stress condition due to the sample geometry. Then, evaluating the equations, the total system analytical radial displacement can be described by three parameters - A_i, A_m and B_m - once, for the considerations adopted $B_i = 0$.

In this analytical model used to furnish the system's kinematics, the parameter A_i is responsible for the radial displacement of the inclusion, giving a linear radial displacement in the inclusion domain. The parameter A_m states the radial displacement of the matrix. Furthermore, the parameter B_m defines a transition close to the interface, which depends on the inclusion radius (r_i).

The identification procedure comes to:

$$\mathcal{F}(\mathbf{x}) = \int_{\Omega} [g(\mathbf{x}) - f(\mathbf{x} + \mathbf{u}(\mathbf{p}))]^2 d\mathbf{x} \tag{4.7}$$

where $\mathbf{p}$ is a vector that contains A_i, A_m and B_m. For further depth in the analytical model.

Therefore, the implementation of the IDIC for MCS-CAB temperature variation experiment consists in identifying three parameters that give the model radial displacement. By this process, the number of degrees of freedom drops drastically, reducing the computational cost of processing and the memory needed to store the results. In Figure 4.28 it can be seen the radial displacement results for the DIC, the IDIC, and the difference between the results. As observed, the results obtained agree with the models proposal, diverging mostly by some image distortions that will be discussed opportunely.

By observing Figure 4.28 some assumptions can be made about the possible causes of the displacement fields difference. The first hypothesis lies in the image distortions caused by heat waves, an aspect that is pretty apparent in some DIC

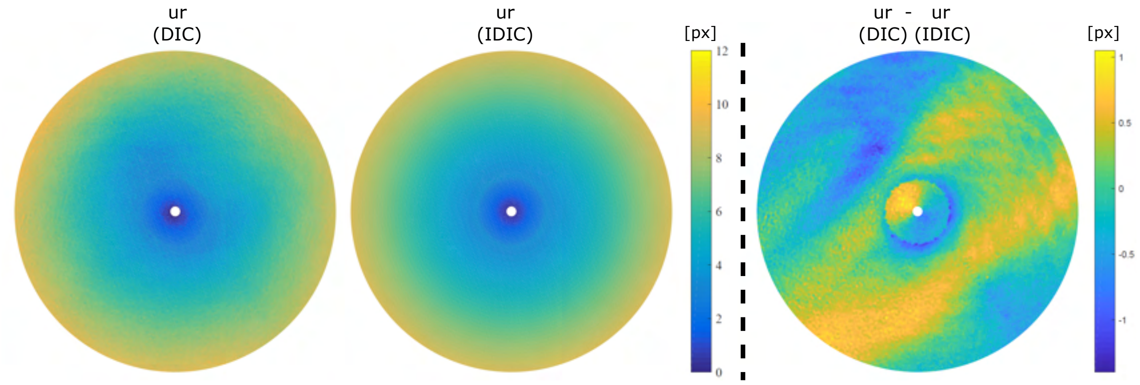

Figure 4.28: From the left to right it is presented the radial displacement obtained via DIC, the radial displacement obtained via IDIC and the difference between these displacement fields identified for a temperature variation of 250 °C.

results and that is well described in the literature [100, 101]. In general, it is expected that such a phenomenon is less influential in the IDIC, resulting in a difference between the fields. The other aspect that shows off is the interface between the inclusion and the matrix. There are two possible explanations for this difference. The first is because the mesh used may have elements over the interface, so the radial displacement should not be described strictly by the inclusion or matrix parameters in the IDIC, but it probably happens. Moreover, it is established in the IDIC a fixed value for the matrix/inclusion interface (r_i), being that the value of r_i certainly increases during the temperature increase.

4.5 MCS-EAB temperature variation experiments in F900

4.5.1 Experimental and numerical details of the analysis

MCS-EAB and MCS-CAB are quite similar, differentiating only by the type of alumina used for the matrix and the absence of a hole in the inclusion. The use of this material combination ensures the obtaining of cracks in the system due to temperature variation supported by the MCS-CAB experiments. The purpose of MCS-EAB experiments was to obtain data from both opposite sides of the specimen to observe if there would be differences in the crack nucleation and propagation between these sides, being able to quantify the actual cracked surface in the ROI. The MCS-EAB experiments were conducted in the F900. Also, MCS-EAB was tested with 1, 2 and 3 inclusions to observe the effects of the number of inclusions's influence on the crack initiation, propagation, and pattern.

For these experiments commercial ink spray for high temperature was used. The experiments were conducted up to 600 °C, however, a good texture was maintained only until around 400 °C, when the ink began to deteriorate. Nevertheless, the MCSs were already cracked until this point, which allowed to study the results attained.

4.6 Cracking pattern for MCS-EAB system with different number of inclusions

By observing the cracking of the systems via the maximum principal strain component (ε_1), it could be noticed that the inclusions number affects the crack density in the ROI as showed in Figure 4.29. Also, for these systems with a predominance of radial cracks with multiple inclusions, the cracking tends to connect the inclusions. These results highlight the need to evaluate the system cracking considering both sides of the specimen, once, in the experiments, both sides do not initiated the cracking process simultaneously, nor end up with the same surface crack density.

In all model composites, several cracks have nucleated. However, it is clear that the systems with multiple inclusions tend to have some predictable crack paths interconnecting the inclusions. These systems also presented evident circumferential cracks connecting radial ones.

Also when comparing the faces crack initiation and pattern of each MCS-EAB specimen, they all present a dominant face, *i.e.,* a face that has a more prominent crack pattern, that hints the crack path that will arise in the other face. For the one and three inclusions, the camera 2 results are the dominant side, while for the two inclusions, experiment camera 1 results present the dominant side.

4.6.1 FE models to obtain thermo-elastic response of the MCSs

As presented, the analytical model introduced was used to evaluate and remove the thermal and elastic strain components of the DIC results, allowing the evaluation of the crack initiation and propagation for MCS-CAB. For a multiple inclusion experiment, analytical models become more complex once each inclusion exerts an influence on all points of the domain. The analytical solution for a

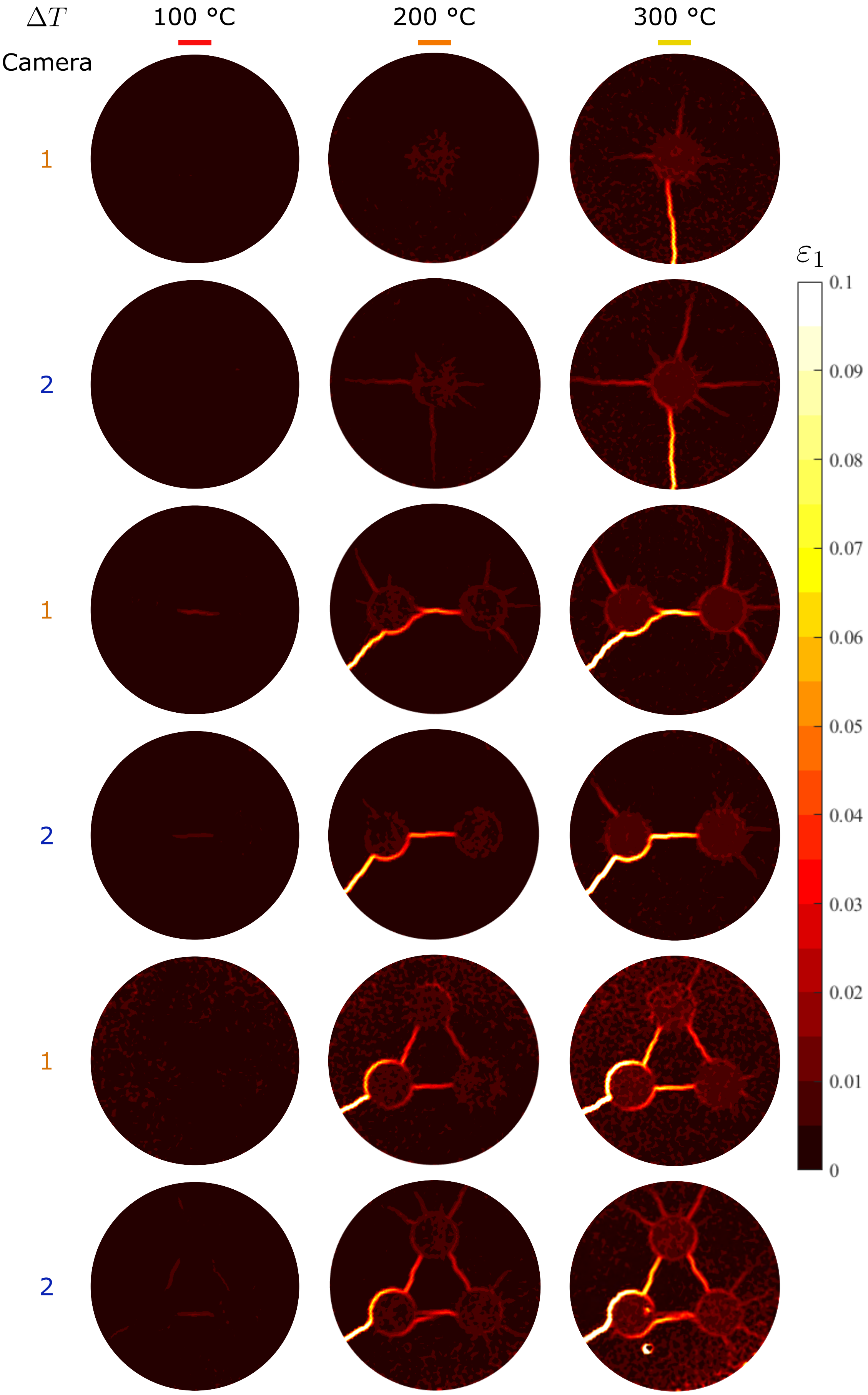

Figure 4.29: Cracking resultant of temperature variation observed via maximum principal strain for MCS-EAB with 1, 2 and 3 inclusions. The results of each experiment are presented for both faces of the MCS-EAB specimens.

case with multiple inclusions exists and can be obtained from the Muskhelishvili complex potentials [102]. One way to roughly evaluate the effects of a system with multiple inclusions is by superimposing the previously described solutions, as done by Zago [64].

Another way to approach the evaluation of thermo-elastic strain of case studies is using Finite Element (FE) models. For the present study, FE models were created based on the images acquired of the MCSs and fed with the material properties identified and the experimental boundary conditions to obtain thermo-elastic strain fields to be subtracted from the DIC results. The FE models were developed in the software Abaqus^{TM}. The same meshes created in the FE software were then used for the DIC analysis. The properties used in the FE simulations are presented in Table 4.5, and they were obtained from the mechanical tests and the optical dilatometries. The mechanical properties were held constant, while the thermal expansion was considered temperature-dependent.

Table 4.5: Material properties used in the FE simulations.

Material	Young's Modulus (GPa)	Poissons' ratio (-)	CTE ($\times 10^{-6}$ °C^{-1}) (25-450 °C)
Alumina	14.5	0.22	5.64 - 7.96
Brass	80	0.3	20 - 23.9

The model geometry and boundary conditions developed to obtain results for one of the faces of the three inclusion model composite are presented in Figure 4.30, where the model is restrained in translation and rotation, but is free to expand. All the regions are put under a temperature of 25 °C in the initial step and then, the model arises the temperature in 1 °C per increment up to a temperature of 325 °C.

The element used is a standard plane stress triangular element with linear geometric order and a size of 30 pixels. Some domains were created for the results' extraction of a region of interest. the region of interest was the matrix domain, where there was good visualization in the real images that would be used to obtain DIC results.

Five FE models were created in total. For the single inclusion MSC2, a single

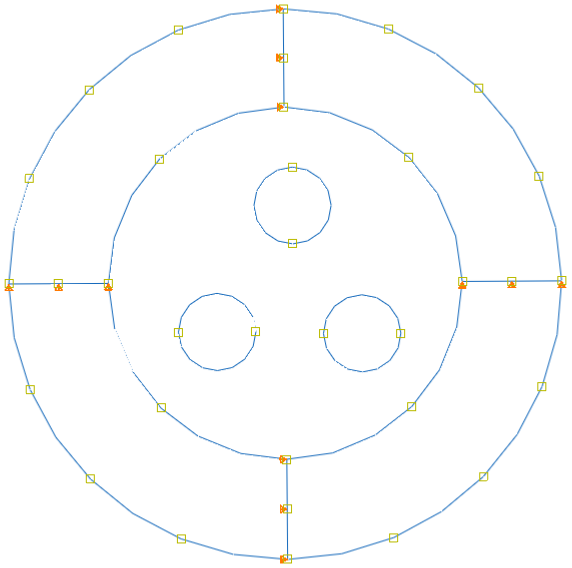

Figure 4.30: Displacement/Rotation boundary conditions imposed to the model, where all regions are subjected to a tempera increase via a predefined field.

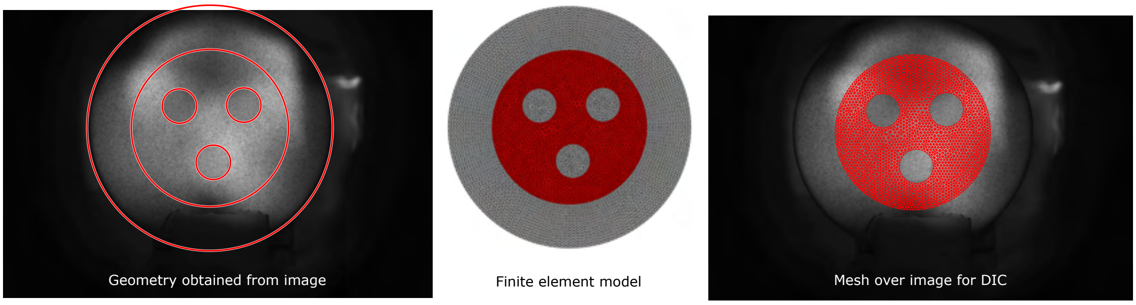

Figure 4.31: FE model created from geometry based on image and usage of FE mesh for correlation.

FE model was used, once it was easy to apply the FE model results to each side of the DIC results. For the multiple inclusion experiments, a FE model was created for each side of the specimens' results. The models were created in pixels with the full dimensions of the real specimens, 1250 px in radio. A partition with 800 px in radio was created for the results' extraction, which was the ROI used in the correlations. To illustrate the procedure described, Figure 4.31 was produced for one of the faces of the three inclusions MCS-EAB. Due to the same setup procedure in all experiments and the same manufacture process of all specimens, the inclusion radius in all models had a dimension of 175 px. The region of interest in the analysis excludes the inclusions, once no cracks occur in them. The strain fields of the FE models were subtracted from the DIC respective fields.

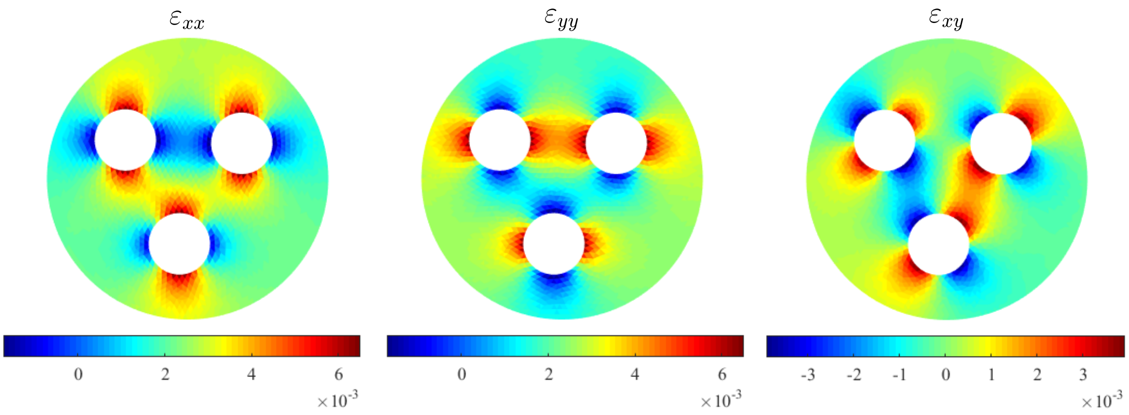

Figure 4.32: FE strain fields computed in Abaqus^{TM} for one of the faces of the three inclusion MCS-EAB at 300°C of temperature variation.

One of the sides of the three inclusions MCS-EAB FE strain fields at 300 °C is presented in Figure 4.32. The subtraction of the FE models from the DIC results produces strain fields mainly resultant of inelastic effects. Maximum principal strain fields were then computed from these fields to evaluate the crack initiation and propagation for each of the specimens' faces.

It is hard to compare the thermo-elastic strain results of the DIC with the FE models once cracking occurs in relatively small ranges of strain in the MCS-EAB, however, this comparison is interesting to demonstrate the well evaluation of properties input into the numerical models. Therefore, a comparison between DIC results and numerical model for a single inclusion MCS-EAB is presented, once this system had a larger temperature range before cracking. Even though the comparison of the results presented is for a temperature variation of 50 °C to ensure that no damage was inflicted to the specimen. This comparison is presented in Figure 4.33.

As an afterthought, it is worth to elucidate that the vertical image axis is positive downward, while the Cartesian vertical axis is positive upward. That is why the correlation results seem to be flipped in regard to the images and numerical models.

4.6.2 Cracking initiation and propagation in MCS-EAB specimens

The first step to evaluate the cracking in the results was to remove the thermo-elastic strain from the DIC results using the FE fields. As described, the xx, yy,

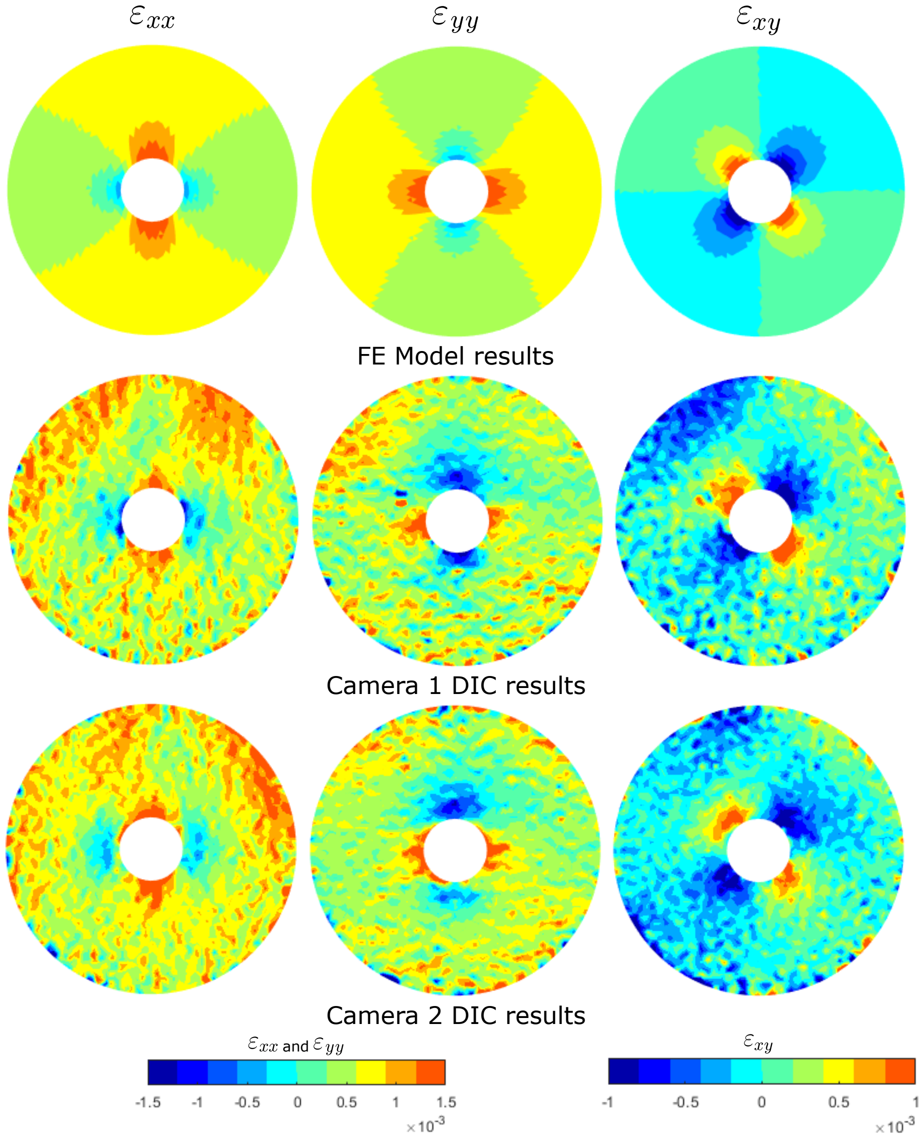

Figure 4.33: Comparison between the FE and experimental strain fields for a temperature variation of 50 °C.

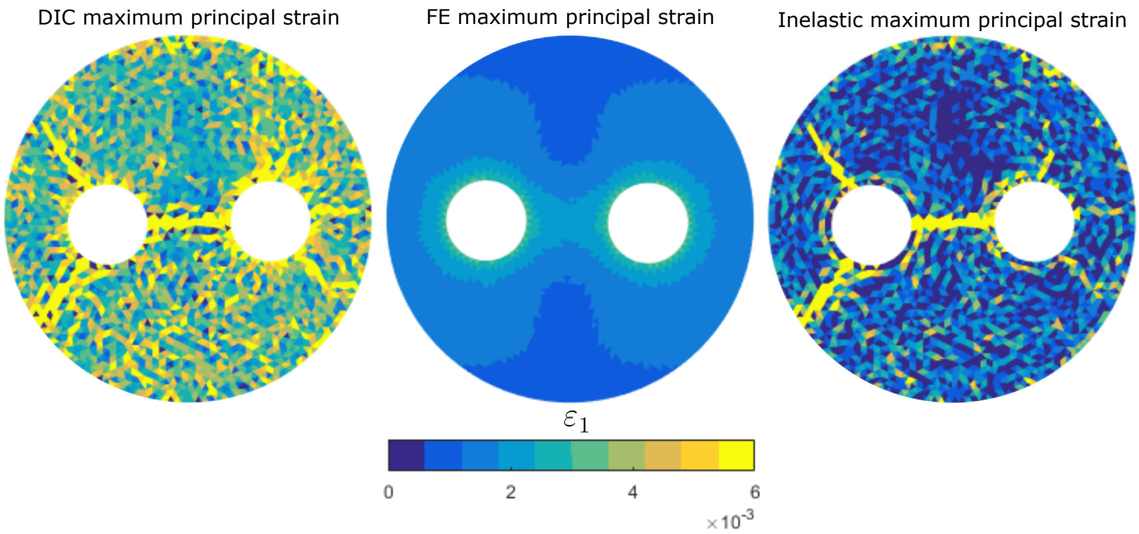

Figure 4.34: Maximum principal strain for a temperature variation of 300 °C, from left to right: Maximum principal strain field with thermo-elastic effects obtained directly from DIC; maximum principal strain obtained from FE simulation containing only thermo-elastic effects; Inelastic maximum principal strain computed from the subtraction of the FE model xx, yy and xy components from the DIC results.

and xy respected fields are subtracted and then an inelastic maximum principal strain is computed. Just as a matter of illustration, Figure 4.34 was produced illustrating the DIC result maximum principal strain field, the FE maximum principal strain field and the inelastic maximum principal strain field resultant of the strain component field for one of the faces of the two inclusions MCS-EAB specimen for a temperature variation of 300 °C.

Once the inelastic maximum principal strain field was obtained for all MCS-EAB results, the crack initiation and propagation were evaluated via the SCD and MCOD approach. For the evaluation of such parameters, a threshold value must be adopted. It was noted however that the noise of correlation for each DIC performed was different for each set of reference images, also, the noise increase also was particular for each correlation. Therefore, in order to present a better representation of the cracking behavior of all the specimens' faces, the threshold value was evaluated as ten times the residual of the images from 290 to 310 °C when all the specimens were already damaged. Although there was temperature variation among these “reference images", the thermal effects had already been subtracted. Table 4.6 shows the noise evaluated for the reference

Table 4.6: Noise evaluated for the MCS-EAB DIC results for two different temperature set of images.

	one inclusion		two inclusions		three inclusions	
Temperature	Camera 1	Camera 2	Camera 1	Camera 2	Camera 1	Camera 2
25℃	0.00033	0.00027	0.00029	0.00022	0.00049	0.00059
290-310℃	0.00065	0.00075	0.00075	0.0006	0.00122	0.00113

images at 25 °C and around 300 °C. Figure 4.35 shows the SCD and MCOD results.

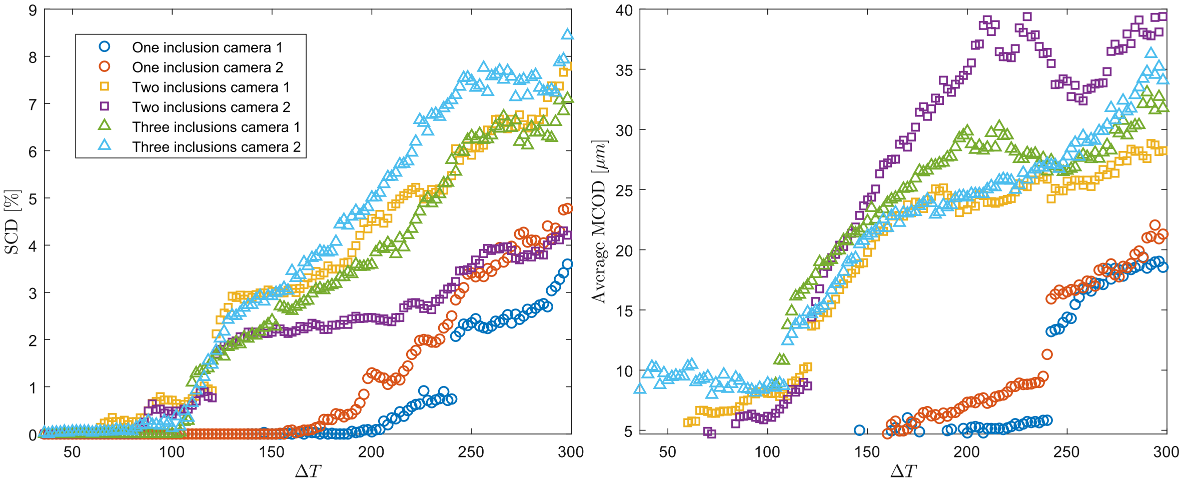

Figure 4.35: SCD and MCOD of all MCS-EAB results.

4.6.3 Evaluation of the inclusion diameter on the cracking of MCS-EAB

Davidge and Green [17], showed that there is a critical inclusion size for a material system to crack at a given temperature variation. Therefore, different inclusions' diameter were tested in MCS-EAB to evaluate the response of the specimens. Figure 4.36 shows the inclusions used in this test. An inclusion with ∅ 4.7 mm and one with ∅ 8.1 mm were tested. The specimens were texturized and submitted to a temperature variation and image acquisition similar to the 12.7 mm diameter single inclusion MCS-EAB specimen.

The ∅ 12.7 mm MCS-EAB results are the ones presented in the previous section, where prominent cracks could be seen in both sides of the specimen, being that there was a “dominant" side.

The ∅ 8.1 mm MCS-EAB was tested up to 600 °C and cracked during the experiment, however the cracking was lesser intense, as shown the results dis-

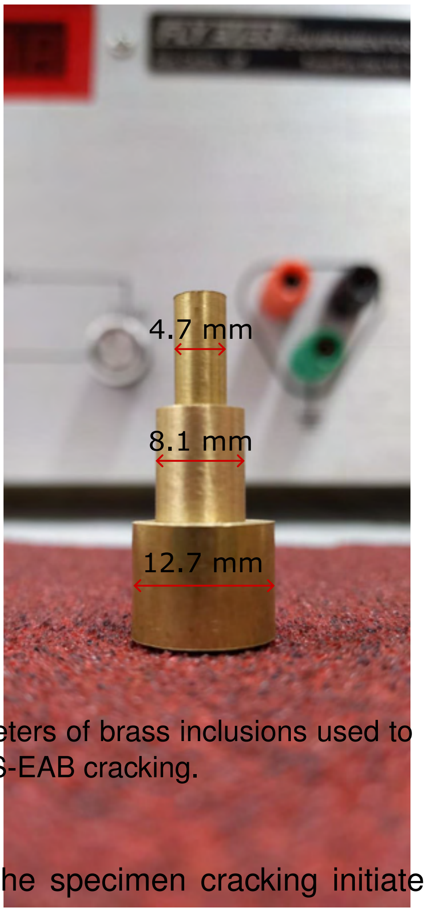

Figure 4.36: Different diameters of brass inclusions used to investigate the influence of the inclusion size in the MCS-EAB cracking.

played in Figure 4.37. The specimen cracking initiated around 150 °C in the dominant side and 200 °C in the other.

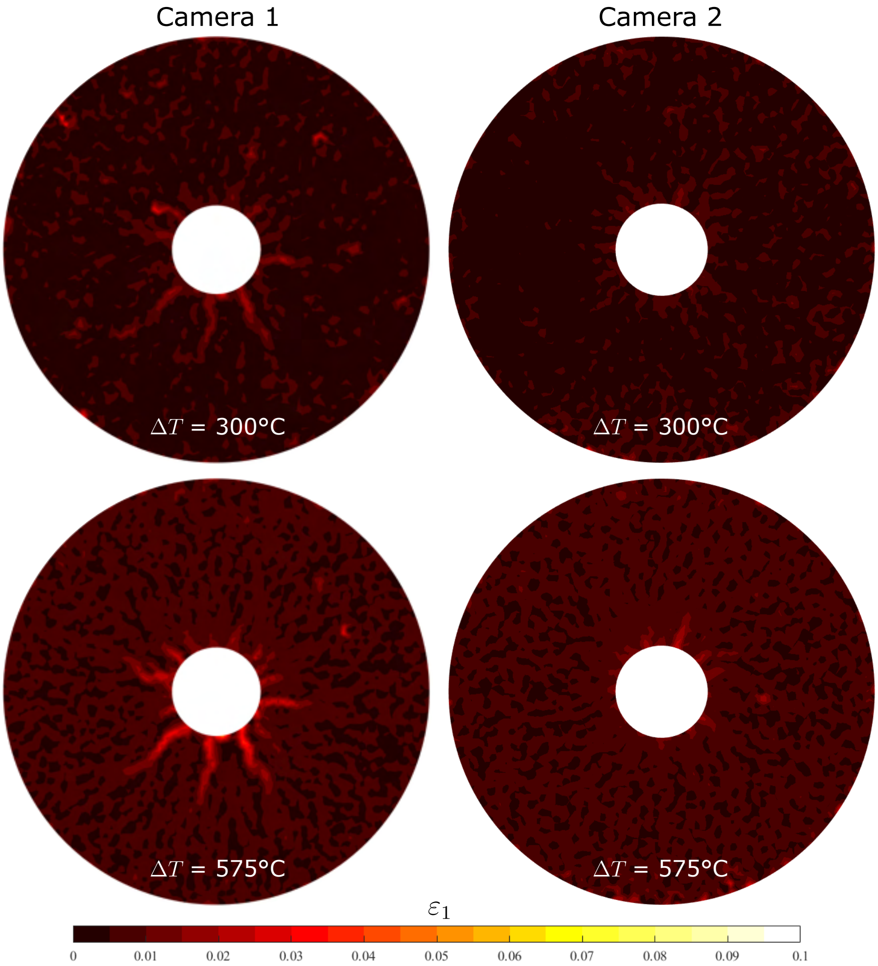

Figure 4.37: Middle size MCS-EAB single inclusion results.

The $\varnothing$ 4.7 mm MCS-EAB single inclusion results up to 600 °C did not show signs of cracks, corroborating the idea that crack initiation is dependent on the inclusion size. This reinforces the idea that an energy approach is needed to accurately predict the cracking in composite systems under temperature variation.

4.6.4 Random multiple inclusion MCS-EAB specimen cracking

The smaller size brass inclusions were also used for an experiment with randomly distributed multiple inclusions. The experiment was performed as previously described for MCS-EAB specimens. The volume fraction effect produced several cracks in the system, in contrast to the single inclusion experiment for this size of brass inclusion, being that cracking began around a temperature variation of 40 °C. Figure 4.38 brings the multiple inclusion MCS-EAB cracking pattern for a temperature variation of 200 °C.

The multiple inclusion system results brought a lot of complex cracking phenomena. In Figure 4.39 the early stages of the System cracking up to a temperature variation of 100 °C is displayed. It is interesting to observe that the most prominent crack observed in Figure 4.38 was not the first one to nucleate, appearing only after a temperature variation of 80 °C. The crack path of this particular crack eventually reached the border of the specimen, being why it eventually became an easier path to open.

4.7 MCS-EAYSZ temperature variation experiments in F900

MCS-EAYSZ was the first attempt to create a ceramic/ceramic model composite system to be tested in F900. The experiments with this system were conducted up to 900 ℃ and followed a similar investigation as the one proposed to MCS-EAB, specimens with one, two and three inclusions. The idea behind the system was to depict a more realist system with a reasonable mismatch that could lead it to fracture when summited to a temperature increase. However, the experimental investigation of the system did not result in cracks, or at least, in cracks visible using the technique, even in a model composite with three inclusions. To illustrate the results attained, Figure 4.40 brings some fields for a very close three inclusion MCS-EAYSZ specimen at 900 °C. By observing the displacement fields, no

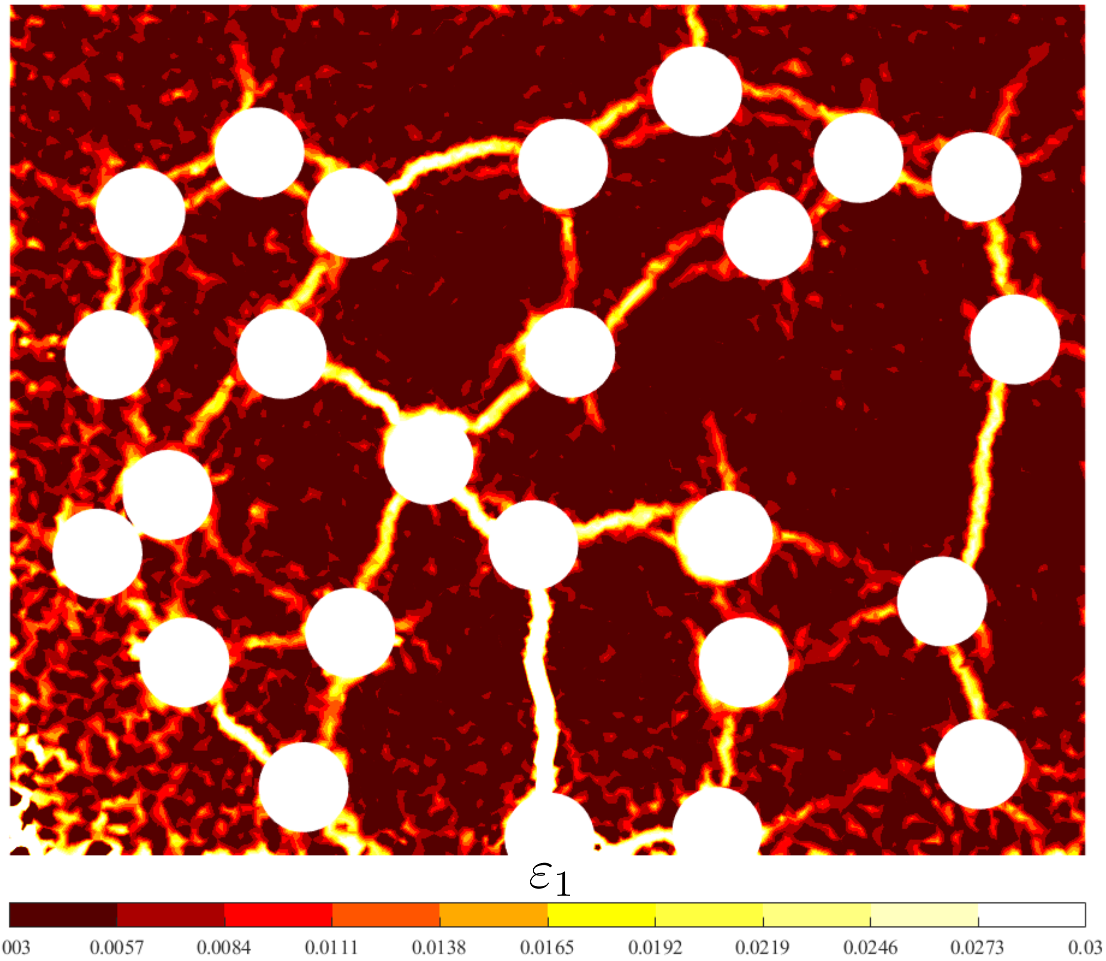

Figure 4.38: Crack pattern for multiple inclusion MCS-EAB observed for $\Delta T = 200°$C via the maximum principal strain field.

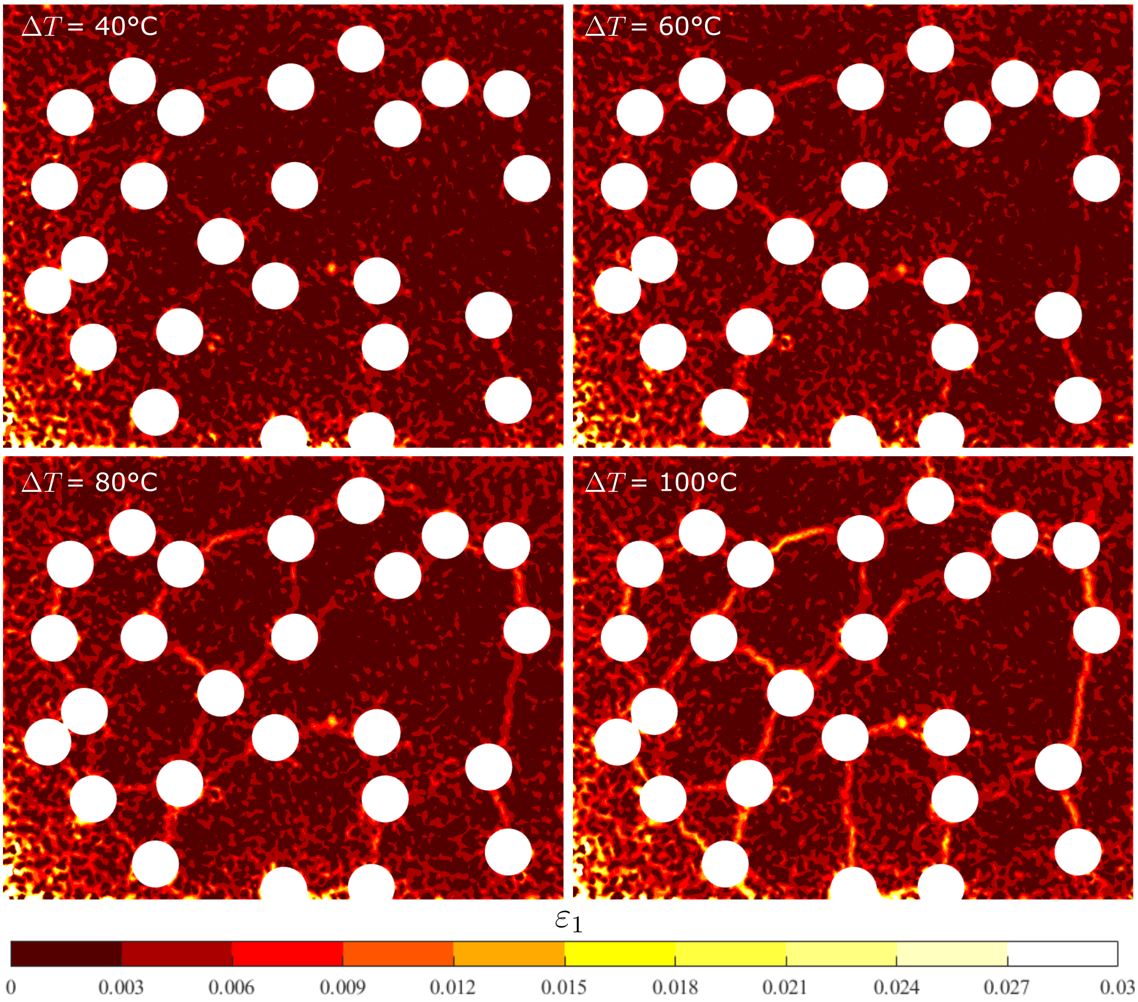

Figure 4.39: Crack evolution for multiple inclusion MCS-EAB observed for $\Delta T = 40, 60, 80,$ and $200°$C via the maximum principal strain field.

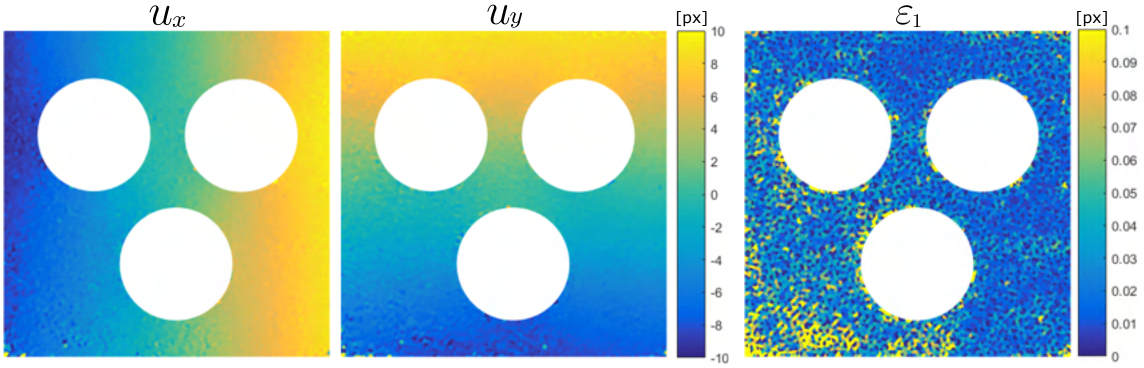

Figure 4.40: Horizontal and vertical displacement and maximum principal strain fields for three inclusions MCS-EAYSZ specimen at 900 °C.

severe discontinuity is observed. The maximum principal strain field, although presenting some noise, also does not show clear signs of any cracks.

One hypothesis to explain the non-fracture of the system is that, although there was a positive CTE mismatch, it decreases with the temperature increase. Therefore, the interfacial stress being a function of $\Delta\alpha\Delta T$, the stress increase would not be what was originally expected. To exemplify this, Figure 4.41 was produced, illustrating the different interfacial stress increase for MCS-EAB and MCS-EAYSZ. The properties used to produce Figure 4.41 were the same used in the numerical models from the previous section (Brass: $E = 80\,GPa, \nu = 0.3$; Alumina $E = 14.5\,GPa, \nu = 0.22$) and for zirconia it was used $E = 164\,GPa, \nu = 0.33$.

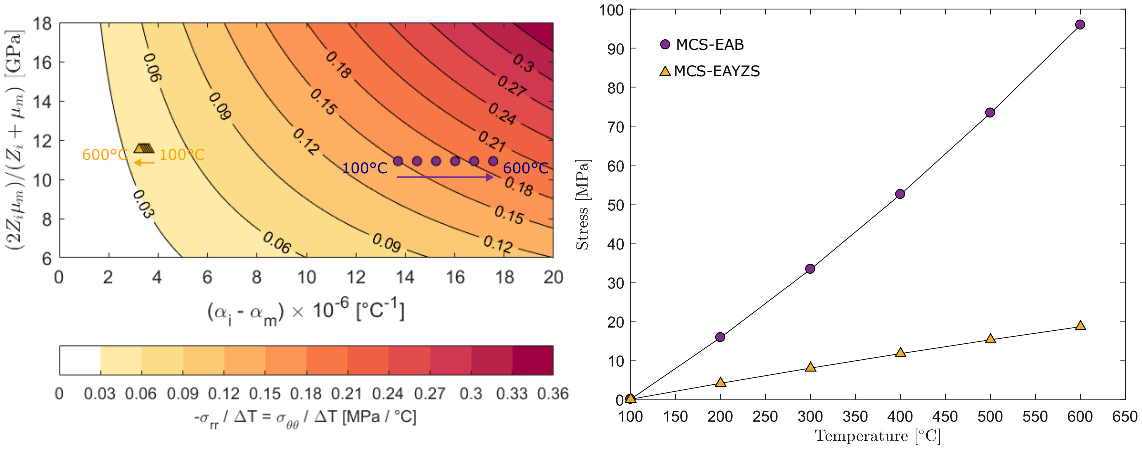

Figure 4.41: Interfacial stress of MCS-EAB and MCS-EAYZS considering the temperature dependent mismatch of the systems. In the left, a diagram is presented showing the interfacial stress per °C of temperature increase, and in the right the arising of the interfacial stress considering a temperature variation from 100 to 600 °C for each system.

As discussed in Chapter 2, the CTE mismatch is the primary driven-force for the stress arising due to temperature variation in composite systems. The zirconia was chosen as an inclusion candidate for the observed higher CTE values in the literature in comparison to alumina, but it was not expected that the CTE mismatch among the materials would decrease with the temperature increase.

4.8 Results conclusion

The experimental investigation of the MCSs embraced different approaches as different material combinations, effects of the volume fraction, and inclusion size. Overall, the methods developed successfully captured the full-field interaction between the phases and evaluated the system's cracking when it occurred. Also, all the thermomechanical characterization of the materials composing the MCS-EAB and MCS-EAYSZ helped understand the different responses of these systems. The two-camera approach described made a huge difference in the correct evaluation of the material's CTE and also in better evaluating the cracking of the MCSs.

5 CONCLUSIONS

This chapter discusses the final remarks of the present thesis alongside the discussions related to the difficulties and perspectives in relation to the work.

5.1 Remarks

The thermomechanical behavior of composite systems is a subject of great interest to several applications and manufacturing processes. This subject can be investigated by many approaches, as demonstrated in this thesis. The development of an experimental methodology using DIC that allows observing the phases' interaction in a model composite during a temperature variation was a great achievement. Further, the development of the furnace that allowed the observation of both sides of a specimen, and the conduction of experiments observing its opposite faces, proved to be important to avoid out-of-plane effects when evaluating material properties such as the CTE and also to observe the different amounts of damage in each face of the model composites.

The performing of experiments with temperature using a two-camera setup DIC brought many challenges that were tackled. Some of these challenges included obtaining glass windows for high temperatures and special camera filters, testing many illumination systems and texturing methodologies, and creating a camera system alignment.

DIC-assisted temperature variation experiments may be more difficult than DIC-assisted experiments in high temperatures. The temperature variation aspect inputs not only a temporal temperature variation that may affect the optical properties of the glass, tested specimen and texture (such as its color), radiation levels, and all the expanding parts of the system but also deals with spatial temperature gradients, and the change in the ambient thermal properties such as convection, that results in heat hazes that may create artifacts in the correlation results. All of these, increases the noise in the results, nevertheless, these difficulties were dealt with in the best way possible to attain quite satisfactory results.

Optical dilatometries conducted in F600 and F900 were really important to the conclusion that the two-camera setup or the employment of other methodologies such as stereo correlation or the use of special components such as telecentric lens is essential to obtaining of trustworthy results. The brass dilatometry comparison shown in Subsection 4.1.3 of Chapter 4 was a good example to elucidate that. But also, in the data displayed in Subsections 4.1.1 and 4.1.4, the need to observe both face's results was displayed.

The methodology presented in Section 4.3 was suitable for analyzing the interaction between the phases in cylindrical inclusion model composites during heating, where Digital Image Correlation (DIC) was used to obtain displacement and strain fields. These measurements allowed to investigate the phases' interaction and to fit the experimental data to an analytical model. The DIC results also allowed the visualization of the crack pattern evolution, which was followed quantitatively by computing the average Mean Crack Opening Displacement (MCOD) for damaged elements and the Surface Crack Density (SCD) as explained in Section 4.3. In this methodology, the proposed analytical model to describe the radial displacement for the model composite, showed good agreement with the experimental results, even for temperatures where cracks had already appeared. To verify this correspondence, the parameter Am, which represents the strain when $(\varepsilon_{rr}(\lim_{r\to\infty}) = Am = \alpha_M \Delta T)$, identified in the fit of the model composite experiment, showed similar values with the thermal strain attained from the alumina slurry's optical dilatometry, showing that the parameters identified by the model are representative of the material properties identified. From the analysis of the interface region, it was possible to estimate the beginning of cracking in the system using a threshold value applied to the inelastic maximum principal strain field. Also, the analysis of the SCD and average MCOD provided the visualization of the cracks' propagation and growth during the temperature increase, allowing the observation of these parameters for several cracks in the experiment individually.

Section 4.6 conducted a similar investigation but using numerical models to remove the thermoelastic components of the maximum principal strain for a system with 1, 2, and 3 inclusions and obtain data of both opposite sides of the model composites. These results were obtained thanks to the development of the F900 and all the apparatus related to it. Using numerical models for the subtractions of thermoelastic effects was also successful, allowing the analysis of the SCD and average MCOD for these experiments to evaluate the cracking initiation and propagation.

The diagram, elaborated to represent Selsing's equation graphically (Figure 2.16), allowed a broader correlation for material selection in low-volume fraction particle composite systems designed for temperature variation applications. The diagram structure can also be used with other analytical models as the one used in this thesis. There is also a perspective to improve the diagram by including the effects of the system's volume fraction. The use of a similar diagram approach for a cylindrical system (Figure 4.41) to compare the MCS-EAB and MCS-EAYSZ also brought a huge insight into the different responses of the systems to temperature variation.

The present work brought new approaches to studying material phase interaction due to CTE mismatch and the evaluation of cracking in such systems. Also, it reveals a whole field of possibilities to explore by conducting in situ experiments using field measurement techniques allied with analytical and numerical approaches. Further, MCS with different configurations of multiple inclusions. In future works, elastic properties of the materials phases for different temperatures could be evaluated. With these data feeding the analysis, it is possible to better estimate the interfacial stress using the analytical or numerical models.

5.2 Suggestion for future works

To accurately estimate the interfacial stress of a composite system in a temperature variation due to CTE mismatch, the property variation of the phases with respect to temperature should be evaluated. In this thesis the CTE was evaluated in such a way, however, the temperature-dependent elastic properties were not explored. Therefore, the investigation of a system with the temperature-dependent relevant properties all characterized should give a better estimation of the interfacial stress of such system. This work would benefit of all the insights brought in this thesis and perhaps could achieve further conclusions related to the influence of the elastic properties. Also, the possibility of fracture properties changing in with temperature could also play a role in the cracking process.

With the results presented for both sides cracking, 3D FE numerical models could further investigate the fracture of the model composite using damage models to match the results achieved experimentally and therefore obtain fracture parameters of the system. The multiple inclusion cracking result is another one that would benefit from a FE analysis. It presents a complex experimental cracking pattern evolution that could be used in the validation of elaborated models.

Real systems that present cracking as some presented in the literature review, or of industrial interest, could be produced and tested following the methodology presented. The investigation with full-field results could bring enlightenment to the material behavior with temperature variation, allowing the observation of the critical temperature variation in function of the inclusion size and the volume fraction. The use of the chats as the ones presented would also help to understand the general behavior of such systems.

In this thesis, the geometry of the model composites was optimized for the use of 2D DIC, however, F900 was designed to allow stereo correlation. Therefore, a work could be done with other geometries of model composites, and the use of stereo correlation to investigate cracking due to CTE mismatch.

A new oven with similar characteristics as F900 was built to achieve temperatures up to 1400 °C. Perhaps, the study of ceramic-ceramic model composites cracking due to CTE mismatch can be achieved with this increase rage of temperature variation or the use of other systems with higher CTE mismatch.

With the two-camera setup, optimized methodology to evaluate CTE of materials, interesting phenomena of materials known for phase transformation or other temperature-dependent phenomena could be investigated with full-field results. Also, the methodology also gives a solution to investigate the expansion of materials that would have their estimates affected by contact measure techniques.

REFERENCES

[1] Ashby, M.F.. Materials Selection in Mechanical Design. 2005. ISBN 0750661682. doi:`10.1016/B978-1-85617-663-7.00011-4`. `arXiv:arXiv:1011.1669v3`.

[2] Ceramic Materials; vol. 2. 2012.

[3] Callister, W.D., Rethwisch, D.G.. Materials Science and Engineering: An Introduction. 2007. ISBN 978-0-470-41997-7.

[4] Sparavigna, A.C.. Ancient concrete works. arXiv e-prints 2011;:arXiv:1110.5230`arXiv:1110.5230`.

[5] Beazley, J.D.. Attic Red-figured Vase-Painters. Photographer Marie-Lan Nguyen. 1963.

[6] Davis, T.M.. Best of Theodore M. Davis. 1915. URL: `https://www.metmuseum.org/art/collection/search/554677`.

[7] Crawford, M.. Ancient Roman Concrete Stands the Test of Time. Photographer Roy Kaltschmidt. The American Society of Mechanical Engineers (ASME) 2017;URL: `https://www.asme.org/topics-resources/content/ancient-roman-concrete-stands-test-time`.

[8] Chawla, K.K.. Composite materials. Department of Materials Science and Engineering. University of Alabama, Birmingham, AL 35294, USA.; 2012. ISBN 9783540885450. doi:`10.1007/978-3-540-88546-7_5`.

[9] William G. Roeseler, Branko Sarh, M.U.K.. COMPOSITE STRUCTURES: THE FIRST 100 YEARS. In: 16TH INTERNATIONAL CONFERENCE ON COMPOSITE MATERIALS; vol. 125. 2017, p. 264–272. doi:`10.1016/j.resconrec.2017.06.023`.

[10] Karbhari, V.M., Zhao, L.. Use of composites for 21st century civil infrastructure. Computer Methods in Applied Mechanics and Engineering 2000;185(2-4):433–454. doi:`10.1016/S0045-7825(99)90270-0`.

[11] Smith, F., March, G.M.. Composites leadership forum. 2015. URL: `www.compositesleadershipforum.com`.

[12] Alemour, B., Badran, O., Hassan, M.R.. A review of using conductive composite materials in solving lightening strike and ice accumulation problems in aviation. Journal of Aerospace Technology and Management 2019;11:1–23. doi:`10.5028/jatm.v11.1022`.

[13] Anderson, T.. Fracture Mechanics: Fundamentals and Applications. 2005. ISBN 9781420058215. doi:`10.1007/978-1-4612-1740-4`.

[14] Campbell, F.C.. Introduction to Composite Materials. 2010.

[15] Callister, W., Rethwisch, D.. Materials Science and Engineering: An Introduction, 9th Edition: Ninth Edition. John Wiley and Sons, Incorporated; 2013. ISBN 9781118476543. URL: `https://books.google.com.br/books?id=TmxbAgAAQBAJ`.

[16] Selsing, J.. Internal Stresses in Ceramics. Journal of the American Ceramic Society 1961;44(8):419–419. doi:`10.1111/j.1151-2916.1961.tb15475.x`.

[17] Davidge, R.W., Green, T.D.. The Strength of Two-Phase Ceramic/Glass Materials. Journal of Materials Science 1968;3:629–634.

[18] Tessier-Doyen, N., Glandus, J.C., Huger, M.. Untypical Young's modulus evolution of model refractories at high temperature. Journal of the European Ceramic Society 2006;26(3):289–295. doi:`10.1016/j.jeurceramsoc.2004.10.028`.

[19] Khlifi, I., Pop, O., Dupré, J.C., Doumalin, P., Huger, M.. Investigation of microstructure-property relantionships of magnesia-hercynite refractory

composites by a refined digital image correlation technique. Journal of the European Ceramic Society 2019;39(13):3893–3902. doi:`10.1016/j.jeurceramsoc.2019.05.010`.

[20] Fu, Y.F., Wong, Y.L., Tang, C.A., Poon, C.S.. Thermal induced stress and associated cracking in cement-based composite at elevated temperatures - Part I: Thermal cracking around single inclusion. Cement and Concrete Composites 2004;26(2):99–111. doi:`10.1016/S0958-9465(03)00086-6`.

[21] Chapline, G., Snapp, C., Pessin, M., Butler, J., Sparks, J.S., Bauer, P., et al. Thermal protection systesms. Engineering Inovations 2014;:182–199.

[22] Kang, D., Pikhitsa, P.V., Choi, Y.W., Lee, C., Shin, S.S., Piao, L., et al. Ultrasensitive mechanical crack-based sensor inspired by the spider sensory system. Nature 2014;516(7530):222–226. URL: `http://dx.doi.org/10.1038/nature14002`. doi:`10.1038/nature14002`.

[23] Shen, L., Ren, Q., Xia, N., Sun, L., Xia, X.. Mesoscopic numerical simulation of effective thermal conductivity of tensile cracked concrete. Construction and Building Materials 2015;95:467–475. doi:`10.1016/j.conbuildmat.2015.07.117`.

[24] Shen, L., Ren, Q., Zhang, L., Han, Y., Cusatis, G.. Experimental and numerical study of effective thermal conductivity of cracked concrete. Construction and Building Materials 2017;153:55–68. doi:`10.1016/j.conbuildmat.2017.07.038`.

[25] Vu, M.N., Nguyen, S.T., Vu, M.H., Tang, A.M., To, V.T.. International Journal of Heat and Mass Transfer Heat conduction and thermal conductivity of 3D cracked media 2015;89:1119–1126. doi:`10.1016/j.ijheatmasstransfer.2015.05.113`.

[26] Khlifi, I., Pop, O., Dupré, J.C., Doumalin, P., Huger, M.. Fracture process analysis in magnesia-hercynite refractory materials by combining an enhanced digital image correlation method with wedge split-

ting test. Theoretical and Applied Fracture Mechanics 2021;116:103134. doi:https://doi.org/10.1016/j.tafmec.2021.103134.

[27] Federal Aviation Administration, . Aviation Maintenance Technician Handbook - Powerplant; vol. 2. 2018.

[28] Yuan, C., Ding, Z., Wang, T.J., Dunn, M.L., Qi, H.J.. Shape forming by thermal expansion mismatch and shape memory locking in polymer/elastomer laminates. Smart Materials and Structures 2017;26(10). doi:10.1088/1361-665X/aa8241.

[29] NASA, . Parker solar probe. National Aeronautics and Space Administration. 2018. URL: https://www.nasa.gov/content/goddard/parker-solar-probe.

[30] NASA', . Orion Spacecraft. National Aeronautics and Space Administration. 2018. URL: https://www.nasa.gov/exploration/systems/orion/index.html.

[31] Quilter, A.. Composites in Aerospace Applications. Information Handling Services, Inc (IHS) 2004;:1–5.

[32] Bobet, J.L., Lamon, J.. Thermal Residual Stresses in Ceramic Matrix Composites- I. Axixymmetrical Model and Finite Element Analysis. Acta Metall Mater 1995;43(6):2241–2253.

[33] Li, L.. A micromechanical crack opening displacement model for fiber-reinforced ceramic-matrix composites considering matrix fragmentation. Theoretical and Applied Fracture Mechanics 2021;112(December 2020):102875. URL: https://doi.org/10.1016/j.tafmec.2020.102875. doi:10.1016/j.tafmec.2020.102875.

[34] Li, L.. Hysteresis-based approach to estimate constituent properties of SiC/SiC ceramic matrix composites. International Journal of Fatigue 2023;167(PA):107302. URL: https://doi.org/10.1016/j.ijfatigue.2022.107302. doi:10.1016/j.ijfatigue.2022.107302.

[35] King, J.E.. Failure in composite materials. Metals and materials 1989;5(12):720–726.

[36] Luchini, B., Sciuti, V.F., Angélico, R.A., Canto, R.B., Pandolfelli, V.C.. Thermal expansion mismatch inter-inclusion cracking in ceramic systems. Ceramics International 2016;42(10):12512–12515. doi:`10.1016/j.ceramint.2016.05.013`.

[37] Luchini, B., Sciuti, V.F., Angélico, R.A., Canto, R.B., Pandolfelli, V.C.. Critical inclusion size prediction in refractory ceramics via finite element simulations. Journal of the European Ceramic Society 2017;37(1):315–321. doi:`10.1016/j.jeurceramsoc.2016.08.008`.

[38] Joliff, Y., Absi, J., Glandus, J.C., Huger, M., Tessier-Doyen, N.. Experimental and numerical study of the thermomechanical behaviour of refractory model materials. Journal of the European Ceramic Society 2007;27(2-3):1513–1520.

[39] Joliff, Y., Absi, J., Glandus, J.C., Huger, M., Tessier-Doyen, N.. Experimental and numerical study of the thermomechanical behaviour of refractory model materials. Journal of the European Ceramic Society 2007;27(2-3):1513–1520. doi:`10.1016/j.jeurceramsoc.2006.04.031`.

[40] Zago, I.P., Angélico, R.A.. Crack pattern identification procedure of cylindrical model composites subjected to temperature variation via DIC. In: 3º - Simpósio de Pós-Graduação em Engenharia Mecânica. 2018, p. 1–6.

[41] Lu, T.C., Yang, J., Suo, Z., Evans, A.G., Hecht, R., Mehrabian, R.. Matrix cracking in intermetallic composites caused by thermal expansion mismatch. Acta Metallurgica Et Materialia 1991;39(8):1883–1890. doi:`10.1016/0956-7151(91)90157-V`.

[42] Vargas, R., Neggers, J., Canto, R., Rodrigues, J., Hild, F.. Analysis of wedge splitting test on refractory castable via integrated dic. Journal

of the European Ceramic Society 2016;36(16):4309 – 4317. doi:https://doi.org/10.1016/j.jeurceramsoc.2016.07.007.

[43] Hild, F., Roux, S., Bernard, D., Hauss, G., Hild, F., Roux, S., et al. ON THE USE OF 3D IMAGES AND 3D DISPLACEMENT MEASUREMENTS FOR THE ANALYSIS OF DAMAGE MECHANISMS IN CONCRETE-LIKE MATERIALS To cite this version : HAL Id : hal-01385670. In: International Conference on Fracture Me- chanics of Concrete and Concrete Structures. 2016,.

[44] Buljac, A., Jailin, C., Mendoza, A., Neggers, J.. Digital Volume Correlation : Review of Progress and Challenges Digital Volume Correlation : Review of Progress and HAL Id : hal-01744752. Experimental Mechanics, Society for Exper- imental Mechanics 2018;C(April). doi:10.1007/s11340-018-0390-7.

[45] Bargmann, S., Klusemann, B., Markmann, J., Eike, J., Schneider, K., Soyarslan, C., et al. Progress in Materials Science Generation of 3D representative volume elements for heterogeneous materials : A review. Progress in Materials Science 2018;96:322–384. URL: https://doi.org/10.1016/j.pmatsci.2018.02.003. doi:10.1016/j.pmatsci.2018.02.003.

[46] Stoneham, A.M., Harding, J.H.. Invited review: Mesoscopic modelling: materials at the appropriate scale. Materials Science and Technology 2009;25(4):460–465. doi:10.1179/174328408X311062.

[47] Dowling, N.E.. Mechanical Behavior of Materials Engineering Methods for Deformation, Fracture, and Fatigue. 2013. ISBN 9780131395060. URL: www.pearsoninternationaleditions.com{%}0A?Pearson. doi:10.1017/CBO9781107415324.004. arXiv:arXiv:1011.1669v3.

[48] Jeong, H.. Effects of voids on the mechanical strength and ultrasonic attenuation of laminated composites. Journal of Composite Materials 1997;31(3):276–292. doi:10.1177/002199839703100303.

[49] Llorca, J., Needleman, A., Suresh, S.. An analysis of the effects of matrix void growth on deformation and ductility in metal-ceramic composites. Acta Metallurgica Et Materialia 1991;39(10):2317–2335. doi:`10.1016/0956-7151(91)90014-R`.

[50] Herakovich, C.T.. Mechanics of composites: A historical review. Mechanics Research Communications 2012;41:1–20. doi:`10.1016/j.mechrescom.2012.01.006`.

[51] Sonego, M., Fleck, C., Pessan, L.A.. Hierarchical levels of organization of the Brazil nut mesocarp. Scientific Reports 2020;10(1):1–13. URL: `http://dx.doi.org/10.1038/s41598-020-62245-y`. doi:`10.1038/s41598-020-62245-y`.

[52] Joliff, Y., Absi, J., Huger, M., Glandus, J.C.. Experimental and numerical study of the elastic modulus vs temperature of debonded model materials. Computational Materials Science 2008;44(2):826–831. URL: `http://dx.doi.org/10.1016/j.commatsci.2008.04.024`. doi:`10.1016/j.commatsci.2008.04.024`.

[53] Zanardi, H., Zago, I.P., Angélico, R.A.. Prediction of the Crack Pattern in Ceramic Composites Subjected To Temperature Variation. In: 2º - Simpósio de Pós-Graduação em Engenharia Mecânica. 2002; 2017, p. 3–7.

[54] Zago, I.P., Zanardi, H., Gonçalves, M.C., Angélico, R.A.. ESTUDO DO TRINCAMENTO DE COMPÓSITOS MODELO SUBMETIDOS À VARIACÃO DE TEMPERATURA. In: 4º - Simpósio de Pós-Graduação em Engenharia Mecânica. São Carlos; 2019,URL: `http://biblioteca.eesc.usp.br/images/soac/sipgem/sipgem2019anais.pdf`.

[55] André, D., Levraut, B., Tessier-Doyen, N., Huger, M.. A discrete element thermo-mechanical modelling of diffuse damage induced by thermal expansion mismatch of two-phase materials. Computer Methods in Applied Mechanics and Engineering 2017;318:898–916. URL: `http://dx.doi.org/10.1016/j.cma.2017.01.029`. doi:`10.1016/j.cma.2017.01.029`.

[56] Bobet, J.L., Naslain, R., Guette, A., Ji, N., Lebrun, J.L.. Thermal residual stresses in ceramic matrix composites-II. Experimental results for model materials. Acta Metallurgica Et Materialia 1995;43(6):2255–2268. doi:`10.1016/0956-7151(94)00430-7`.

[57] Hibbeler, R.. Mechanics of Materials. Pearson Education; 2016. ISBN 9780134321233. URL: `https://books.google.com.br/books?id=PL15CwAAQBAJ`.

[58] Ragab, A., Bayoumi, S.. Engineering Solid Mechanics: Fundamentals and Applications. Taylor & Francis; 1998. ISBN 9780849316074. URL: `https://books.google.com.br/books?id=QAASF3oMvEEC`.

[59] Shackelford, J.F.. Ciência Dos Materiais. 2008. ISBN 9788576051602.

[60] Crandall, S.. An Introduction to Mechanics of Solids. Mcgraw Hill Higher Education; 2012. ISBN 9781259084393. URL: `https://books.google.com.br/books?id=VczzjAzm7vAC`.

[61] Montanini, R., Freni, F.. Non-contact measurement of linear thermal expansion coefficients of solid materials by 2014;doi:`10.1088/0957-0233/25/1/015013`.

[62] INGLIS, C.E.. Stresses in a plate due to the presence of cracks and sharp corners. Trans Inst Naval Archit 1913;55:219–241. URL: `https://ci.nii.ac.jp/naid/10010696606/en/`.

[63] Griffits, A.A.. The phenomena of rupture and flow in solids. Masinovedenie 1995;C(1):9–14. doi:`10.1098/rsta.1921.0006`.

[64] Zago, I.P.. Estudo do comportamento mecânico de compósitos modelo submetidos à variação de temperatura via correlação de imagens digitais. Master's thesis; 2019.

[65] Zago, I.P., Vargas, R., Sciuti, V.F., Canto, R.B., Angélico, R.A.. DIC to evaluate a model composite system cracking due to CTE mismatch. Theoretical and Applied Fracture Mechanics 2024;131(October

2023):104330. URL: `https://doi.org/10.1016/j.tafmec.2024.104330`. doi:`10.1016/j.tafmec.2024.104330`.

[66] Zago, I.P., Angélico, R.A.. Procedimento de identificação do arranjo de trincas via CID para um compósito modelo bifásico submetido a uma variação de temperatura. In: 3° Simpósio de Pós Graduação em Engenharia Mecânica (SIPGEM). São Carlos; 2018, p. 1–6.

[67] de Melo, C.C., Furlan, M., Hild, F., Schmitt, N., Canto, R.B.. Uniaxial compression test on ceramic green compact with bending consideration using digital image correlation. Powder Technology 2020;376:136–148. doi:`10.1016/j.powtec.2020.08.002`.

[68] Gonzales, R.C., Woods, R.E.. Processamento de imagens digitais. 1992. ISBN 8521217269, 9788521217268.

[69] Dougherty, G.. Digital Image Processing for Medical Applications. California State University, Channel Islands: CAMBRIDGE UNIVERSITY PRESS; 2009. ISBN 9780521860857.

[70] Thyagarajan, K.. Digital Image Processing with Application to Digital Cinema. Focal; 2006. ISBN 9780240807294. URL: `https://books.google.com.br/books?id=SQyAv5iAC6sC`.

[71] 12019, U.. tree frog. 2012. URL: `https://pixabay.com/photos/tree-frog-frog-red-eyed-amphibian-69813/`.

[72] Ramesh, K., Sasikumar, S.. Digital photoelasticity: Recent developments and diverse applications. Optics and Lasers in Engineering 2020;135:106186. URL: `https://www.sciencedirect.com/science/article/pii/S0143816619315271`. doi:`https://doi.org/10.1016/j.optlaseng.2020.106186`.

[73] Ramesh, K., Hariprasad, M.P., Bhuvanewari, S.. Digital photoelastic analysis applied to implant dentistry. Optics and Lasers in Engineering 2016;87:204–213. doi:`10.1016/J.OPTLASENG.2016.03.022`.

[74] Vivekanandan A., R.K.. Study of crack interaction effects under thermal loading by digital photoelasticity and finite elements. Exp Mech 2020;60. doi:doi.org/10.1007/s11340-019-00561-9.

[75] Francis, D., Tatam, R.P., Groves, R.M.. Shearography technology and applications : a review 2010;(August). doi:10.1088/0957-0233/21/10/102001.

[76] McCormick, N., Lord, J.. Digital image correlation. Materials Today 2010;13(12):52–54. URL: http://dx.doi.org/10.1016/S1369-7021(10)70235-2. doi:10.1016/S1369-7021(10)70235-2.

[77] Hild, F and Roux, S.. CORRELI Q4: A Software for "Finite-element" Displacement Field Measurements by Digital Image Correlation. Tech. Rep. 254; 2008.

[78] Dufour, J.E., Hild, F., Roux, S.. Integrated digital image correlation for the evaluation and correction of optical distortions. Optics and Laser in Engineering 2014;56:121–133.

[79] Vargas, R., Neggers, J., Canto, R.B., Rodrigues, J.A., Hild, F.. Analysis of a castable refractory using the wedge splitting test and cohesive zone model. Journal of the European Ceramic Society 2019;39(13):3903–3914. doi:10.1016/j.jeurceramsoc.2019.03.009.

[80] Vargas, R., Canto, R.B., Hild, F.. Fracture energy evaluation of refractories in wedge splitting tests from notch opening displacements. Journal of the European Ceramic Society 2021;41(10):5367–5379. doi:10.1016/j.jeurceramsoc.2021.02.055.

[81] Hild, F., Roux, S.. Measuring stress intensity factors with a camera: Integrated digital image correlation (i-dic). Comptes Rendus Mécanique 2006;334(1):8 – 12. URL: http://www.sciencedirect.com/science/article/pii/S163107210500210X. doi:https://doi.org/10.1016/j.crme.2005.11.002.

[82] Sutton, M.A., Yan, J.H., Tiwari, V., Schreier, H.W., Orteu, J.J.. The effect of out-of-plane motion on 2D and 3D digital image correlation measurements. Optics and Lasers in Engineering 2008;46:746–757. doi:`10.1016/j.optlaseng.2008.05.005`.

[83] Leclerc, H., Neggers, J., Mathieu, F., Roux, S., Hild, F.. Correli 3.0. 2015. IDDN.FR.001.520008.000.S.P.2015.000.31500.

[84] Young's modulus and Poisson's ratio of concrete at high temperatures: Experimental investigations. Materials and Design 2013;45:421–429. doi:`10.1016/j.matdes.2012.07.070`.

[85] Charbal, A., Cinoglu, I.S.S., Hild, F., Roux, S., Vermaak, N.. Stereocorrelation Formalism Considering Brightness and Contrast Effects: Application to Torsional Loadings. Experimental Mechanics 2020;.

[86] Dufour, J.E., Beaubier, B., Hild, F., Roux, S.. Cad-based displacement measurements with stereo-dic. Experimental Mechanics 2015;55(9):1657–1668.

[87] Sutton, M.A., Orteu, J.J., Schreier, H.. Image correlation for shape, motion and deformation measurements: Basic concepts, theory and applications. Springer Science & Business Media; 2009.

[88] Maginador, R.V.. Fracture of refractories at room and elevated temperatures analyzed with wedge splitting tests and image correlation. Ph.D. thesis; Universidade Federal de São Carlos / Université Paris-Saclay; 2024.

[89] Belgacem, S., Galai, H.. Cement Refractory Bricks Characteristics: The Importance of Mineralogical Quantification in the Evaluation of the Refractory Bricks Corrosion. October 2021; 2018. ISBN 978-1-53613-863-4.

[90] de Melo, C.C.. COMPUTATIONAL MODELING OF RUBBER MULTIAXIAL PRESSING APPLIED TO CERAMIC MATERIALS. Ph.D. thesis; 2021.

[91] Hild, F., Roux, S., Gras, R., Guerrero, N., Marante, M.E., Flórez-López, J.. Displacement measurement technique for beam kinematics. Optics and Lasers in Engineering 2009;47(3):495–503. doi:`https://doi.org/10.1016/j.optlaseng.2008.03.006`.

[92] Hild, F., Roux, S.. Digital image correlation: from displacement measurement to identification of elastic properties - a review. Strain 2006;42:69–80.

[93] VARGAS, R., ZAGO, I.P., SCIUTI, V.F., FURLAN, M., ANGÉLICO, R.A., HILD, F., et al. Multi-Window Setup for Thermomechanical Experiments Assisted by DIC up to 900 °C. Materials Research 2024;27. URL: `https://doi.org/10.1590/1980-5373-MR-2024-0072`. doi:`10.1590/1980-5373-MR-2024-0072`.

[94] Hayashi, H., Saitou, T., Maruyama, N., Inaba, H., Kawamura, K., Mori, M.. Thermal expansion coefficient of yttria stabilized zirconia for various yttria contents. Solid State Ionics 2005;176(5-6):613–619. doi:`10.1016/j.ssi.2004.08.021`.

[95] Sciuti, V.F., Vargas, R., Canto, R.B., Hild, F.. Pyramidal adaptive meshing for Digital Image Correlation dealing with cracks. Engineering Fracture Mechanics 2021;256:107931. doi:`10.1016/j.engfracmech.2021.107931`.

[96] Sciuti, V.F., Hild, F., Pandolfelli, V.C., Santos, T., Smaniotto, B., Canto, R.B.. Digital Image Correlation applied to in situ evaluation of surface cracks upon curing of MgO-containing refractory castables. Journal of the European Ceramic Society 2021;41(1):1003–1014. doi:`10.1016/j.jeurceramsoc.2020.04.055`.

[97] Sciuti, V.F., Vargas, R., Guerrero, N., Marante, M.E., Hild, F.. Digital image correlation analyses of masonry infilled frame: Uncertainty-based mesh refinement and damage quantification. Mathematics and Mechanics of Solids 2023;0(0). doi:`10.1177/10812865231174840`.

[98] Sciuti, V.F., Vargas, R., Canto, R.B., Hild, F.. Modal characterization of crack network development in an mgo containing refractory castable. The Journal of Strain Analysis for Engineering Design 2023;58(6):490–500. doi:`10.1177/03093247221141490`.

[99] Sciuti, V.F., Hild, F., Pandolfelli, V.C., Santos, T., Smaniotto, B., Canto, R.B.. Digital Image Correlation applied to in situ evaluation of surface cracks upon curing of MgO-containing refractory castables. Journal of the European Ceramic Society 2020;.

[100] Reu, P.L., Jones, E.M.C., O'Hern, T.J., Sweatt, W.C.. Distortion of full-field surface displacements from heat waves. Tech. Rep.; Office of Scientific and Technical Information (OSTI); 2016.

[101] Jones, E., Reu, P.. Distortion of digital image correlation (dic) displacements and strains from heat waves. Experimental Mechanics 2018;58(7):1133 – 1156.

[102] Muskhelishvili, N.. Some Basic Problems of the Mathematical Theory of Elasticity. Springer Netherlands; 2013. ISBN 9789401730341. URL: `https://books.google.com.br/books?id=jdL3CAAAQBAJ`.

APPENDIX A: Elastic parameters of materials

The relations between the elastic constants of an isotropic material are shown in Table A.1. The first column denotes an elastic constants pair, and in each line, how to write the respective property of a column regarding the pair of elastic constants of the line.

Table A.1: Some relations between elastic parameter can be written for isotropic linear-elastic materials.

	E	K	μ	λ	ν
μ, E		$\frac{\mu E}{3(3\mu - E)}$		$\frac{\mu(E - 2\mu)}{3\mu - E}$	$\frac{E - 2\mu}{2\mu}$
μ, ν	$2\mu(1+\nu)$	$\frac{2\mu(1+\nu)}{3(1-2\nu)}$		$\frac{2\mu\nu}{1-2\nu}$	
μ, K	$\frac{9K\mu}{3K+\mu}$			$K - \frac{2\mu}{3}$	$\frac{3K - 2\mu}{2(3K+\mu)}$
E, ν		$\frac{E}{3(1-2\nu)}$	$\frac{E}{2(1+\nu)}$	$\frac{E\nu}{(1+\nu)(1-2\nu)}$	
E, K			$\frac{3EK}{9K - E}$	$\frac{3K(3K - E)}{9K - E}$	$\frac{3K - E}{6K}$
ν, K	$3K(1-2\nu)$		$\frac{3K(1-2\nu)}{2(1+\nu)}$	$\frac{3K\nu}{1+\nu}$	
λ, μ	$\frac{\mu(3\lambda + 2\mu)}{\lambda + \mu}$	$\lambda + \frac{2\mu}{3}$			$\frac{\lambda}{2(\lambda+\mu)}$
λ, K	$\frac{9K(K-\lambda)}{3K-\lambda}$		$\frac{3(K-\lambda)}{2}$		$\frac{\lambda}{3K-\lambda}$

APPENDIX B: Cautions when performing experiments assisted by DIC

It is convenient to draw attention to the conduction of experiments assisted by the DIC. The DIC technique augments the data that almost all conventional experimental procedures can obtain to evaluate material properties, and it is also not an invasive measurement technique. However, if some primary concerns of the technique are not given attention, the correlation procedure could not converge, or the data acquired may be misleading the reality. Therefore, some guidelines must be followed:

- If the sample tested does not have a natural pattern texture suitable to distinguish the intensity values of the elements in the mesh, the sample must be texturized, usually with spray ink or numerically treated. The first evaluation of the texture consists in observing its histogram. Being that an evenly distributed histogram or a Gaussian one is desired.

- During the tests, the image-acquiring devices and the sample tested must not move away from one relative to the other, especially in a way that can change the image focus. This type of experimental error can provide false displacements. It is possible to correct it, but it may not be an easy task.

- The light intensity reflected and emitted by the sample to the acquire device must not change. It means that the illumination of the sample must not be modified or moved during the test, and if the test results in a variation of the emitted radiation, it must be corrected numerically or with the aid of image filters.

- Besides the concerns presented, each experimental procedure may have its concerns as moisture, temperature variation, large displacements, the appearance of discontinuities in the sample, tests in situ, vibration, etc. All these factors must be considered in the DIC technique's evaluation of displacement.

APPENDIX C: The color change problem of temperature variation experiments using DIC: Optical properties, illumination, texture and multiphase systems

The Digital Image Correlation (DIC) is based on the continuity of the optical flux, *i.e.,* , during the experiment, the specimen under a given condition, optimally, should preserve its optical properties, and the light intensity and wave length over the specimen should remain constant. Although these requirements are treated with a lot of care, there is always some divergence of the ideal images acquired, which is why the DIC takes the residual as a variable and a convergence criterion.

In many cases, artificial texture is applied to the tested specimen to make it feasible or to help the DIC algorithm converge. This texture should also maintain its consistency and optical properties during the test's image acquisition. The texture operates as a speckle signature that creates a contrast between the different regions of the specimen.

Therefore, for the conduction of temperature variation experiments in multiphase systems analyzed via DIC there are **the light problem**, **the phases optical properties problem**, **the texture problem**, and **the heat hazes problem**.

C.1 The light problem

The first problem of temperature variation experiments is the change of the light properties reaching the specimen and being captured by the camera. The temperature increase leads to black body radiation, change in the glasses and air refraction, and change in the overall intensity and wavelength of the light captured by the camera. To tackle some of these problems, special lenses, high-intensity blue illumination, and selection of the image's blue layer were used, which improved the results but did not solve all the difficulties faced for correlation.

The DIC software presents a tool of bright and contrast (BC) correction that was indispensable to aid the DIC to be executed. This feature could be used in different ways, some more costly than others, but overall, it slows the DIC process, although being very helpful.

C.2 The phases optical properties problem

The optical properties variation will be space-dependent when dealing with a multiphase system. This means that the BC corrections must differ for each material region, or that one of the phase regions must be excluded from the correlation to apply the BC corrections. The BC correction was applied elementwise for the results where both phases were present, which is the most costly way to use it. Although this was successful in some cases, it was not always effective because of the texture problem, as shown in Figure C.1.

C.3 The texture problem

The texture problem has some layer of discussion that should be presented. A lot of trial and error was performed to improve the understanding of how to better approach the texturization of specimens for high temperatures, and temperature variation experiments. Firstly and foremost, the texture must remain, *i.e.,* , the texture can not degrade, evaporate or diffuse into the specimen. Where all of the above happened at some point of this research while searching for texture solutions. Secondly, the texture will also change its optical properties, which will greatly impact the BC correction effectiveness. Because the BC correction could be applied elementwise, but if material and texture change their color differently, The correction will not be optimal, and if there is more than one texture the problem could be worse. Therefore, as a recommendation, different texture inks or other methods should not be combined, because each one of them will change differently with temperature.

As explained, the above insights were mistakes committed during this research that made the results processing difficult and impracticable or with lower quality in some cases. However, the trial and error performed allowed the current understanding. To understand the effect of this, once again, the image residue is a clear way to observe it, as displayed in Figure C.1.

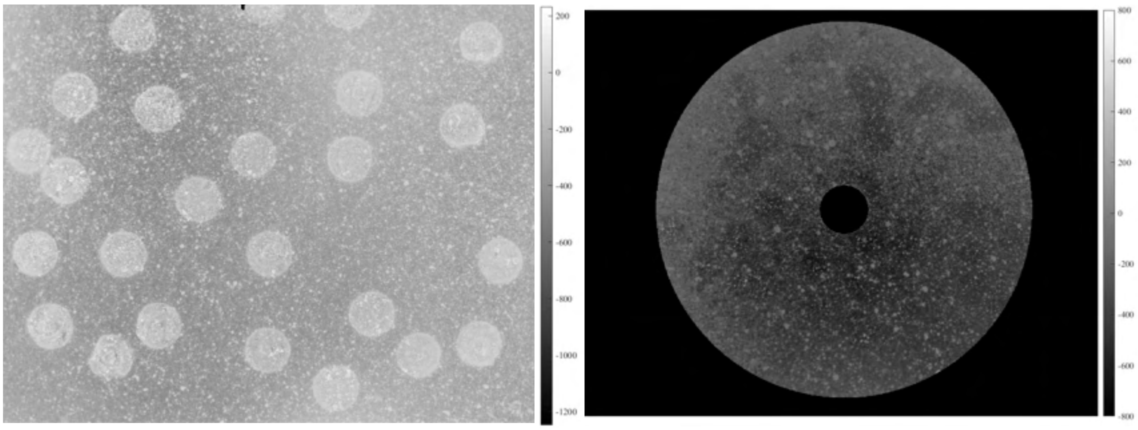

Figure C.1: Residue of two correlations to illustrate the BC correction difficulties for temperature variation experiments in relation to the texture and to multiple phases. The dynamic range of the images was around 4000.

C.4 The heat haze problem

The heat haze occurs due to airs convection and temperature fluctuations inside furnaces. This problem is quite hard to solve, but can be attenuated. High exposure times in image acquisition is the most practical solution. In order to do so, Neutral Density (ND) filters can be used. It is important to mention, however, that every artifact used between the camera sensor and the surface photographed input some distortion, and such filters – for the present research – were identified as the most detrimental for the image quality. Furthermore, even with an exposure time of 10 seconds in some experiments, this was not a perfect solution. Figure C.2 presents the effect of a heat haze comparing the maximum principal strain result of two images spaced by 1 °C. The images before and after the problematic result show no sign of the disturbance observed on the right strain field. These affected field results had to be removed for post-processing, such as crack evaluation.

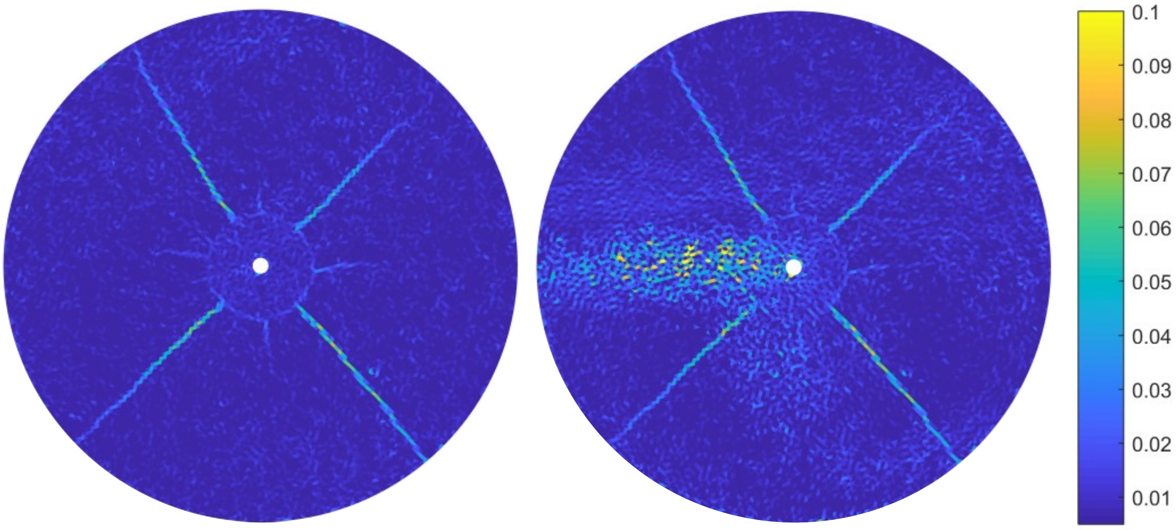

Figure C.2: Heat haze effect on the maximum principal strain field. In the left a result not affected, and in the right one affected by a heat haze. The two results are 1 °C appart.